Università
degli Studi
di Ferrara

DOCTORAL COURSE IN
PHYSICS

CYCLE XXXI

DIRECTOR Prof. Vincenzo Guidi

The next generation experiments for CMB anisotropies: from balloons to space

Scientific/Disciplinary (SDS) FIS/02

Candidate
Dott. Polastri Linda

Supervisor
Prof. Natoli Paolo

Co-advisor
Dott. Molinari Diego

Years 2015-2018

Università
degli Studi
di Ferrara

DOCTORAL COURSE IN
PHYSICS

CYCLE XXXI

DIRECTOR Prof. Vincenzo Guidi

The next generation experiments for CMB anisotropies: from balloons to space

Scientific/Disciplinary (SDS) FIS/02

Candidate
Dott. Polastri Linda

Supervisor
Prof. Natoli Paolo

Co-advisor
Dott. Molinari Diego

Years 2015-2018

E' cosi bello fissare il cielo e accorgersi
di come non sia altro che un vero
e proprio immenso laboratorio di fisica
che si srotola sopra le nostre teste.
Margherita Hack

To my grandparents

Contents

Abstract

The signature of primordial gravitational waves is imprinted in the B-modes of CMB polarization, producing specific polarization patterns that can be disentangled from other sources. Several issues make this detection an extremely challenging measurement. In this thesis I will present two examples of the next generation of CMB polarization experiments: CORE (Cosmic Origins Explorer) and LSPE (Large Scale Polarization Explorer). The first one is a proposed space mission that aims to map the nearly full-sky CMB polarization pattern with unprecedented sensitivity. The second is an experiment composed of two instruments: one flying on a stratospheric balloon and the other ground-based. Both LSPE and CORE have a main science target in the CMB B-modes. They also address a significant list of ancillary science targets. I contributed to developing, testing and validating the future software pipeline for scanning strategy simulations, foreground removal and spectral analyses. I simulated scanning strategy and data reduction for both experiments, in order to select the optimal mission parameters. I also contributed to developing a component separation pipeline to remove the foreground contamination from simulated maps of LSPE.

Sommario

La firma delle onde gravitazionali primordiali è impressa nei modi B della polarizzazione della radiazione cosmica di fondo, producendo schemi di polarizzazione specifici che potrebbero essere distinti e separati da altre fonti. Tuttavia, a causa di molteplici problematiche, la rivelazione di questi patterns risulta una misurazione estremamente impegnativa e stimolante. In questa tesi presento due esempi della prossima generazione di esperimenti che si propongono di misurare con precisione la polarizzazione della CMB: CORE (Cosmic Origins Explorer) e LSPE (Large Scale Polarization Explorer). La prima è una proposta di missione spaziale che mira a mappare il pattern di polarizzazione della CMB quasi a cielo pieno con una sensibilità senza precedenti. Il secondo è un esperimento composto da due strumenti: uno situato su un pallone stratosferico e l'altro a terra. Sia LSPE che CORE hanno come obiettivo scientifico principale lo studio dei modi B della polarizzazione della CMB, affrontando anche un numero significativo di obiettivi scientifici ausiliari. Ho contribuito a sviluppare, testare e convalidare la futura pipeline software per simulare le differenti strategie di scansione, la rimozione delle emissioni astrofisiche e le analisi spettrali. In particolare ho simulato la modalità di scansione del cielo e la data reduction per entrambi gli esperimenti, al fine di selezionare i parametri ottimali di queste missioni. Infine ho contribuito allo sviluppo di una pipeline di component separation, necessaria per rimuovere le contaminazioni dovute alle emissioni astofisiche dalle mappe simulate di LSPE.

Introduction

In the last thirty years physical cosmology underwent an exponential development thanks to the improvement of observational techniques and the use of space-borne telescopes. The observation of the Cosmic Microwave Background (CMB) radiation has set a milestone for the Big Bang theory proposed by G.Gamow in the 1940 [57]. The most ancient radiation ever emitted in the universe was detected for the first time in 1964 by Arno Penzias and Robert Wilson, who observed an isotropic and homogeneous signal in microwave band with a black-body temperature about 3K [80].

In the following decades, technological development has allowed us to perform increasingly better measurements: COBE (1989-1993) [48, 49, 93] proved that the CMB has a perfect (within errors) black-body frequency spectrum and, for the first time, observed CMB anisotropies; WMAP (2001-2010) [17, 39] and Planck (2009-2013) [10] measured the angular spectrum of the CMB anisotropies with increasing resolution and sensitivity. WMAP and Planck also measured the expected, but much weaker polarized signal of the CMB. Together with other astrophysical and cosmological observations they greatly contributed to shape up our current understanding of cosmology. All the knowledge acquired can be summarized inside a quite simple six parameter model called Lambda Cold Dark Matter (ΛCDM) model. This model is remarkably successful because it depends on a small set of parameters (those describing the geometry of the Universe, its composition and the formation of its structures) that can be measured from the data finding excellent consistency with observations.

Furthermore, the data from the Planck experiment are good enough to allow cosmological constraints below the percent level, which is a remarkable confirmation of the ΛCDM model. The latest data released by the Planck collaboration represents the ultimate measurement of CMB temperature anisotropies but went short of exploiting the information encoded in the CMB polarization. The Planck satellite also gave strong evidence for an early inflationary phase of the universe, yet the predicted background of primordial gravitational waves remains unobserved. The signature of primordial gravitational waves is imprinted in the B-modes of CMB polarization, producing specific polarization patterns which can be disentangled from other sources. However, several issues make this detection extremely challenging. Gravitational lensing of the CMB photons due to structures between last scattering surface and us also generates B-modes as well as foregrounds emission and contaminations of other systematics origin. Nevertheless, the CMB appears as the most promising observable capable of placing limits on the inflationary era. For these reasons, it is mandatory for future CMB experiments to keep foregrounds contamination and systematics under control in order to deliver the "ultimate" observations in polarization as Planck has done for temperature.

The purpose of this thesis is to study in detail two examples of next-generation CMB polarization experiments. I will first focus on CORE, a space mission proposed to ESA for M5 call, planning to map the CMB polarization pattern at nearly full sky with cosmic variance errors [23]. I will then discuss LSPE, composed of two instruments: one flying on a stratospheric balloon and the other ground-based, aimed at measuring B-mode CMB polarization at large angular scales over 30% of the sky [18].

In particular I contributed to developing, testing and validating the future software pipeline for these experiments, including scanning strategy, data reduction, foreground removal and spectral analyses. In particular, I have simulated data acquisition for both experiments in order to optimize their scanning parameters and developed a component separation pipeline to remove the foreground contaminations from the simulated maps.
This thesis is organized as follows:

1. Chapter 1: I provide an overview of the ΛCDM model, starting from the cosmological principle. I describe the evolution of the universe, the main epochs of the universe and provide a brief introduction to inflation. Moreover, in the end of the chapter, I describe the main aspects of perturbation theory, including the Boltzmann equations for the evolution of cosmological perturbations.

2. Chapter 2: I describe the origin of the cosmic microwave background radiation, showing how gravitational potential is connected to matter perturbations and how their influence changes the properties of the photon-

baryon fluid. I describe the anisotropies of the CMB both in temperature and polarization and I derive the expression for the CMB temperature anisotropies power spectrum (APS). Moreover, I focus on the polarization aspects of the CMB i.e. how polarization is generated and how it is observed. I also discuss briefly the main foreground contaminations.

3. Chapter 3: I present the first part of my original work of this thesis. This chapter begins with the description of the proposed Cosmic Origin Explorer (CORE) experiment. I describe the goals of the mission, the instrument and its scanning strategy. I give a brief introduction about the main expected systematic effects, including correlated noise that can be alleviated in the map-making process. Based on the latter I optimize the scanning strategy of the experiment, while keeping correlated noise under control.

4. Chapter 4: I describe the Large Scale Polarization Explorer (LSPE) experiment. Starting with the description of the instrument and present the code employed to simulate its scanning strategy. I subsequently analyse the properties of the noise maps and attempt to optimize the scanning parameters and the map-making process. Moreover I present a component separation algorithm and test it on the LSPE optimized configuration. Finally I show the conclusions and perspectives for future work.

1

An expanding Universe

> *Se l'universo si espande,*
> *perché non riesco mai*
> *a trovare un parcheggio?*
> Woody Allen

Based on strong observational data and on our knowledge of fundamental and particle physics, the standard cosmological model (ΛCDM) describes an expanding universe which starts from an extremely hot and dense initial condition. The universe continues to expand and cool adiabatically allowing the existence of a series of processes that shape the universe that we observe today. The abundance of light elements, the distribution of large-scale structures and the presence of a fossil radiation that permeates the universe are the most important observables of its thermal history. The latter called Cosmic Microwave Background (CMB) radiation, is a sea of photons that pass through the universe and scattered, the last time, when the universe was about 1000 times hotter than today.
The CMB is a relic radiation of the Big Bang and it is the main source of data for all the cosmological studies because contains information of the early stage of the universe that may be investigated through the analysis of the statistical properties (of its temperature and polarization anisotropies). This relic radiation has a mean temperature around $T_0 = 2.725$ K, but if we remove this component we observe anisotropies at the level of 10^{-5} in temperature and 10^{-6} in polarization. In this chapter we will see in details how it is possible to investigate the main steps of the thermal history of the early universe and how the model that comes out is almost perfectly in agreement with the observational data.

1.1 The cosmological principle

On large scales (> 100Mpc [1]), the universe is described with good approximation as homogeneous and isotropic, i.e. we can find the same physical properties in every part of the universe, no preferred directions for any observer are defined [30, 51, 63, 72, 100].

Thus, the general appearance of the universe must not depend on the observer position and on the direction of observation. The assumptions of homogeneity and isotropy of the universe represent the *cosmological principle.*

Isotropy does not imply homogeneity, i.e. assuming isotropy from a single point of observation does not ensure homogeneity and measuring physical quantities in different areas of the universe does not guarantee isotropy. Probing isotropy, by at least, two different observables would be a confirmation of the cosmological principle, however, we are limited in space and time.

Assuming the cosmological principle leads to a series of implications: homogeneous and isotropic means that the space-time can be exfoliated in a series of 3D hypersurfaces all characterized by a time coordinate. Consider the metric:

$$ds^2 = g_{\mu\nu} dx^\mu dx^\nu \tag{1.1}$$

where $g_{\mu\nu}$ is the metric tensor.

Considering the space-space and time-time coordinates we obtain for the metric tensor:

$$g_{00} = -1 \tag{1.2}$$

$$g_{ij} = a^2 \gamma_{ij}(r). \tag{1.3}$$

In the Eq.(1.3), we describe an expanding universe, with an expanding scale factor equal to $a \equiv a(t)$ (today $a(t_0) = 1$) and a spatial part of the metric (γ_{ij}) that is a function only of the radial coordinate r in the assumption of isotropy.

Putting together the Eqs.(1.2) and (1.3), the results is a metric for a 4D space-time:

$$ds^2 = -dt^2 + a^2 \gamma_{ij} dx^i dx^j. \tag{1.4}$$

If we consider a space where every path between two points can be continuously transformed into any other path, we can write a simpler version of Eq.(1.4) in polar coordinates. The solution to the Einstein equation in an homogeneous and isotropic universe is the so called **Friedmann–Robertson–Walker (FRW)**

---

[1] 1 Mpc = 3.086 $\times 10^{22} m$

metric:

$$ds^2 = -dt^2 + a^2 \frac{dr^2}{1 - kr^2} + r^2 d\Omega^2, \tag{1.5}$$

where k is the curvature of space-time and $d\Omega^2 = d\theta^2 + sen\theta^2 d\phi^2$.

As we have seen the FRW metric describes a four-dimensional curved space-time metric. However, when we introduce some massive object or some energy density, we need a theory capable of describing the mutual interaction between metric and energy. This theory is called **General Relativity** (GR) and it is a theory, developed by Albert Einstein, in which effects of gravity are a consequence of the curvature of four-dimensional space-time. The energy and momentum of all matter and radiation causes curvature in the Friedman-Robertson-Walker space-time and these potential wells hold masses and energy densities tied together.

In Euclidean space we can define a partial derivative operator that is no valid in a generic manifold, that is a topological space that resembles Euclidean space near each point. We need to introduce a new operator that is valid in an arbitrary space, which is reduced, in the case of flat space, in a partial derivative operator. This new operator valid in GR is the *covariant derivative*: $D_\mu = \partial_\mu + \Gamma^\nu_{\mu\sigma}$, where $\Gamma^\nu_{\mu\sigma}$ is the Christoffel symbol, that describes the effects of parallel transport in curved surfaces and, more generally, manifolds and it is defined as:

$$\Gamma^\nu_{\mu\sigma} = \frac{1}{2} g^{\nu\lambda} \left[\partial_\sigma g_{\lambda\mu} - \partial_\lambda g_{\mu\sigma} + \partial_\mu g_{\sigma\lambda} \right]. \tag{1.6}$$

From that, we can define the **Einstein tensor** as:

$$G_{\mu\nu} = R_{\mu\nu} - \frac{1}{2} g_{\mu\nu} R, \tag{1.7}$$

where $R_{\mu\nu}$ is the Ricci tensor and R is the Ricci scalar.

Starting from the cosmological principle we can approximate the universe as an isotropic fluid and we would like to find an equation which supersedes the Poisson equation of the Newtonian potential:

$$\nabla^2 \phi = 4\pi \rho_m G, \tag{1.8}$$

where ϕ is a gravitational potential, ρ_m is the mass density and G is the universal gravitational constant.

We can define at this point the principle of equivalence (PE), that tells us that in any local region of space-time, the effect of gravity can be transformed away, i.e. at each point of space-time it is possible to find a coordinate transformation such that the gravitational field variables can be eliminated from the field equations of matter [25]. This principle suggests that gravity is only a matter of geometry: an observer able to measure a portion of space to be flat is exactly in the same condition of another observer, elsewhere in the universe, who is measuring an equivalent flat space. Thus, considering GR as a classical field theory allows to a self-consistent derivation of the equations of motion:

$$G_{\mu\nu} = 8\pi G T_{\mu\nu}, \tag{1.9}$$

where $T_{\mu\nu}$ is the energy momentum tensor:

$$T_{\mu\nu} = \begin{pmatrix} T_{00} & 0 & 0 & 0 \\ 0 & T_{11} & 0 & 0 \\ 0 & 0 & T_{22} & 0 \\ 0 & 0 & 0 & T_{33} \end{pmatrix}. \tag{1.10}$$

Eq.(1.9) contains information about the variation of metric and curvature (left-hand side) and the source of the curvature due to matter and energy (right-hand side). Einstein's filed equation is a second order differential equation for the metric tensor, since we have a symmetric rank-2 tensor, there are 10 independent equations, however imposing some reasonable properties like a statement of energy conservation:

$$D_\mu T^{\mu\nu} = 0, \tag{1.11}$$

we can reduce the numbers of degrees of freedom to only 6 truly independent equations.

1.2 A hint of expanding universe: Hubble law and distances

In a comoving universe the definition of distance is itself a challenging issue, length are the estimations of distances: especially the one that light can have travelled since $t = 0$. In a time dt the light can travel a distance $dx = dt/a$, so we can define the total comoving distance as [2]:

$$\eta = \int_0^t \frac{dt'}{a(t')}, \tag{1.12}$$

this represents the maximum distance at which information can be propagated in a cosmological time t, in the comoving frame. Regions separated by distances greater than η are not causally connected. The corresponding physical distance is called the **cosmological horizon** and it is the farthest distance that we can observe today:

$$d_H(t_0) = a(t_0) \int_0^{t_0} \frac{dt}{a(t)}. \tag{1.13}$$

Using the FRW metric, see Eq.(1.4), we can introduce the definition of **proper distance**: a spatial geodesic measured along a hyper-surface of constant cosmic time, i.e. a geometric distance,

$$d_P(t) = a(t) \int_0^r \frac{dr'}{\sqrt{1 - kr'^2}}. \tag{1.14}$$

In the case of flat universe, k=0 and the proper distance becomes $d_P = a(t)r$. Furthermore in absence of peculiar motions in the comoving frame the relative velocity between two considered objects depends on their distance: $v = H_t d_P$. In the particular case in which $t = t_0$, we obtain the **Hubble Law**, i.e the relative velocity increases proportionally to the distance of the observed object and it is a strong probe of the expansion of the universe:

$$v = H_0 d_P. \tag{1.15}$$

In order to measure the amplitude of the Hubble parameter, H_0, we need to know the distance and the velocity of a certain object, which basically mean to know its redshift. This is an useful and rather simple to measure quantity. In order to give a definition of that, we consider two points in the space-time, connected together by a light signal. The source and the observer are both in their respective local rest frame. These two points are connected by a space-time interval $ds^2 = 0$. Considering two successive fronts of the electromagnetic wave: the first starts from the source with a time t_{em} and arrives to the observer at time t_{obs}; the second front wave starts at $t_{em} + \lambda_{em}$, where λ_{em} is the wavelength of the emitted photon at the source, and arrives to the observer at $t_{obs} + \lambda_{obs}$,

---

[2] From this point in advance we consider the CGS unit system in which c=1.

where λ_{obs} is the photon wavelength measured by the observer. The stretching of the wavelengths of the photons does not arise only from some effect equivalent to the Doppler effect in General Relativity, but from the universe expansion, that dilutes the photon energy in a larger portion of space. The photons may be redshifted due to modifications of the space-time properties or due to the presence of gravitational potentials along the photon path. A photon is redshifted when gets out a region with large gravitational potential and it is blue-shifted when enters a potential wells. If the source remained in the same position, this implies that the distance between source and observer remained constant. We can define the relation between the emitted and observed wavelength and the scale factor at emission and observed time:

$$1+z=\frac{\lambda_{obs}}{\lambda_{em}}=\frac{1}{a}. \tag{1.16}$$

This is a convenient definition of the **redshift**, z, that provides a simple way to measure time, distances and the stretching factor of the universe. It is relatively easy to measure the spectrum of a distant galaxy, in fact knowing how fast an object is receding from us translates into a distance information thanks to the Hubble law Eq.(1.15), and, since the velocity of recession is related to the expansion rate, we are measuring also the stretching factor a(t) of the universe. Of course if we assumed a negligible peculiar motion of the galaxy.
Nevertheless the most difficult part of the process to determine H_0 is the determination of the distance d_P. In certain conditions, e.g. in presence of a luminosity measurement of a standard candle, the redshift can be used to connect the proper distance and the luminosity distance of an object. The observed flux and the luminosity of the source are respectively:

$$\begin{aligned} F &= \frac{Nh\nu_{em}}{\Delta t_{em}}, \\ L &= \frac{Nh\nu_{obs}}{A\Delta t_{obs}}, \end{aligned} \tag{1.17}$$

where N is the number of photons, h is the Planck constant, ν_{em} is the frequency of emitted, em, or observed ,obs, photons and $A=4\pi d_p^2$ is the surface.
Since frequency and time intervals are redshifted, the flux in terms of luminosity takes the form:

$$F=\frac{L}{4\pi d_p^2(1+z)^2}. \tag{1.18}$$

So, from this, we can define the **luminosity distance** in term of proper distance as:

$$d_L = d_p(1+z). \tag{1.19}$$

In presence of a standard ruler, e.g. the radius of the acoustic horizon at the recombination epoch, we can define the **angular diameter distance** d_A in an Euclidean space as a function of the proper or the luminosity distance:

$$d_A = \frac{d_p}{1+z} = \frac{d_L}{(1+z)^2}. \tag{1.20}$$

Determinations of the angular diameter distance suffers the fact that in principle it is difficult to know the size l of generic objects.

1.3 An expanding universe

In order to have a simplified description of the dynamics of the universe, we consider a flat universe with constant curvature $k = 0$. Solving the 6 equations of the Eq.(1.9), we can derive the so called **Friedmann equations**.
Let's start from the time-time component of the Eq.(1.9):

$$G_{00} = 8\pi G T_{00}, \tag{1.21}$$

we obtain the first Friedman equation:

$$H^2 = \left(\frac{\dot{a}}{a}\right) = \frac{8\pi\rho G}{3}, \tag{1.22}$$

here ρ is the energy density and H is the **Hubble parameter** and it is used as the unit of measurement to describe the expansion of the universe.
It is possible approximate the energetic content as energy density and pressure, so it is correct to assume the **perfect fluid** notation:

$$T_{\mu\nu} = (\rho + P)V_\mu V_\nu - P g_{\mu\nu}, \tag{1.23}$$

where P is the pressure and V_μ is the 4-velocity vector.
Eq.(1.22) tells us that the Hubble parameter depends on the energy content of the universe and it is not constant during the evolution. Therefore, the Hubble parameter is a local quantity that can be measured only in the local universe.

Considering the first Friedman equation and the space-space component i.e. $g_{ij} = \frac{k}{3}T_{ij}$, we obtain the **acceleration equation** [43]:

$$\frac{\ddot{a}}{a} = -\frac{4\pi G}{3}(3P + \rho), \tag{1.24}$$

where P is the pressure of a perfect fluid. In order to study the dynamics of the universe (homogeneous and isotropic) we can define the matter content in terms of its energy momentum tensor $T_{\mu\nu}$.
If $\rho + 3P < 0$ the cosmic expansion would be accelerated. Putting together the Eqs. (1.22) and (1.24) we obtain the continuity equation:

$$\dot{\rho} = -3H(P + \rho). \tag{1.25}$$

At this point we have three equations and four variables, so we need another equation in order to solve the system and a useful choice is to use the equation of state of a gas of particles:

$$P = \omega\rho, \tag{1.26}$$

where ω is a constant determining the properties of the particle component. Thus the continuity equation can be rewritten as a function of the parameter ω in the following way:

$$\dot{\rho} = -3H\rho(\omega + 1) \rightarrow \rho = \rho_0 a^{-3(1+\omega)}, \tag{1.27}$$

where ρ_0 is the density evaluated today.
Moved by the common knowledge and by his beliefs, in order to have a static description of the universe, around the 1929, Einstein introduced a constant term Λ, in Eq.(1.21), that does not violate the covariance derivative of the Einstein tensor. So the "new" Friedman equations became:

$$H^2 = \frac{8\pi\rho G}{3} - \frac{k}{a^2} + \frac{\Lambda}{3}, \tag{1.28}$$

$$\frac{\ddot{a}}{a} = -\frac{4\pi G}{3}(3P + \rho) + \frac{\Lambda}{3}. \tag{1.29}$$

For a flat Λ dominated universe, the first Friedmann equation takes the form:

$$H_0 = \frac{\dot{a}}{a} = \left(\frac{8\pi\rho_\Lambda G}{3}\right)^{\frac{1}{2}}. \tag{1.30}$$

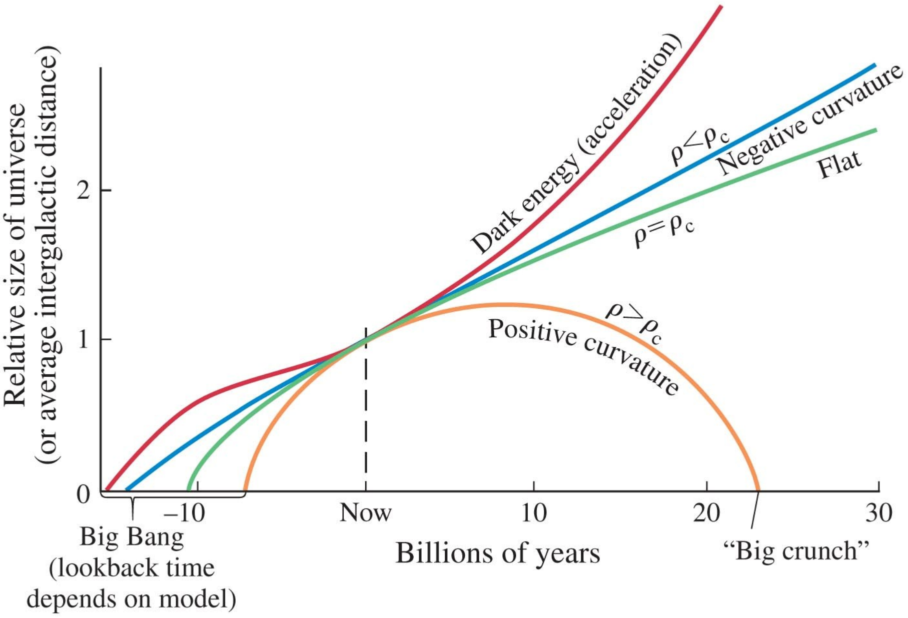

Figure 1.1: *Different possible scenarios of the evolution of the universe for different density values.*

Leading to an exponentially expanding scale factor,

$$a(t) = e^{H_0(t-t_0)}. \tag{1.31}$$

1.3.1 Cosmological parameters

We can define the **critical density** that is the average density of matter required for the universe to just halt its expansion, but only after an infinite time:

$$\rho_c(t) = \frac{3c^2H^2(t)}{8\pi G}. \tag{1.32}$$

Let's consider a comparison between a generic density of the universe ρ and the critical density ρ_c (see Fig.1.1).
If the density of the universe is bigger then a critical density ($\rho > \rho_c$) we have a positive curvature, so a close universe (yellow line). If the density of the universe is smaller then a critical density ($\rho < \rho_c$) we have a negative curvature, so an open universe (blue line). If the density of the universe is equal to the critical density ($\rho = \rho_c$) we have k equal to 0, so a flat universe (green line). So, the statement about the evolution of the Universe is true for $\Lambda = 0$ only.

Form this discussion about the curvature parameter, we can introduce a **density parameter**:

$$\Omega_i(t) = \frac{\rho_i(t)}{\rho_c(t)}, \tag{1.33}$$

where i defines the contribution of the considered component.
Under this formalism Eq.(1.22) takes the following form:

$$H = H_0\sqrt{\Sigma_i \Omega_i a^{-3(1+\omega)}}, \tag{1.34}$$

for a spatially flat universe the sum of all contributions must be $\Omega_{tot} = 1$.
In Table 1.1 are shown the densities of various species scales which as different powers of a.
We can rewrite the Friedman equation as a sum of contributions:

$$H = H_0\sqrt{\Omega_{m0}a^{-3} + \Omega_{r0}a^{-4} + \Omega_{\Lambda 0}} \tag{1.35}$$

where Ω_{m0} is the density parameter for non-relativistic matter today, Ω_{r0} is the density parameter for relativistic matter and $\Omega_{\Lambda 0}$ is the density parameter for dark energy. Looking the Eq.(1.35) it is evident that different species dominate at different ages. Radiation or relativistic matter is more important at early times, when the scale factor is small, but at a certain time non-relativistic matter starts to be the dominant part in terms of energy contribution. Finally when the expansion has diluted matter and radiation components, the age of cosmological constant domain starts. The exact time of transition between two regimes depends on the amount of the constituents. In Fig.1.2 we show the different expansion regimes in the case of a three component model (matter+radiation+cosmological constant) [88].

Table 1.1: *The values for ω, ρ and $a(t)$ for different era of the universe.*

	ω	ρ	a(t)
Non relativistic matter (baryon,dark matter)	0	a^{-3}	$t^{\frac{2}{3}}$
Relativistic matter or radiation	$\frac{1}{3}$	a^{-4}	$t^{\frac{1}{2}}$
Cosmological constant (dark matter)	-1	e^{Ht}	$t^{\frac{1}{2}}$

At this point we can define the ratio between matter and radiation:

$$\frac{\Omega_m}{\Omega_r} = \frac{\rho_m(t)}{\rho_c(t)}\left(\frac{\rho_r(t)}{\rho_c(t)}\right)^{-1} = \frac{\rho_m}{\rho_r} = \frac{\rho_{m,0}}{\rho_{r,0}}a(t). \tag{1.36}$$

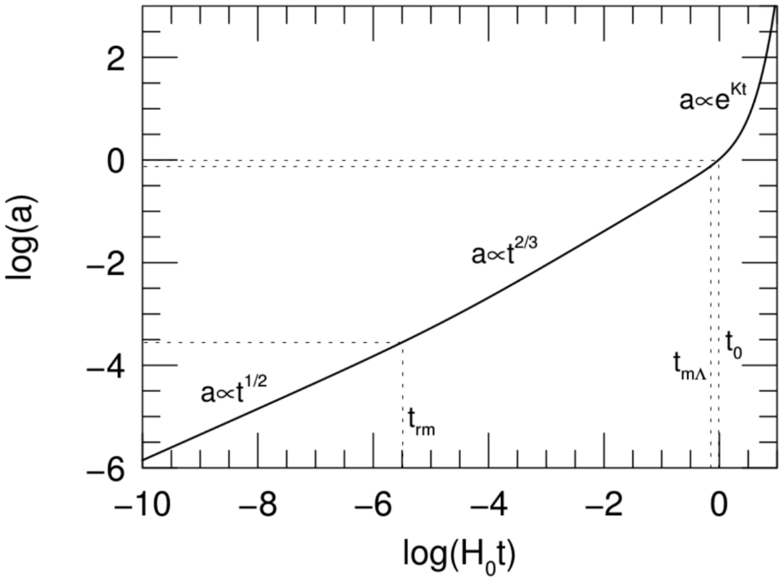

Figure 1.2: *The scale factor, a, as a function of the time measured in units of Hubble constant H_0. The parameter used are $\Omega_{m,0} \sim 0.3, \Omega_{r,0} \sim 10^{-5}, \Omega_{\Lambda,0} \sim 0.7$ and $\Omega_{k,0} = 0$ [88].*

If $\Omega_m/\Omega_r < \rho_{m,0}/\rho_{r,0}a(t)$, the universe is dominated by relativistic particles: neutrinos and photons. Under this condition the universe is dominated by radiation. On other hand, if $\Omega_m/\Omega_r > \rho_{m,0}/\rho_{r,0}a(t)$, the universe is dominated by non relativistic matter: baryons and cold dark matter (CDM). So, the dominant component in this particular case is the matter.
Similarity, we can define the ratio between matter and Λ:

$$\frac{\Omega_\Lambda}{\Omega_m} = \frac{\rho_\Lambda(t)}{\rho_c(t)}\frac{\rho_c(t)}{\rho_m(t)} = \frac{\rho_\Lambda}{\rho_m} = \frac{\rho_{\Lambda,0}}{\rho_{m,0}}a^3(t). \tag{1.37}$$

If $\Omega_\Lambda/\Omega_m < \rho_{\Lambda,0}/\rho_{m,0}a^3(t)$, the universe is dominated by matter otherwise the cosmological constant contribution is the dominant part.

1.4 Boltzmann equations

The standard cosmological model, as described above, give us a description of the space-time dynamics and a set of thermodynamic quantities that ensure a complete description of both relativistic and non relativistic energetic content of the universe. The first approximation in order to have a rough indication of these dynamics is to consider a reaction that starts from 2 particles and give us two particles and the associated ratio between the scattering rate Γ of the species and the Hubble rate of expansion H:

$$\begin{aligned} \Gamma > H &\Rightarrow \textit{coupled} \\ \Gamma < H &\Rightarrow \textit{decoupled} \end{aligned} \tag{1.38}$$

It is possible to define:

$$\Gamma = n < \sigma v > . \tag{1.39}$$

Here v is the average velocity of the particles, σ is the interaction cross section and H is the Hubble rate. All the information about how particles are distributed among momentum eigenstates is contained in the probability distribution function, $f(\overrightarrow{p})$. The number density of particles is:

$$n = \frac{g}{(2\pi)^3} \int d^3p \; f(\overrightarrow{p}), \tag{1.40}$$

where g is the internal degrees of freedom of the particles.

Particles are divided into two classes: fermions and bosons. In thermodynamic equilibrium fermions follow the Fermi-Dirac distribution (+), while bosons follow the Bose-Einstein distribution (-):

$$f(\overrightarrow{p}) = \frac{1}{e^{(E-\mu)/T} \pm 1}. \tag{1.41}$$

At equilibrium the distribution function depends on two parameters: temperature (T) and chemical potential (μ).

In order to reconstruct the phase-space evolution of the distribution function is to provide an equation able to merge the behaviour of the thermodynamic quantities with the metric evolution, the Boltzmann transfer equation:

$$\widehat{L}[f(E,t)] = \widehat{C}[f(E,t)], \tag{1.42}$$

where $\widehat{C}$ is the collisional term and $\widehat{L}$ is the Louville operator:

$$\widehat{L} = p^{\mu}\frac{\partial}{\partial x^{\mu}} - \Gamma^{\mu}_{\nu\gamma} p^{\nu} p^{\gamma} \frac{\partial}{\partial x^{\mu}}. \tag{1.43}$$

From that we can rewrite the left hand term of Eq. (1.42) as:

$$\widehat{L}[f(E,t)] = E\frac{\partial f}{\partial t} - H|\overrightarrow{p}|^2\frac{\partial f}{\partial E}. \tag{1.44}$$

At this point, we are able to find the evolution of the number density of a species that describes a change in number density due to the Hubble rate of expansion and to interactions, by multiplying the above equation by $\frac{g}{2\pi}$ and integrating over the momentum:

$$\frac{dn_i}{dt} + 3Hn_i = \frac{g_i}{2\pi^3}\int C[E_i,t]\frac{d^3p_i}{E_i}. \tag{1.45}$$

We can rewrite the collisional term of the Boltzmann equation, assuming thermal equilibrium, as:

$$\frac{dn_i}{dt} + 3Hn_i = -\int d\Pi_1 d\Pi_2 d\Pi_3 d\Pi_4 (2\pi)^4|M|^2\delta^4(p_3+p_4-p_2-p_1)[f_1f_2 - f_3f_4]. \tag{1.46}$$

Where the subscripts are the term of a binary process $1+2 \leftrightarrow 3+4$, $d\Pi_i = (g_i/2\pi^3)(d^3p_i/E_i)$ is the momentum space and the $|M|^2$ is the matrix containing the scattered amplitudes.

We have that two processes may happen: 1) the temperature of the fluid becomes lower than the mass of the species x ($T < m_x$) and the relativistic to non relativistic transition occurs; 2) the interaction rate of the binary scattering processes becomes smaller than the Hubble rate of expansion preventing the $2 \leftrightarrow 2$ interactions. If the interaction rate becomes smaller than the Hubble rate, see Eq.(1.38) the given species can have a significant relic abundance today. In this case the Boltzmann equation can be rewritten as:

$$\frac{1}{a^3}\frac{d(n_1a^3)}{dt} =< \sigma v > \left[n_1n_2 - \left(\frac{n_1n_2}{n_3n_4}\right)_{eq} n_3n_4\right]. \tag{1.47}$$

Where n_{eq} is the number density calculated at the equilibrium. We can rewrite the last equation in terms of comoving density $N_i \equiv n_i/S$ (where S is the entropy density):

$$\frac{dlnN_1}{dlna} = -\frac{\Gamma_1}{H}\left[1 - \left(\frac{N_1N_2}{N_3N_4}\right)_{eq}\frac{N_3N_4}{N_1N_2}\right]. \tag{1.48}$$

Where $\Gamma_1 = n_2 < \sigma v >$ and the right-hand side of the equation describes the interaction efficiency. When $\Gamma \gg H$ the system evolves in function of the comoving number density: if $N_1 \gg N_1^{eq}$ the interaction efficiency results negative and particles of type 1 are destroyed during the scattering (or annihilation) process. On the other hand if $\Gamma \ll H$ the right-hand side of equation gets suppressed and N_1 goes asymptotically to a constant value.

1.5 The standard cosmological model

Considering the mathematical frame described so far and in agreement with the standard model of particles, we are able now to successfully describe the thermal history of the universe. Starting from the fact that the recession of the galaxies has been observed and that we can consider the universe is an isolated system, we can infer to live in an adiabatically and expanding cooling universe. Thus going back in time, it must have been denser and hotter at early times. Under these assumptions data and observations suggest that the universe is born approximatively 13.8 Gyr [8] ago from a space-time singularity commonly called Big Bang (BB). The temperature was very hot and all the matter was trapped in a photon-baryon fluid in a plasma state in thermodynamic equilibrium. The matter is fully ionized and photons interact with baryons through the Thomson scattering and therefore the mean free path is very small, see Fig.1.3.
The universe that comes out can be, on large scales, approximated as a homogeneous and isotropic system. The main evidence of the latter statement is the Cosmic Microwave Background (CMB), that is the sea of photons that permeates the universe and that scattered the last time (on the so called Last Scattering Surface LSS) when the universe was about 1000 times hotter than today. This sea is considered a thermal echo of the Big Bang and it is the main data source for all the cosmological studies because it contains a huge amount of information about the early stage of the universe. In this section we will see in details how the standard cosmological model is in good agreement with the observational data.

1.5.1 Nucleosynthesis: Formation of the first elements

After the accelerated expansion produced by the inflation (see Sec. *1.5.3*), the universe continues to expand. Having to deal with an expanding universe means to describe physics inside a cooling system which is in local thermodynamic equilibrium, where local thermodynamic equilibrium means that we can consider

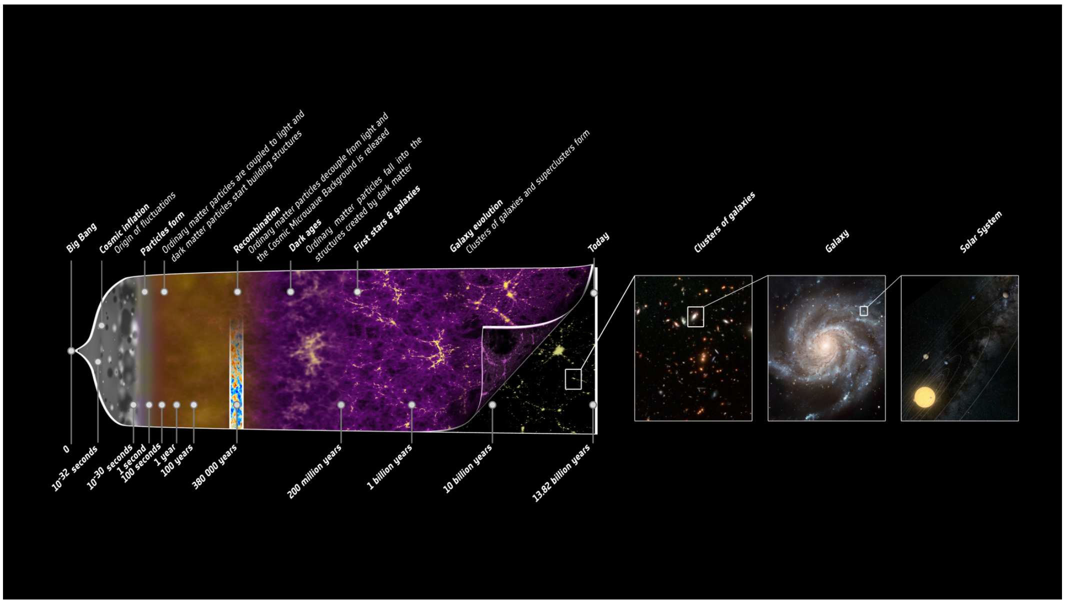

Figure 1.3: *Principal phases of the evolution of the universe in agreement with the Cosmological Standard Model (credits ESA: http://www.esa.int/ESA).*

the fluid in equilibrium in a small enough range of time. In this framework two main processes take place and affect the equilibrium of the primordial plasma: decoupling of the known interactions and transition between relativistic and non-relativistic behaviour of the species. The first process happens when the scattering rate of interactions falls below the Hubble expansion rate $\Gamma = n < \sigma v > \ll H(t)$ and it is called decoupling. The second process takes place as soon as the temperature of the fluid falls below the mass of the particles $T \ll m$ (freezout). The weak interaction goes out of equilibrium very quickly ($\propto T^2$) once the mean temperature of the primordial fluid is less then 1 MeV. This process is also called as neutrino **decoupling** and leads to a conservation of the number density called **freeze-out**. Here neutrinos, that have been in equilibrium due to weak interactions:

$$\begin{aligned} \nu_e + \overline{\nu}_e &\leftrightarrow e^+ + e^-, \\ e^- + \overline{\nu}_i &\leftrightarrow e^- + \overline{\nu}_i, \end{aligned} \tag{1.49}$$

decouple from the rest of the components, that means the reactions shown above no longer occur. We know that neutrinos were ultra-relativistic at the decoupling time, due to their tiny masses, as suggested by the fact that we measure their flavour oscillations, and their distribution function in thermal equilibrium was a

Fermi-Dirac; thus when they decouple from the rest of the plasma they preserve their distribution.
After 1 second from the Big Bang when the temperature of the universe is of a few Mev, protons and neutrons are no longer relativistic and their number densities follow the Maxwell-Boltzmann distribution.
Until weak interactions are in equilibrium ($t < 1s$) neutrons decay is a negligible process and we have to consider the following reactions:

$$\begin{aligned} n + \nu_e &\leftrightarrow p^+ + e^-, \\ n + e^+ &\leftrightarrow p^+ + \overline{\nu}_e. \end{aligned} \tag{1.50}$$

Neutrons have larger masses with respect to protons and they decay through weak interactions in:

$$n \rightarrow p^+ + e^- + \overline{\nu}_e. \tag{1.51}$$

However, after neutrino decoupling the neutron to proton ratio remains almost constant except for neutrons decay, thus we can define the neutron to proton ratio, at equilibrium, as:

$$\left(\frac{n_n}{n_p}\right)_{eq} = \left(\frac{m_n}{m_p}\right)^{3/2} e^{-Q_n/T}, \tag{1.52}$$

where Q_n is the binding energy. Basically, Eq.(1.52), shows us the exponential drop of the neutron to proton ratio once the mean temperature of the fluid is $T \ll Q_n$. The freezeout happens well before exponential decay.
The processes which takes into account neutrons described so far is fundamental, it sets the initial condition for the nucleosynthesis of the light elements in the primordial universe. Indeed we have to consider that other reactions are in equilibrium in the primordial plasma:

$$\begin{aligned} p^+ + p^+ &\leftrightarrow D + e^+ + \overline{\nu}_e, \\ n + n &\leftrightarrow D + e^- + \nu_e, \\ n + p^+ &\leftrightarrow D + \gamma, \end{aligned} \tag{1.53}$$

the first two processes are suppressed with respect to the third one because of the Columbian repulsive potential between two equally charged particles and the weakness of the weak interaction respectively. While the third one is the so called **Deuterium nucleosynthesis**. The binding energy of deuterium is $Q_D = m_n + m_p - m_D = 2.22MeV$, we can write an equation for the deuterium to proton ratio:

$$\left(\frac{n_D}{n_p}\right)_{eq} \simeq \eta \left(\frac{T}{m_p}\right) e^{Q_D/T}, \tag{1.54}$$

where η is the baryon-to-photon ratio in the range of $(5.1 - 6.5)^{-10}$ [77].
Eq.(1.54) is expressed in terms of the baryon-to-photon ratio in order to put in evidence that the production of D is inhibited until the temperature drops well beneath the binding energy Q_D. When the mean temperature of the primordial fluid drops below $T \sim 0.2MeV$, helium cannot form directly, the density is too low and there is not enough time, so the following process occur:

$$\begin{aligned} D + p^+ \leftrightarrow^3 He + \gamma, \\ D +^3 He \leftrightarrow^4 He + p^+. \end{aligned} \tag{1.55}$$

in which deuterium is consumed forming helium. When the temperature decreases at $T \sim 4 \cdot 10^8 K$ the nucleosynthesis ends. Baryons are mainly in form of free protons or ^4He. Since there are no stable elements with atomic mass number of A = 5 and A = 8 is not possible to produce heavy elements during nucleosynthesis, in fact the ^8Be is unstable and decays into two ^4He and ^5He has short life. The radiation dominates until $t \sim 0.47MYr$, after this age the matter became the dominant component.

1.5.2 Recombination, decoupling and last scattering surface

At $T \geq 1eV$ the primordial soup is made of e^-, γ, p^+ and the light nuclei produced during Big Bang Nucleosynthesis.
Neutrinos are free-streaming and do not influence directly the dynamics. In this situation electromagnetic interaction guarantee the process:

$$p^+ + e^- \leftrightarrow H + \gamma, \tag{1.56}$$

which does not provide the formation of neutral matter because of the great efficiency of the photo-dissociation process.
The equilibrium abundance ratio among hydrogen atoms, protons and electrons is given by:

$$\left(\frac{n_H}{n_e n_p}\right)_{eq} = \frac{g_H}{g_e g_p} \left(\frac{2\pi m_h}{T m_e m_p}\right)^{3/2} e^{\frac{Q_H}{T}}, \tag{1.57}$$

with $Q_H = 13.6eV$ is the binding energy of the hydrogen atom.
When 90% of electrons are bound with protons the mean temperature is $T_{rec} \sim 0.3eV$, it is almost two orders of magnitude lower than the hydrogen binding energy. As we have also seen during the primordial nucleosynthesis the great number of photons increases the statistical weight of the tail of photon distribution, so, when the mean temperature is of the order of Q_H, there are still too many photons with $T \gg 13.6eV$ that prevent recombination. When hydrogen recombines, the free electron density drops down quickly and, photons inside the plasma, that were kept tied by Compton scattering, no longer interact and start to stream in a neutral universe. This process takes the name of **photon decoupling**. We find that decoupling happened at $T_{dec} \sim 0.27eV$ and $t_{dec} \sim 380000Yr$. These processes originate the **Last Scattering Surface** that, compared with the universe time scale, is the last moment when photons interact with the primordial plasma. Now photons are free to travel in the universe that is transparent to electromagnetic radiation. These photons carry on information of the pre-last-scattering universe, this relic radiation is known as **Cosmic Microwave Background** (CMB) radiation and it is one of the most important discoveries of mankind. We will describe all the properties of CMB in Chapter 2.

1.5.3 Inflation model

The cosmological standard model suggests that at early time the universe has had an epoch of exponential expansion called **inflation** [98]. During this epoch the universe was dominated by a scalar field which probably originated a positive energy very similar to what we call cosmological constant (Λ_i). The inflation produced a quasi-exponential expansion of the universe that was stretched by a factor:

$$\frac{a(t_f)}{a(t_i)} \sim e^{-N}, \tag{1.58}$$

where N is the number of e-foldings of inflation: $N \equiv H_i(t_f - t_i)$.
In litterature there is a variety of inflationary models [62, 68] which have different initial conditions, dynamics and exit from inflationary period. With particle generation and reheating of the universe, the simplest model is the single scalar field (ϕ) **slow-roll** model that we will describe later. The necessity of an inflationary epoch rises from some observational and theoretical issue known as: **Flatness problem, Horizon problem and Monopole problem** [90, 98].

Flatness problem

The standard cosmological model predicts that any initial difference between ρ and ρ_c, Eq.(1.33), grows with time. The hypothesis of a flat universe [4] in the present days, recently confirmed by cosmological data, therefore, requires an initial value of the total energy density very close to the critical one: $\rho/\rho_c \ll 10^{-60}$. This fine tuned initial conditions are statistically very unlikely and so, the flatness problem has a statistical nature. From the Eq.(1.35) we can define, considering $a = a_0 = 1$:

$$\Omega_{tot} - 1 = \frac{k}{H(t)^2 a^2}. \tag{1.59}$$

Looking back in time $\Omega_{tot} - 1$ becomes smaller and smaller. In order to quantify the magnitude, we can compare the total densities parameters in the radiation epoch:

$$\frac{\Omega_{tot} - 1 \mid_{t=t_{early}}}{\Omega_{tot} - 1 \mid_{t=t_{late}}} \simeq 10^{-64}. \tag{1.60}$$

This is a fine-tuning problem of 64 orders of magnitude which is difficult to reconcile, on the other hand inflation provides a suitable solution by considering the exponential evolution of the universe that stretches the initial curvature dramatically to become very close to one independently from the initial value.

Horizon problem

The horizon problem arises due to the difficulty in explaining the observed homogeneity of causally disconnected regions of space, at the LSS, in the absence of a mechanism that sets the same initial conditions everywhere. Taking a light-like metric $ds^2 = -dt^2 + adx^2 = 0$, the horizon distance or the distance travelled by a photon at the last-scattering time is d_{hor} ∼0.4 Mpc. Using Eq.(1.20) it is possible to find the angular size of a causally connected region on the LSS: $\theta_{hor} \sim 1.6$ deg.
The solution of this problem is given basically making H^{-1} constant during the entire inflationary process of expansion. The perturbation mode, during this epoch, grows larger than the horizon and then comes back inside the horizon, which grows slower during radiation domination.

Monopole problem

The monopole problem consists in the absence today of magnetic monopoles in the universe. If the early universe was very hot, a large number of very heavy and stable magnetic monopoles have been produced ($m \sim 10^{16}$ GeV). This is a problem with Grand Unified Theory (GUT), which proposes that at high temperatures the electromagnetic, strong and weak nuclear forces are not actually fundamental forces but arise due to spontaneous symmetry breaking from a single gauge theory. These theories predict a number of heavy, stable particles that have not yet been observed in nature. Solution comes from the fact that the magnetic monopoles were created before inflation and therefore their density was diluted by the exponential expansion up to a point when their contribution to the cosmological fluid is irrelevant and, therefore, it is extremely unlikely to observe them.

1.5.4 Physics of inflation

The basic idea under inflation is the spontaneous symmetry breaking mechanism: above a given energy scale it existed a symmetry, i.e. an invariance of the theory. In its simplest form, we introduce a scalar field ϕ called **inflaton**, thus we can write the Klein-Gordon action:

$$A = \int d^4x\sqrt{-g}\left[\frac{1}{2}\partial^\mu\phi\partial_\mu\phi + V(\phi)\right], \tag{1.61}$$

where $V(\phi)$ is the potential. As usually in classic field theory, solving the Euler-Lagrange equation leads to the equation of motion:

$$\ddot{\phi} + 3H\dot{\phi} + \frac{dV(\phi)}{d\phi} = 0. \tag{1.62}$$

The second term $3H\dot{\phi}$ corresponds to the velocity term weighted by the Hubble parameter, it behaves like a Hubble friction.
We can rewrite the Friedman equations during the period dominated by the scalar field component:

$$H = \sqrt{\frac{8}{3}\pi G\left(\frac{1}{2}\dot{\phi} + V(\phi)\right)}. \tag{1.63}$$

Whit these equations we can write the second **Friedman equation**:

$$\dot{H} = -4\pi G\dot{\phi}. \tag{1.64}$$

Assuming that the fractional change between $\dot{H}$ and H during the expansion time is negligible, we get:

$$\ddot{\phi} \ll\mid V(\phi) \mid . \tag{1.65}$$

This condition implies that $P = -\rho$ and so:

$$H \simeq \sqrt{\frac{8}{3}\pi G V(\phi)}. \tag{1.66}$$

In the slow roll model [67] it is also assumed that the ratio between $\ddot{\phi}$ and $\dot{\phi}$ must be much less than the unity: $\ddot{\phi} \ll H\dot{\phi}$, in such a way it is possible to drop the inertial term and obtain the new equation of motion:

$$\dot{\phi} = -\frac{V'(\phi)}{3}. \tag{1.67}$$

Putting together all these considerations it is possible to write the flatness conditions for the potential, in order to allow a slow roll motion of the inflaton field:

$$\begin{gathered} \frac{V'(\phi)}{V(\phi)} \ll H, \\ \frac{V''(\phi)}{V(\phi^2)} \ll H^2 \ . \end{gathered} \tag{1.68}$$

In the **slow roll** model we suppose that the potential underwent a shift in a finite time from an initial value to a final one. The decreasing of the inflaton filed translates into a exponential increase of the scale factor.

During the inflation the inflaton potential contained the largest part of the energy density. When inflation ends the energy of the potential had been transformed in kinetic energy of the inflaton that decays heating the universe and allowing the generation of particles, in the process called **reheating**.

We can rewrite the equation of motion considering that the field ϕ oscillates in the bottom of the potential:

$$\ddot{\phi} + 3H\dot{\phi} = -m^2\phi, \tag{1.69}$$

where m is the mass associated to the minimum of $V(\phi) = \frac{1}{2}m^2\phi^2$. When the expansion rate becomes larger than the oscillation period $H^{-1} \gg m^{-1}$ the friction term can be neglected and the oscillatory pattern becomes dominant. At this point the particles created underwent scattering processes that will thermalize the primordial plasma. The reheating temperature depends on the energy density at the end of the reheating epoch.

Scalar perturbations

If the expansion of the universe is slow enough, particles have enough time to settle close to local equilibrium since the universe is homogeneous. In quantum mechanics, due to uncertainty principle $\Delta p \Delta x \geqslant \hbar/2$, the momentum of a particle can be described only considering a finite volume V. If we want to solve the Schroedinger equation inside this box, we obtain the energy and momentum eigenstates. Pose our attention on the uncertainty principle, every quantum-mechanical quantity have some variance. The local differences in time:

$$\delta\phi(\overrightarrow{x}, t) = \phi(\overrightarrow{x}, t) - \phi(\overline{\phi}t), \tag{1.70}$$

implies different inflation durations and consequently different end times. Moreover, quantum fluctuations in time translates into local classical spatial fluctuations [15].

In Fourier space the whole set of perturbations can be factorized in single k-modes allowing to write a distribution having zero mean and non-zero variance. Considering the conservation of the energy momentum tensor in the Fourier space it is possible to write the scale invariant **power spectrum** as:

$$\mathcal{P}_\phi = \frac{8\pi H^2}{9k^3 m^2_{planck}} \ . \tag{1.71}$$

From this we can understand that all the perturbation have the same initial amplitude independently from k. Consequently, the primordial power spectrum is also called "scale-invariant"; this means that, after the horizon crossing, all the perturbations have the same amplitude. On the other hand, after the horizon crossing, perturbations are super-horizon and, thus, their evolution is driven uniquely by the quantum fluctuations that, due to the accelerated expansion, now are metric perturbations.

More generally, we can write the primordial power spectrum for scalar perturbations as:

$$\Delta^2_S(k) = A_S(k_0)\left(\frac{k}{k_0}\right)^{n_S - 1} , \tag{1.72}$$

where Δ_S is the normalized version of the power spectrum and k_0 is a reference scale (pivot). Inflation predicts a value of N_S very close to 1 as explained above.

Tensor perturbations

Inflation generates, also, primordial tensor perturbations.
This harmonic behaviour leaves an imprint during the accelerated expansion generated by the inflaton field. Hence we can write, in analogy to what done for the scalar perturbations, a tensor perturbation normalized power spectrum:

$$\Delta_T^2(k) = A_T(k_0)\left(\frac{k}{k_0}\right)^{n_t}, \tag{1.73}$$

and we can define the **tensor-to-scalar ratio** as:

$$r = \frac{A_T}{A_S} \tag{1.74}$$

where A_T is the tensor amplitude and A_S is the scalar amplitude and are defined respectively as:

$$\begin{aligned} A_T &\cong \frac{3}{2\pi^2}\frac{V}{M_{planck}^4}, \\ A_S &\cong \frac{1}{24\pi^2\epsilon}\frac{V}{M_{planck}^4}. \end{aligned} \tag{1.75}$$

Where ϵ is a slow-roll parameter. The r parameter impacts on the power spectra shown in Fig. 1.4. Actually there is not a theoretical prediction for the r parameter, there are too many inflationary models that can originate a great variety of tensor-to-scalar ratio values, this means that, in principle, it is always possible to consider the observation not sensitive enough.

1.6 Cosmological parameters

The ΛCDM model, as we have described in this chapter, is in very good agreement with the cosmological observations. It is based on six parameters:

1. $\Omega_b h^2$: baryonic density;
2. $\Omega_c h^2$: dark matter density;
3. $100\theta_{MC}$: ratio of the angular diameter distance at the last scattering surface sound horizon;

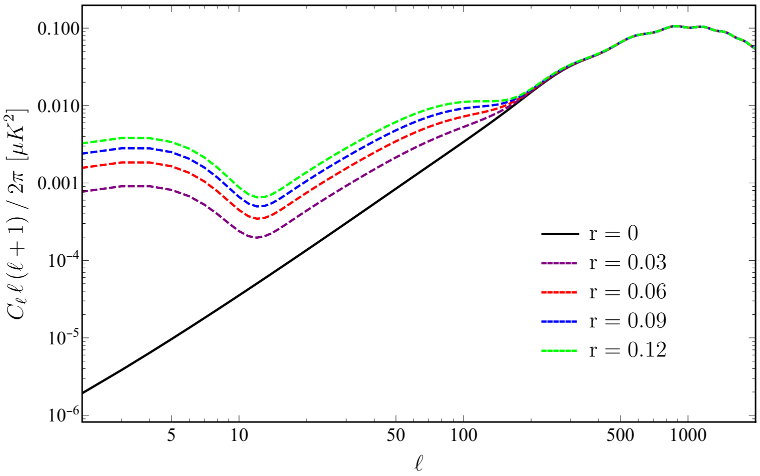

Figure 1.4: *Impact of tensor-to-scalar ratio on the BB power spectrum.*

4. τ: reionization optical depth;
5. n_s: scalar spectral index;
6. $ln(10^{10}A_s)$: amplitude of scalar perturbations.

The last values that the Planck experiment has revealed [8] are summarized in the Table 1.2.

Parameters	**Best fit**	68% **limits**
$\Omega_b h^2$	0.022383	0.02237 ± 0.00015
$\Omega_c h^2$	0.12011	0.1200 ± 0.0012
$100\theta_{MC}$	1.040909	1.04092 ± 0.00031
τ	0.0543	0.0544 ± 0.0073
n_s	0.96605	0.9649 ± 0.0042
$ln(10^{10}A_s)$	3.0448	3.044 ± 0.014

Table 1.2: *Six pillars for ΛCDM model [8].*

1.7 Perturbation theory

As we can see in previous section the zero order distribution function coincides with the Bose-Einstein distribution, Eq.(1.41) for bosons (-), or with the Fermi-Dirac Eq.(1.41) depending for fermions (+). In this section we will describe the perturbation equations for the various components of the universe.

1.7.1 Photons

It is possible write the first order of the distribution function for photons, introducing the temperature perturbation $\Theta = \frac{\delta T}{T}$, as:

$$f \simeq f_0 - \frac{\partial f_0}{\partial p}\, p\, \Theta\ . \tag{1.76}$$

Expliciting the perturbed Boltzmann equation we obtain:

$$\frac{df(\overline{x};t;P^{\mu})}{dt} = \frac{\partial f}{\partial t} + \frac{\widehat{p}^i}{a}\frac{\partial f}{\partial x^i} - p\frac{\partial f}{\partial x^i} - p\frac{\partial f}{\partial p}\left[H + \frac{\partial \phi}{\partial t} + \frac{\widehat{p}^i}{a}\frac{\partial \psi}{\partial x^i}\right] = C(f), \tag{1.77}$$

where C_ℓ is the collision operator.
We can approximate this equation in two different ways:

1. **Zeroth order approximation** ($\phi = 0$ and $\psi = 0$):

   $$\left.\frac{df}{dt}\right|_0 = \frac{\partial f^0}{\partial t} - pH\frac{\partial f^0}{\partial p} = 0. \tag{1.78}$$

   This equation is equal to zero because we have no collisions. We can rewrite this equation in terms of temperature T:

   $$\frac{\partial f^0}{\partial p}\left[-\frac{1}{T}\frac{dT}{dt} - \frac{da}{dt}\frac{1}{a}\right] = 0, \tag{1.79}$$

   and the solution of this equation gives us that the expansion of the universe is reflected in the cooling of its temperature:

   $$T \propto \frac{1}{a}. \tag{1.80}$$

2. **First order approximation**:

$$\left.\frac{df}{dt}\right|_1 = -p\frac{\partial f^0}{\partial t}\left[\frac{\partial \Theta}{\partial t} + \frac{\widehat{p}^i}{a}\frac{\partial \Theta}{\partial x^i} + \frac{\partial \phi}{\partial t} + \frac{\widehat{p}^i}{a}\frac{\partial \psi}{\partial x^i}\right]. \tag{1.81}$$

   The first two terms in the brackets produces a free streaming, i.e. anisotropies on increasingly small scales as the universe evolves. The second two terms account for the effect of gravity.

Considering the influence of Compton scattering on the distribution function for photons, the process that we will study is:

$$e^- + \gamma \rightleftarrows e^- + \gamma. \tag{1.82}$$

If we are in a non relativistic case, for Compton effect, we have a small transfer of energy and $p \sim p'$ (p is the momentum of e^- and p' is the momentum of the scattered e^-) and $q >> p$ or p' (q is the momentum of γ). Also the energy of electrons is very small so $q = q'$ (q' is the momentum of the scattered γ), i.e. $E_p \sim E_{p'}$. The value of $f_e(q)$ gives us the exact number density of electrons n_{e^-}. With these considerations it is possible to write the collision term as:

$$C[f(\overline{p})] = -p\frac{\partial f^0}{\partial p} n_e \sigma_{Th}\left[\Theta_0 - \Theta(\overline{p}) + \overline{p}\cdot\overline{v}_b\right]. \tag{1.83}$$

Here we have a contribution of *monopoles*, it does not depend on the direction vector, it is an integral of the perturbation over all directions:

$$\Theta_0 = \frac{1}{4\pi}\int d\Omega' \Theta(\widehat{p'}; \overline{x}; t). \tag{1.84}$$

There is not zero order term and, if we have a peculiar velocity, it refers to the components of a receding galaxy's velocity that cannot be explained by Hubble's law. So, $v_b = 0$ and the Compton scattering is very efficient, only the monopole perturbation survives and all other moments are zero. On the other hand, if we have a value of $v_b \neq 0$ in the collisional term appears a *dipole* term and this is very bounded with Doppler effect (hot temperature in the direction of motion of electrons, and cold temperature in the opposite direction).
At this point, we are able to write the **Boltzmann equation for photons** using the equations (1.81) and (1.83):

$$\frac{\partial \Theta}{\partial t} + \frac{\overline{p}^i}{a}\frac{\partial \Theta}{\partial x^i} + \frac{\partial \phi}{\partial t} + \frac{\overline{p}^i}{a}\frac{\partial \psi}{\partial x^i} = n_e \sigma_{Th}[\Theta_0 - \Theta + \overline{p}\cdot\overline{v}_b]. \tag{1.85}$$

In the case of small perturbation the single modes evolve independent from each others, so we define the Fourier modes:

$$\begin{aligned}\Theta(\overline{x}) &= \int \frac{d^3k}{(2\pi)^3} e^{i\overline{k}\cdot\overline{x}}\Theta(k),\\ \Theta(k) &= \int d^3x e^{-i\overline{k}\cdot\overline{x}}\Theta(\overline{x}),\end{aligned} \tag{1.86}$$

where $k \equiv \sqrt{k^i k_i}$ and it is the amplitude of wave vector, $\overline{k}$ is a wave number and p is propagation direction vector of photons. Defining the optical depth as a function of η:

$$\begin{aligned}\tau(\eta) &= \int_{\eta}^{\eta_0} d\eta' n_e \sigma_{Th} a,\\ \dot{\tau} &= -n_e \sigma_{Th} a,\end{aligned} \tag{1.87}$$

is possible rewrite the equations (1.86) passing from the coordinates space to k-space (phase space), and find the **Boltzmann equation in k-space**:

$$\dot{\Theta} + ik\mu\Theta + \dot{\phi} + ik\mu = -\dot{\tau}[\dot{\Theta}_0 - \Theta + \mu v_b]. \tag{1.88}$$

From which we can find two separate expressions for monopole and dipole:

$$\begin{aligned}\dot{\Theta}_{r,0} + k\Theta_{r,1} &= -\dot{\phi},\\ \dot{\Theta}_{r,1} - \frac{k}{3}\Theta_{r,0} &= -\frac{k}{3}\phi.\end{aligned} \tag{1.89}$$

1.7.2 Cold Dark Matter (CDM)

With the term "Cold" we are assuming that in the epoch that we are studying dark matter is not relativistic, in this way the peculiar velocities are small (opposite for the "Hot" dark matter). Dark matter has no interactions with other components except through the gravitational interaction, therefore can be considered a perfect fluid pressure-less. We can rewrite the two independent equations for monopole and dipole for the case of CDM in a k-space as:

$$\begin{aligned}\dot{\delta} + ikv + 3\dot{\phi} &= 0,\\ \dot{v} + \frac{\dot{a}}{a}v + ik\psi &= 0.\end{aligned} \tag{1.90}$$

1.7.3 Boltzmann equation for baryons

Electrons and protons are coupled by Coulomb scattering until:

$$t_{Coulomb} << t_{Hubble}. \tag{1.91}$$

At this point, it is possible make two approximations:

$$\begin{aligned} \delta_b &= \frac{\rho_e - \rho_e^0}{\rho_e^0} = \frac{\rho_p - \rho_p^0}{\rho_p^0}, \\ \overline{v}_e &= \overline{v}_p = \overline{v}_b. \end{aligned} \tag{1.92}$$

In the case of electrons we have two collisional terms due to the fact that the electrons interact with protons and photons. For photons, we have only the collisional term because the photons does not interact with protons. In this way we have two equations and is possible find a solution of them using $m_e << m_p$ working in the Fourier space. Under these assumptions we find the equation associated to the monopole (continuity equation for baryons, perturbed in a k-space) and the equation associated to the dipole (Euler equation, that describes the motion of fluid bounded to the baryons velocity and dipole associated to the radiative part):

$$\begin{aligned} &\dot{\delta}_b + ikv_b + 3\dot{\phi} = 0, \\ &\dot{v_b} + \frac{\dot{a}}{a}\overline{v}_b + ik\psi = \dot{\tau}\frac{4}{3}\frac{\rho_\gamma}{\rho_\gamma}[3i\Theta_1 + v_b]. \end{aligned} \tag{1.93}$$

The last term in the second equation gives us the contribution of Doppler effect and the dipole term Θ_1:

$$\Theta_1 \equiv i\int_{-1}^{1}\frac{d\mu}{2}\mu\Theta(\mu). \tag{1.94}$$

We can express a more general formula:

$$\Theta_l(k;\eta) \equiv (-1)^l\int_{-1}^{1}\frac{d\mu}{2}P_l(\mu)\Theta(k;\eta;\mu), \tag{1.95}$$

where $P_l(\mu)$ is a Legendre polynomial.

2

Cosmic Microwave Background radiation

Guardate le stelle e non i vostri piedi.
Provate a dare un senso a ciò che vedete,
e chiedervi perché l'universo esiste. Siate curiosi.
Stephen Hawking

The Cosmic Microwave Background radiation is the most relevant observable to investigate the properties of the early universe. As many other discoveries in human history the first detection of the most ancient radiation emitted was made by chance. In 1965, Arno Penzias and Robert Wilson, were operating at the Bell Telephone Laboratories on a radio antenna for satellite communication and, they found a temperature excess of ~ 4.2K [40, 80] isotropic and free from seasonal variations. At the same time a group in Princeton (30 km far from the Bell's laboratory) was looking for an isotropic radiation, theorized few years earlier (1946) by R.Alpher and G.Gamov as a probe of the Hot Big Bang (HBB) model [11, 50]. They confirmed that the radiation seen by Penzias and Wilson was what they were looking for. Penzias and Wilson received the 1978 Nobel Prize in Physics, see Fig.(2.1).

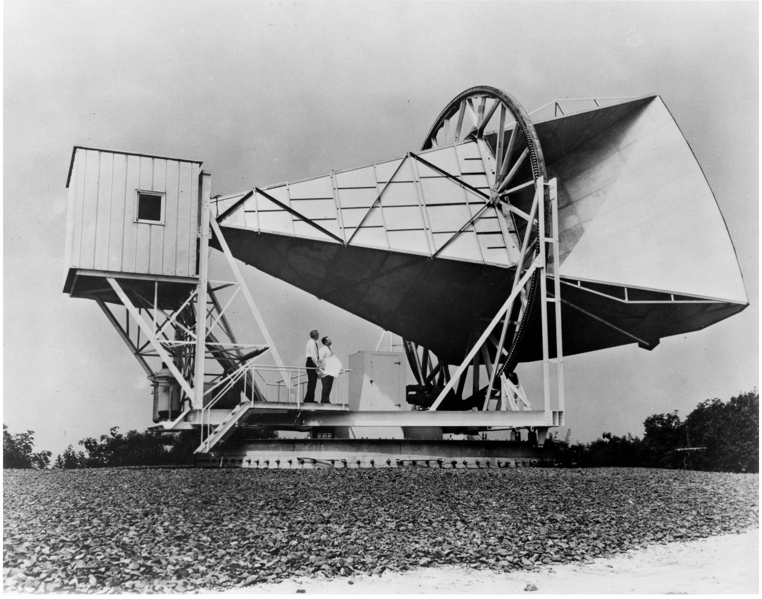

Figure 2.1: *Arno Penzias and Robert Wilson in front of the Bell's radio antenna.*

Since its discovery many experiments followed one another to study the CMB. One of the most important experiment, the first, was COBE (COsmic Background Explorer) operated in 1989-1996 [48, 49, 93]. COBE is a satellite that measured the diffuse infrared and microwave radiation from the early universe. It found that the CMB has a black-body spectrum at a temperature of $2.755K$ (see Fig. 2.2), in agreement with the theoretical predictions and also revealed spatial variations of emission. The satellite was composed by the three instruments: *DIRBE*, a multi-wavelength infrared detector used to map dust emission, *FIRAS* a spectrophotometer used to measure the spectrum of the CMB and the *DMR* a microwave instrument to map anisotropies of the CMB. The goals reached with this space mission were: a full sky map of the CMB radiation and an almost (up to 10^{-4}) perfect measurement of the associated black body spectrum:

$$B_\nu(\nu, T) = \frac{2h\nu^3}{c^2}\left(e^{h\nu/T} - 1\right)^{-1}, \tag{2.1}$$

with $T = 2.7255\text{K}$ and the presence of small temperature fluctuations of the order of:

$$\frac{\delta T}{T} \sim 10^{-5}, \tag{2.2}$$

at large angular scales.

COBE was followed by many experiments like balloons, ground-based and satellites that measured the properties of the CMB, in particular its fluctuations and their angular power spectrum.

Thanks to the results of COBE, scientists started to observe the CMB from the ground, for example: VSA (Very Small Array) [86, 89, 96, 99], DASI (Degree Angular Scale Interferometer) [52,66] and CIBI (Cosmic Background Imager) [78]. DASI found and studied the CMB temperature anisotropies and the polarization. CIBI discovered the existence of E-modes in CMB polarization.

In 2001 and, subsequently, in 2009, a new generation of satellites was lunched:

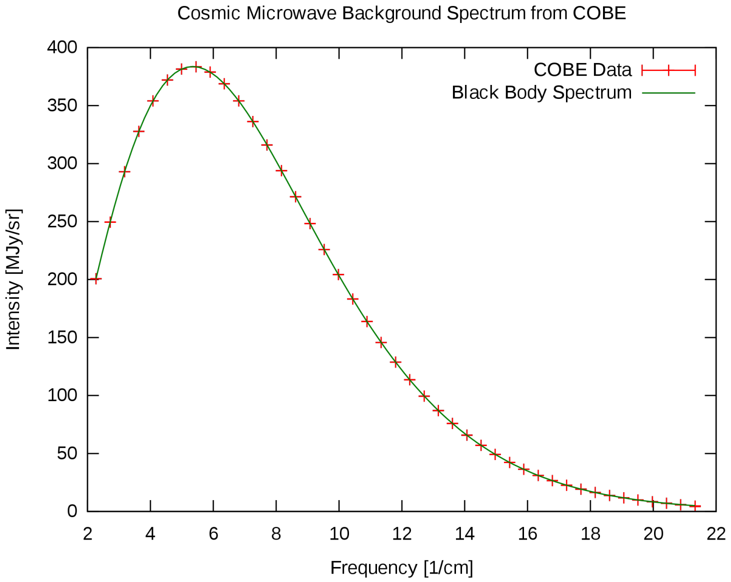

Figure 2.2: *The monopole spectrum of the Cosmic Microwave Background Radiation using the original data set by the FIRAS team [101].*

the Wilkinson microwave anisotropy probe WMAP [17,39] and Planck [10]. Both of these space missions were devoted to CMB anisotropies and to measure the cosmological parameters of the standard cosmological model. Compared to its predecessor WMAP had a 45 times higher sensitivity ($\Delta T/T \sim 10^{-6}$), and an angular resolution 33 times more precise ($15'$). Planck pushed even further the limit having a sensitivity of $\sim 2 \times 10^{-6}$ and mean angular resolution of $5'$. Sensitivity and angular resolution actually depend on the frequency band. COBE saw for the first time the CMB anisotropies, with WMAP and Planck were devoted to fully analysed anisotropies. They are the best objects that help us to study the CMB and the early stage of the universe. Removing the monopole component, in Fig.2.3 we show the CMB anisotropies and how they appear at the resolutions of the different satellite generations.

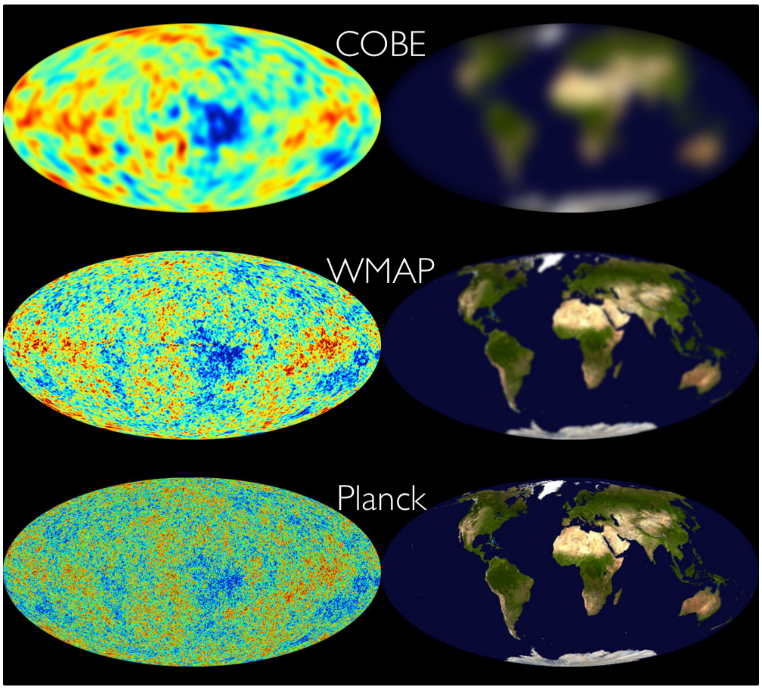

Figure 2.3: *Left-hand side: CMB as seen by COBE, WMAP and Planck, from top to bottom. Right-side: the comparison with a picture of the earth that put in evidence the increase in resolution and sensitivity.*

2.1 CMB anisotropies

There are three main physical quantities that are bound in the evolution of the universe: the gravitational potential and matter inhomogeneities that may be studied throughout the temperature anisotropies. Let us start looking at how gravitational instabilities and the evolution of the gravitational potential drive the matter inhomogeneities.

Before proceeding, we need to give a definition of dark matter, because it is the most relevant non-relativistic contribution to the total energy density of the universe. Dark matter does not interact with radiation and its evolution is coupled only with the metric perturbations. This means that it starts to fall into primordial wells well before its baryonic counterpart. At early time, during the radiation domination era its evolution depends, at most, on the radiation monopole and dipole. At later times ($z = 2750$) when matter started to dominate the evolution and the expansion history, it started to evolve with a different growing function.

In this picture the important point is the concept of gravitational instability:

if there is an initial local over-dense region, dark matter will fall into the over-density increasing the potential and attracting more matter. This means that adjacent to an over-dense region, matter is attracted by gravity and repulsed by pressure. If the attractive potential is larger than the pressure the over-density will grove with time, otherwise it will bounce until it reaches the balance. The physics that describes this last phenomenon is the harmonic oscillator.

Following the evolution of a single over-density we can define three evolution regimes: a) **super-horizon** ($k\eta \ll 1$), the over-densities being larger that the horizon size; b) **horizon-crossing** ($k\eta \sim 1$), the moment in which their size becomes of the order of the horizon size; c) **sub-horizon** ($k\eta \gg 1$) when perturbations are smaller that the horizon.

Since we have to deal with oscillations and modes it is reasonable to deal with them in frequency space where we use wave-numbers k and periods instead of size and times. The size of the over-densities (k-modes) is related to the initial conditions of the considered over-density and the horizon depends on the expansion history of the universe. Let us continue to pose our attention on the evolution of a single over-density and it is identical to look at over-densities of different size at the same moment. There are few concepts to take in mind: a) the horizon-crossing process can happen before, during or after the matter-radiation equality and this moment depends on the initial size of the perturbation. If the mode enters the horizon before the matter-radiation equality the over-density will enter in an oscillatory regime; b) the larger k wave-number are associated to smaller sizes of the perturbation and enter in the horizon earlier.

We can express the gravitational potential ϕ depending on a primordial potential ϕ^0, set during inflation, times a growth function and a transfer function [43]

$$\phi(\overrightarrow{k}, a) = \frac{9}{10}\phi^0 T(k)\frac{D(a)}{a}, \tag{2.3}$$

where $T(\overrightarrow{k})$ is the transfer function and $D(a)$ is the growth function, that describes the growth of the matter perturbations at late times. Following the idea that as time evolves, over-dense regions attract more and more matter, thereby becoming more over-dense.

It is possible to express the power spectrum of the matter distribution, during the matter era, using the Poisson equation:

$$\phi = \frac{4\pi G\rho_m a^2\delta_c}{k^2}, \tag{2.4}$$

where ρ_m is the background matter density and it is equal to:

$$\rho_m = \frac{3\Omega_m H_0^2}{8\pi a^3 G}. \tag{2.5}$$

Eq.(2.4) is the simplest expression to relate the matter over-density, δ_c,to the gravitational potential, ϕ:

$$\begin{aligned} \delta_c(\overrightarrow{k}, a) &= \frac{2ak^2}{3\Omega_m H_0^2}\phi(\overrightarrow{k}, a) \\ &= \frac{3k^2}{5\Omega_m H_0^2}\phi^0 D(a)T(k). \end{aligned} \tag{2.6}$$

In order to derive the behaviour of the potential we will divide the problem into two different regimes: large and small scales with respect to the horizon size.

2.1.1 Large Scales

For the scales which are super-horizon for very long times $k/k_{eq} \ll 1$. We again can distinguish into two regimes: scales that are super-horizon and scales which cross the horizon during the matter-dominated era.

Super-horizon - $k\eta \ll 1$

Under this assumption we can neglect k. So, the analytical solution for the potential is:

$$\phi = \frac{\phi^0}{10y^3}\left[16\sqrt{1+y} + 9y^3 + 2y^2 - 8y - 16\right], \tag{2.7}$$

where y is the ratio between a and a_{eq}. This potential goes to ϕ^0 at early times when y is small and goes to $\phi \to \frac{9}{10}\phi^0$ when the universe is matter dominated, i.e. at large y.

Crossing-horizon - $\phi = const$

Because these modes enter the horizon at very late times (after recombination), when the universe is matter dominated, the potential depends only to the matter content of the universe. Since in the initial condition we have $\dot{\phi} = 0$, the gravitational potential remains constant as long as the matter dominates the dynamics, that is up to $a \sim 1/10$, when dark energy starts to dominate.

2.1.2 Small Scales

These are scales which cross the horizon before or during the matter-radiation equality epoch $k/k_{eq} \gg 1$. We can distinguish into scales that undergo the crossing-horizon and modes that are basically always sub-horizon.

Crossing-horizon

Matter perturbations are affected by the gravitational potential, which we have seen in this regime is driven by radiation. Hence we have to consider only Θ_{r0} and Θ_{r1} contributions. The potential equation becomes:

$$\phi = \frac{6a^2H^2}{k^2}\left[\Theta_{r0} + \frac{3aH}{k}\Theta_{r1}\right], \tag{2.8}$$

where Θ_{r0} and Θ_{r1} are defined in Eqs. (1.89) and (1.90). Solving these equations we obtain the an equation that governs the potential evolution:

$$\ddot{\phi} + \frac{4}{\tau}\dot{\phi} + \frac{k^2}{3}\phi = 0, \tag{2.9}$$

whose solution is:

$$\phi = 3\phi^0\left[\frac{\sin(k\tau/\sqrt{3}) - (k\tau/\sqrt{3})\cos(k\tau/\sqrt{3})}{(k\tau/\sqrt{3})^3}\right]. \tag{2.10}$$

This means that as soon as the mode enters the horizon, the potential drops down and starts to oscillate. Once we know the behaviour of the potential it is possible to find the evolution of the matter perturbation, δ_c, that is:

$$\ddot{\delta}_c + \frac{1}{\tau}\dot{\delta}_c = -3\ddot{\phi} + k^2\phi - \frac{3}{\tau}\dot{\phi}, \tag{2.11}$$

where the right-hand part of the equation represents the source term for the dark matter perturbations. Eq.(2.11) has two solutions $\delta = 0$ and $\delta = \ln(a)$, which leads to a logarithmic growth of the dark matter perturbations. In general it is possible to build a general solution using the source term weighted by a Green's function, however results are comparable to the approximate solution and show that matter perturbations grow also in the radiation dominated epoch, but the growth is smaller than in the matter-dominated era due to the presence of the radiation pressure.

Sub-horizon

Radiation pressure induces the decay of gravitational potential. However it could happen that $\rho_c\delta_c$ becomes larger that $\rho_r\Theta_r$, even if the radiation dominates the energetic content of the universe. This is exactly what happened in the sub-horizon modes, therefore in this case we can neglect the radiation contribution and find the equation that governs the evolution of sub-horizon dark matter perturbations, the so called "**Meszaros equation**" [43]:

$$\delta_c'' + \frac{2+3y}{2y(y+1)}\delta_c' - \frac{3}{2y(y+1)}\delta_c = 0. \tag{2.12}$$

The general solution of this equation is:

$$\delta_c = C_1 D(y) + C_2 D_2(y), \tag{2.13}$$

where $D(y) = y+2/3$ and $D_2(y) = D(y)\ln[(\sqrt{1+y}+1)/(\sqrt{1+y}-1)] - 2\sqrt{1+y}$. From the latter, at early times ($y \ll 1$), the radiation contribution to the energy density drives the universe to expand so fast that matter has no time to follow it. The consequence is that δ_c is fixed to a constant value, which means that matter perturbations don't grow. Otherwise, at late times ($y \gg 1$), when the radiation contribution becomes negligible and the universe is dominated by matter, dark matter perturbations grow as $\delta_c \propto a$. In this picture, when matter perturbations enter the horizon having $\dot{\delta}_c > 0$, they are not frozen and continue to grow giving a total boost factor proportional to $\ln y$.

2.2 CMB anisotropies in temperature

As we have seen in the last section of the previous chapter, when hydrogen recombines, photons start to free stream in a neutral universe. These photons carry on the information about the early universe imprinted in their energy and angular distribution by years of thermalisation. On the average temperature of the CMB there are temperature fluctuations. Since the theory is only able to give predictions about the stochastic properties of the CMB fluctuations, we focus our attention on the statistical properties of the temperature anisotropies. Inflation predicts that the initial perturbations are Gaussian distributed, and, if the evolution is linear, the Gaussianity is conserved in time. All the statistical information about the anisotropy field is contained in the two-point correlation function:

$$C(\theta) = \left\langle \frac{\delta T}{T}(\widehat{n}) \frac{\delta T}{T}(\widehat{n}') \right\rangle, \tag{2.14}$$

where $\theta = \widehat{n} \cdot \widehat{n}'$.

The temperature anisotropies are studied expanding the anisotropies in spherical harmonics:

$$\frac{\Delta T}{T}(\theta, \phi) = \sum_{\ell=0}^{\infty} \sum_{m=-\ell}^{\ell} a_{\ell m} Y_{\ell m}(\theta, \phi). \tag{2.15}$$

The coefficients $a_{\ell m}$ are obtained by the orthonormal propriety of the spherical harmonics:

$$a_{\ell m} = \int \frac{\Delta T}{T}(\widehat{n}) Y^*_{\ell m}(\theta, \phi) d\Omega. \tag{2.16}$$

Under this assumption the $a_{\ell m}$ coefficients follow the normal distribution with zero mean and non-zero variance.

We can rewrite Eq.(2.14) in harmonic space:

$$C(\theta) = \sum_{\ell=0}^{\infty} \frac{2\ell+1}{4\pi} C_\ell P_\ell(\theta), \tag{2.17}$$

where $P_\ell(\theta)$ are the Legendre polynomials and C_ℓ are:

$$C_\ell = \langle a_{\ell m} a^*_{\ell m} \rangle = \frac{1}{4\pi} \int d\Omega d\Omega' P_\ell(\widehat{n} \cdot \widehat{n}') \left\langle \frac{\delta T}{T}(\widehat{n}) \frac{\delta T}{T}(\widehat{n}') \right\rangle. \tag{2.18}$$

The C_ℓ's represents the variance of fluctuations at a given angular scale where in first approximation:

$$\theta \sim \frac{\pi}{\ell}. \tag{2.19}$$

Moreover, C_ℓ's coefficients are the angular power spectrum of temperature fluctuations. The angular power spectrum is usually plotted using the combination:

$$D_\ell = \frac{\ell(\ell+1)}{2\pi} C_\ell. \tag{2.20}$$

In Fig.2.4 we show the temperature angular power spectrum as measured by Planck [10]. The uncertainties of the TT spectrum are dominated by variance, rather than by noise or foreground residuals, at all scales below $\ell = 1800$. The particular shape of the angular power spectrum is the main source of cosmological information. Its shape is predicted by the standard cosmological model and it is composed by primary and secondary contributions.

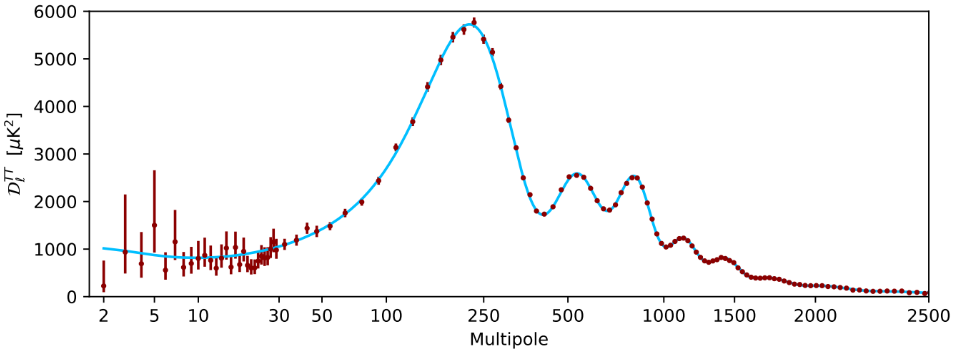

Figure 2.4: *Angular power spectrum of CMB in temperature. Blue line corresponds to the theoretical trend, red dots are Planck 2018 mesurements [10].*

2.2.1 *Primary anisotropies*

The inflation, as we shown in Chapter 1, stretched all the primordial perturbations on scales larger than the Hubble radius and they remained frozen until the universe expanded up to their sizes. It is possible distinguish between:

- **Gravitational perturbations**. The gravitational perturbations produce the dominant large-scale effect arising from gravitational potential perturbations ϕ at last scattering that cause a change in frequency of the CMB photons. The effect of this kind of perturbations gives a temperature fluctuation:
$$\frac{\delta T}{T} = \frac{1}{3}\delta\phi. \tag{2.21}$$
This relation take in account two contribution: photons that climb out of a potential well generated by an over-density region cools the back-ground and while they are climbing out, the universe expands itself slower compared to the surrounding regions because of the over-density.

- **Density perturbations**. The density perturbation are wells/hills of potentials where the photon-baryon fluid falls/slips, in general the denser the fluid the higher the temperature.

- **Velocity perturbations**. The velocity perturbations are photons that have a greater momentum and smaller mean free path and the other way around.

Looking to Fig.2.4 we can do some consideration about: low ($2 \leqslant \ell \leqslant 50$), intermediate ($50 \leqslant \ell \leqslant 1500$) and high multipoles ($\ell > 1500$).

Super-horizon scales

The region of small multipoles, where ℓ is between 2 and 50, is characterized by a plateau. These scales are super-horizon scales and are independent on the physics of the fluid component. At these scales fluctuations reflects the distribution of DM and thus the gravitational potential. The effect that affect the photons is the so called **Sachs-Wolfe effect**:

$$\left(\frac{\delta T}{T}\right)_{S-W} = \frac{1}{3}\delta\phi. \tag{2.22}$$

This equation shows that large-scales regions of higher density will appear as colder in the CMB map and the other way around.
Photons passing through large-scale gravitational wells (or hills) experience a gravitational redshift losing (or increasing) their energy.

Acoustic peaks

The APS is the statistical point of view of the anisotropies on the LSS, at that epoch the universe was mainly composed by hydrogen, helium, photons, neutrinos and dark matter. Photons and baryons have been tightly coupled until the decoupling. Inhomogeneities feel their own gravity and collapse if they enter the horizon until the radiation pressure dominates the equation and they start to oscillate. Therefore, the **first peak** have exact correspondence with the sound horizon at the recombination time.
Fluctuations larger than the first peak are super-horizon, while fluctuations on smaller scales are sub-horizon. This implies that they follow the oscillatory behaviour driven by gravity and pressure.
The **series of small peaks** are the results of an oscillatory processes: modes that were frozen by the recombination at the maximum of compression (or rarefaction) are mapped into the peaks, while those that are exactly in phase with the background are mapped into the wells. The first peak represents a mode that has completed one compression, the second peak, represents a mode that has half the wavelength, has complete one compression and one rarefaction, and so on.

2.2.2 Sub-horizon scales

For high multipoles, more precisely $\ell > 1500$ the APS starts to be dominated by the **damping effect**. If we think the LSS as a non instantaneous process, i.e. we consider a last-scattering layer instead of a last-scattering surface, all the temperature fluctuations on scales that are smaller than the thickness of the layer, which depends on the mean-free path of photons, will be exponentially damped.

2.2.3 Secondary anisotropies

The secondary anisotropies are not directly connected to the primary, their existence is due to effects that happens well after the LSS. In this section we discuss the principal secondary anisotropies:

- Integrated Sachs-Wolfe effect;
- CMB lensing;
- Re-ionization;
- Sunyaev-Zeldovich effect.

Integrated Sachs-Wolfe effect

Photons during their journey from the LSS to us travel in gravitational potentials that are not constant in time. This is an important effect for potentials on large scale: these potentials change over cosmological time-scales because of the expansion of the universe. The gravitational potentials evolve during the time needed to a photon to travel through them, thus, the blueshift, experienced by photons falling in the potential is not balanced by the redshift when they come out.

The total sum of gravitational effects depends on the time variation of the gravitational potential and is called **Integrated Sachs-Wolfe** (ISW) effect:

$$\frac{\delta T}{T} = \int \dot{\phi}[r(t), T]dt, \tag{2.23}$$

where $\dot{\phi} = \frac{d\phi}{d\tau}$ and $d\tau = dt/a(t)$.

After recombination the universe is not completely dominated by matter and the radiation gives a significant contribution to the fluctuations potential of DM. The diffusion of the photons by Thomson scattering causes $\frac{\delta T}{T} < 0$ called **Early**

ISW. Another effect is the so called **Late ISW** that happens at $z << z_{rec}$ and therefore affects large angular scales. It is related to the nature of the dark energy.

CMB lensing

The propagation of a photon in the universe is deflected by the mass distribution along its path. Weak gravitational lensing produced by distortions due to non uniform distribution of mass, for example: galaxies or cluster of galaxies, leads to change in photon direction. This impacts mainly at small and intermediate angular scales peaking at $\ell = 1000$.

Re-ionization

After the decoupling, CMB photons encounter again a distribution of free electrons, probably re-ionized by UV photons produced by the first stars. Inside the ΛCDM model this effect is parametrized as a re-ionization layer that reduces the fluctuation amplitude on all scales by a factor $e^{-\tau_{rei}}$, where τ_{rei} is the **re-ionization optical depth**:

$$\tau_{rei} = \int n_e \sigma_T d\ell. \tag{2.24}$$

Here, n_e is the free electron number density and σ_T is the Thompson cross-section. The effect of the re-ionization is shown in Fig. 2.5.

Sunyaev-Zeldovich effect

CMB photons are scattered by high energy electrons in intracluster gas. Electrons transfer energy to CMB photons through inverse Compoton processes and simultaneously change their direction of propagation. We can define two different type of this effect:

- **thermal SZ effect**: due to the high temperature of free electrons it distorts the CMB spectrum giving energy to the photons. The black body spectrum shifts to higher energies and it looks like a reduction in temperature of the photons at low frequencies.
- **kinetic SZ effect**: it is due to the peculiar velocity of the cluster. The Thompson scattering of CMB photons with the free electrons in the cluster produce a Doppler effect.

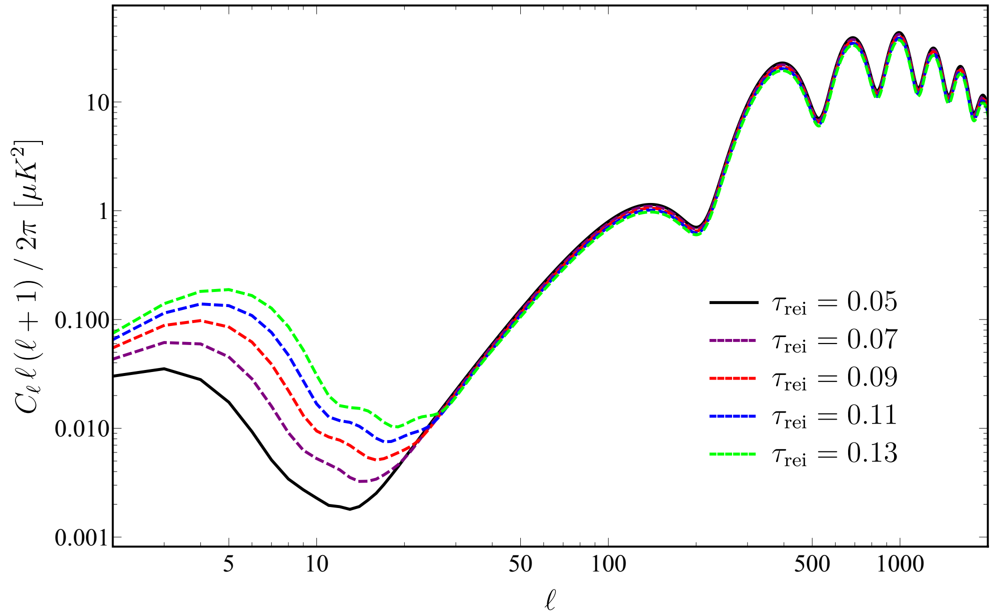

Figure 2.5: *CMB angular power spectrum for different value of* τ_{rei}*: 0.05 (black line), 0.07 (purple dashed line), 0.09 (red dashed line), 0.11 (blue dashed line) and 0.13 (green dashed line).*

2.3 Effects on power spectrum

It is possible calculate the power spectrum of the CMB considering a model of the universe and following it in the evolution of the distribution function of photons. If Ω_0 decreases we have that the angular scale corresponding to a given physical scale decreases and shifts towards larger ℓ. In the case of $\Omega_b = 0$, we do not have acoustic peaks, but only the first one, which is due to dark matter falling into primordial gaussian field perturbations would survive. Increase the value of Ω_b means increase the effective mass perturbation and consequently increase the amplitude if the odd peaks and decrease the power of the even peaks of the spectrum. If H_0 decreases, the distance to LSS increases, the angle subtended decreases and moves to larger ℓ.

2.4 CMB polarization

In the previous sections we have described the temperature fluctuations of the CMB, however Thompson scattering provides also a soft polarization of the

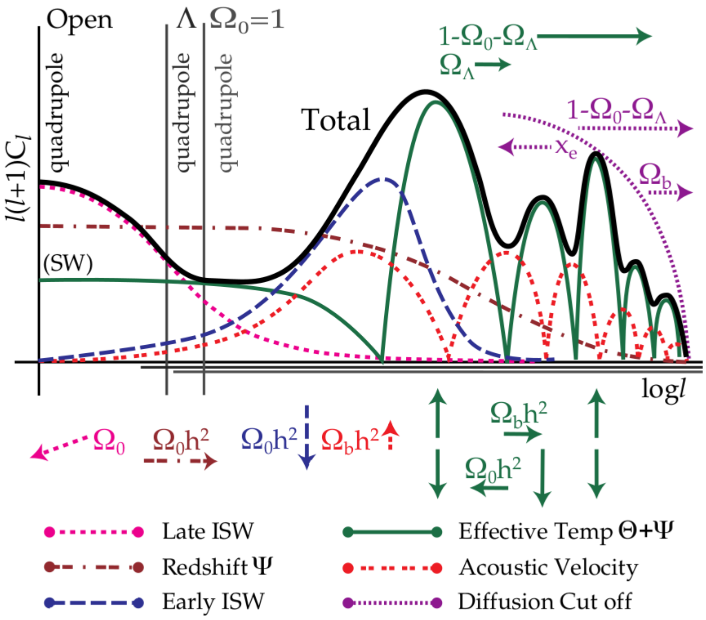

Figure 2.6: *Total spectrum of the CMB anisotropy in which we highlighted the different effects on the spectrum by playing with the cosmological parameters. [56]*

radiation [29].

We consider a monochromatic wave that propagates in the direction $\widehat{x}$. In the primordial universe, before decoupling we have:

$$\begin{aligned} E_x(t) &= a_x(t)cos(\omega_0 t - \theta_x(t)), \\ E_y(t) &= a_y(t)cos(\omega_0 t - \theta_y(t)), \end{aligned} \tag{2.25}$$

where ω_0 is the pulse of the monochromatic wave that propagates in the direction $\widehat{x}$.

It is useful introduce the **Stokes parameters** I for the intensity, Q and U for linear polarization and V for circular polarization:

$$\begin{aligned} I &=< a_x^2 > + < a_y^2 >, \\ Q &=< a_x^2 > - < a_y^2 >, \\ U &=< 2a_xa_y\cos(\xi_x - \xi_y) >, \\ V &=< 2a_xa_y\sin(\xi_x - \xi_y) >, \end{aligned} \tag{2.26}$$

where < ... > indicates the time average.

The parameter I represents the intensity of the wave, the Q parameter quantifies

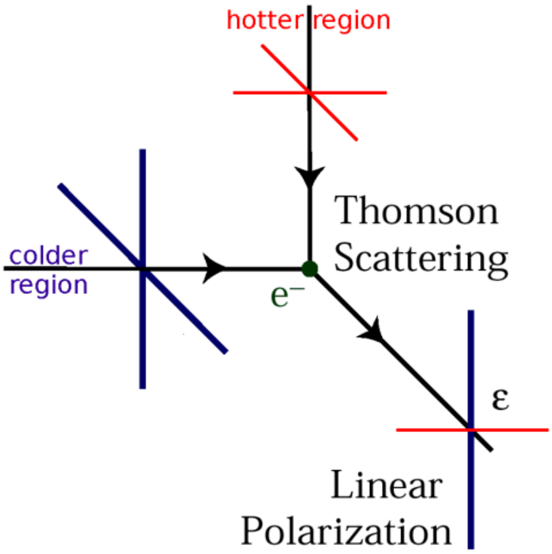

Figure 2.7: *Thompson scattering of radiation with quadrupole anisotropy generates linear polarization. In the rest frame of the electron, red lines represent hotter radiation, while blue lines represent colder radiation resulting in a quadrupole anisotropy of the incident radiation [73].*

the polarization along the x-y directions, U quantifies the polarization along axes rotated by 45° and the V Stokes parameter is expected to vanish as Thompson scattering induces no circular polarization.
We can consider the transformation property of Stokes parameters under rotation of the axis x and y by an angle θ. While I and V are scalars, Q and U become:

$$\begin{aligned} Q' &= Q\cos(2\theta) + U\sin(2\theta)\ , \\ U' &= -Q\sin(2\theta) + U\cos(2\theta)\ . \end{aligned} \tag{2.27}$$

We can also define a **polarization vector**:

$$P = Q + U, \tag{2.28}$$

where P has the amplitude $\sqrt{Q^2+U^2}$ and form with respect to the x axis an angle $\alpha = \frac{1}{2}\tan^{-1}\frac{U}{Q}$. Polarization vector is positive defined.
With these transformation properties we can introduce the **polarization matrix**:

$$P = \frac{1}{2}(\sigma_0 I + \sigma_x Q + \sigma_y U + \sigma_z V) = \frac{1}{2}\begin{pmatrix} I-Q & U-iV \\ U+iV & I+Q \end{pmatrix} \tag{2.29}$$

with $\sigma_\mu \equiv (1, \sigma_i)$ where σ_i are the Pauli matrices.

2.4.1 Production mechanism of polarization

We know very well that the fundamental process in which radiation interacts with matter is the Thompson scattering. The interaction between photons and matter is not sufficient for the production of CMB polarization, because the process is symmetric, i.e. does not prefer a particular direction. The Thompson cross section is:

$$\frac{d\sigma}{d\Omega} = \frac{3}{8}\frac{\sigma_{Th}}{\pi}|\widehat{\epsilon'} \cdot \widehat{\epsilon}|^2 \ , \tag{2.30}$$

where $\widehat{\epsilon'}$ is the incident wave and $\widehat{\epsilon}$ is the wave diffused by the electron. Impose that z axis is the direction of the photon emitted, we can define the intensity of the incident (I') and diffused (I) light and suppose that the incident light is un-polarized:

$$\begin{aligned} I_x &= \frac{3\sigma_{Th}}{8\pi} I' \ , \\ I_y &= \frac{3\sigma_{Th}}{8\pi} I' cos^2(\theta) \ , \end{aligned} \tag{2.31}$$

where $I_x = (I + Q)/2$, $I_y = (I - Q)/2$ and $I'_x = I'_y = I/2$. So we ca rewrite I and Q:

$$\begin{aligned} I = I_x + I_y &= \frac{3\sigma_{Th}}{8\pi} I'(1 + cos^2\theta) \ , \\ Q = I_x - I_y &= \frac{3\sigma_{Th}}{8\pi} I' sin^2\theta \ . \end{aligned} \tag{2.32}$$

Now the total Stokes parameters for scattered radiation expanding in spherical harmonics become:

$$\begin{aligned} I &= \frac{3\sigma_{Th}}{16\pi}\left[\frac{8}{3}\sqrt{\pi}a_{00} + \frac{4}{3}\sqrt{\frac{\pi}{5}}a_{20}\right] , \\ Q &= \frac{3\sigma_{Th}}{4\pi}\sqrt{\frac{2\pi}{15}}Re(a_{22}), \\ U &= -\frac{3\sigma_{Th}}{4\pi}\sqrt{\frac{2\pi}{15}}Im(a_{22}). \end{aligned} \tag{2.33}$$

The production of polarization is related to the presence of a quadrupole term in the intensity of radiation (a_{22}).

If the incident radiation from perpendicular directions (separated by 90°) had different intensities, like in Fig.2.7, a net linear polarization would result. Such anisotropy is called **quadrupole** because the poles of anisotropy are 90° apart. The sources of quadrupole anisotropy are: a) scalar perturbations, due to the velocity gradient of the photons in the plasma density fluctuations. At the recombination, photons are flowing from the cold under-densities to the hot over-densities. This mechanism generates a gradient in the velocity distribution of the photons and so a scalar quadrupole anisotropy. b) tensor perturbations, that, at the recombination, are generated by residual gravitational waves generated during the inflation. This tensor effect has been predicted by the inflationary theory, but it has still not been detected, consequently the predictions about its amplitude and its contribution to the linear polarization signal depend on the considered model. The amplitude of tensor perturbations is usually related to the intensity of the scalar perturbations through the so called tensor-to-scalar ratio, r.

2.4.2 E and B-modes

The common approach followed in CMB analysis is to consider two combinations for the polarization components $Q \pm iU$. The associated transformation law for rotation is:

$$(Q \pm iU)' = e^{\pm 2i\phi}(Q \pm iU). \tag{2.34}$$

Expanding the linear combination of Q and U in spherical harmonics we have:

$$Q(\widehat{n}) + iU(\widehat{n}) = \sum_{\ell=0}^{\infty} \sum_{m=-\ell}^{\ell} a_{2,\ell m}\, Y^{2}_{\ell m}(\widehat{n}), \tag{2.35}$$

$$Q(\widehat{n}) - iU(\widehat{n}) = \sum_{\ell=0}^{\infty} \sum_{m=-\ell}^{\ell} a_{-2,\ell m}\, Y^{-2}_{\ell m}(\widehat{n}). \tag{2.36}$$

Using some properties of spin-2 harmonics coefficients it is possible to write the polarization field in the most common representation used in cosmology:

$$\begin{aligned} a_{E,\ell m} &= -\frac{a_{2,\ell m} + a_{-2,\ell m}}{2}, \\ a_{B,\ell m} &= i\frac{a_{2,\ell m} + a_{-2,\ell m}}{2}. \end{aligned} \tag{2.37}$$

From that we can define:

$$\begin{aligned} E(\widehat{n}) &= \sum_{\ell m} a_{E,\ell m} Y_m^\ell(\widehat{n}), \\ B(\widehat{n}) &= \sum_{\ell m} a_{B,\ell m} Y_m^\ell(\widehat{n}), \end{aligned} \tag{2.38}$$

these are two scalar quantities that describe the polarization. $T(\widehat{n})$, $E(\widehat{n})$ and $B(\widehat{n})$ are invariant under rotations and under parity transformation.
E-modes have $(-1)^\ell$ parity on the sphere and **B-modes** have $(-1)^{\ell+1}$ parity. Considering the transformation $\widehat{n} \rightarrow -\widehat{n}$ E-modes remain unchanged for even value of ℓ, while B-modes change the sign (an example is shown in Fig. 2.8 for the particular case of $\ell = 2, m = 2$). Using a useful analogy with electromagnetic fields, $E(\widehat{n})$ and $B(\widehat{n})$ represent the decomposition of polarization field in a part with zero divergence and zero rotor respectively for B and E.

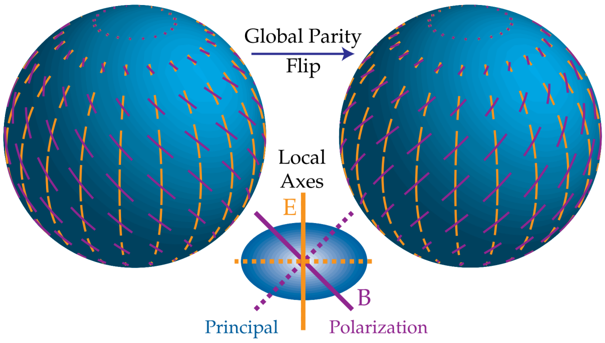

Figure 2.8: *Polarization pattern for $\ell = 2, m = 2$. In this figure is shown the generation of opposed patterns for E-modes (thick lines) and B-modes (thin lines), from a scattering of a tensor m=2 perturbation.*

Starting from eq.(2.38) and eq.(2.15) using the eq.(2.15) we can write all the combinations of $T(\widehat{n})$, $E(\widehat{n})$ and $B(\widehat{n})$ spectra:

$$\begin{aligned}
C_\ell^{TT} &= \frac{1}{2\ell+1}\sum_{m=-\ell}^{\ell}(a_{\ell m}^* a_{\ell m}),\\
C_\ell^{EE} &= \frac{1}{2\ell+1}\sum_{m=-\ell}^{\ell}(a_{E,\ell m}^* a_{E,\ell m}),\\
C_\ell^{BB} &= \frac{1}{2\ell+1}\sum_{m=-\ell}^{\ell}(a_{B,\ell m}^* a_{B,\ell m}),\\
C_\ell^{TE} &= \frac{1}{2\ell+1}\sum_{m=-\ell}^{\ell}(a_{\ell m}^* a_{E,\ell m}),\\
C_\ell^{EB} &= C_\ell^{TB} = 0.
\end{aligned} \tag{2.39}$$

In Fig. 2.9 and Fig. 2.10 we show the public TE and EE power spectra measured by the Planck collaboration [10]. As already noticed for the TT power spectrum in the previous section, the observed data (red dots) are in very good agreement with the theoretical prediction of the standard cosmological model (blue line).

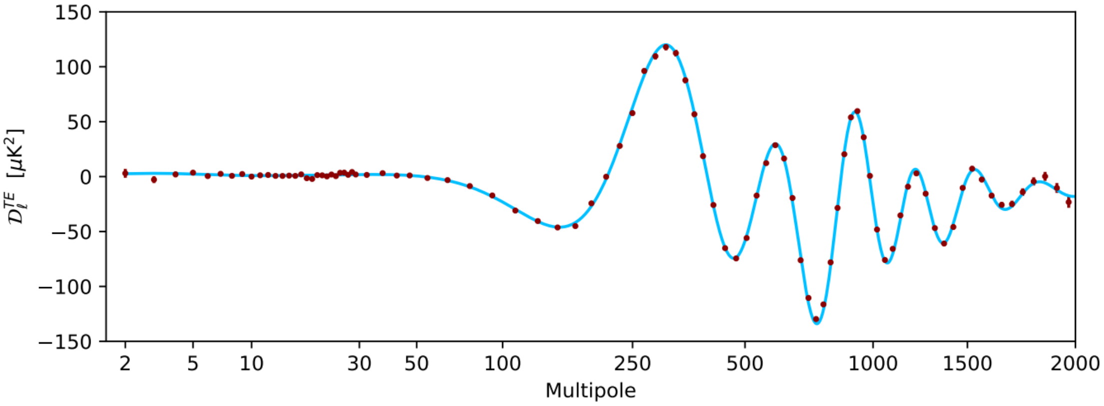

Figure 2.9: *TE angular power spectra of the CMB anisotropies measured by the Planck satellite. Blue line correspond to the best fit of theoretical model (ΛCDM) based on six standard parameters, while red points are the binned value of D_ℓ with the corresponding error bars [10]*

If we consider the transformation properties under parity of the E and B modes we obtain:

$$\begin{aligned}
E'(\widehat{n}') &= E(\widehat{n})\\
B'(\widehat{n}') &= -B(\widehat{n})
\end{aligned} \tag{2.40}$$

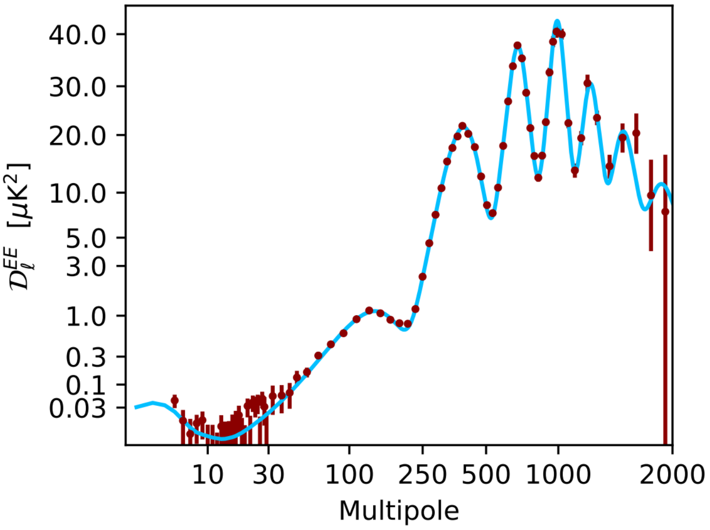

Figure 2.10: *EE angular power spectra of the CMB temperature anisotropies measured by the Planck satellite. Blue lines correspond to the best fit of theoretical model (ΛCDM) based on six standard parameters, while red points are the binned value of D_ℓ with the corresponding error bars [10]*

from which it results that E is actually a scalar, while B is a pseudoscalar. For parity conservation therefore the cross correlation between C_ℓ^{EB} and C_ℓ^{TB} is zero. Calculating all the possible two-point correlation functions, we obtain a 3x3 symmetric spectra matrix :

$$\begin{pmatrix} C_{TT\ell} & C_{TE\ell} & C_{TB\ell} \\ C_{ET\ell} & C_{EE\ell} & C_{EB\ell} \\ C_{BT\ell} & C_{BE\ell} & C_{BB\ell} \end{pmatrix} \tag{2.41}$$

where each element is given by:

$$< X(\widehat{n}_1)(\widehat{n}_2) >= C_{XY} \cos\theta_{12} = \sum_\ell C_{XY\ell} P_\ell \cos\theta_{12}, \tag{2.42}$$

with X,Y = T,E,B.

The introduction of the E (scalar) and B (pseudo-scalar) modes is due to the physical origins of the effects that generate the linearly polarized signal. E-modes are generated both by scalar and tensor perturbations, while B-modes arise only from tensor perturbations.

2.5 Observing the CMB

CMB is a diffuse emission in the microwaves. It is very weak with respect to radiation produced at the same wavelengths by our living environment and by the instruments used to measure it: telescope, optical system and detectors. During the observation we are affected by contaminations (instrument uncertainties) and a stochastic uncertainties (cosmic variance).

2.5.1 Cosmic variance

Cosmic variance is an intrinsic limit to the precision of the evaluation of the power spectrum due to the stochastic nature of CMB analysis since we are observing only one CMB sky. As we observe large scales, the number of points that are correlated decreases, thus the smaller is the number of points available the greater is the statistical uncertainty which we have to deal with.
Inflation predicts that the coefficients of the harmonic expansion are very close to Gaussian variables. We can define an estimator for the power spectrum:

$$\widehat{C}_\ell \equiv \frac{1}{2\ell+1}\sum_{m=-\ell}^{\ell}|\widehat{a}_{\ell m}|^2 = \frac{C_\ell}{2\ell+1}V, \tag{2.43}$$

where V is:

$$V \equiv \sum_{m=-\ell}^{\ell}\frac{|\widehat{a}_{\ell m}|^2}{C_\ell}. \tag{2.44}$$

The variable V is a sum of $2\ell+1$ squared Gaussian variables with unit variance and its probability distribution function is a chi-square with $2\ell+1$ degrees of freedom ($P_{\chi^2_\ell}$). We can write the probability distribution function for the estimator $\widehat{C}_\ell$ as:

$$P(\widehat{C}_\ell) = \frac{\ell}{C_\ell}P_{\chi^2_\ell}\left(\frac{\ell\widehat{C}_\ell}{C_\ell}\right). \tag{2.45}$$

This equation shows that our estimator is distributed according to a chi-square probability distribution function. For $\ell \to \infty$ the Central Limit Theorem guarantees that the distribution will become Gaussian, hence:

$$<\widehat{C}_\ell>= C_\ell, \tag{2.46}$$

and its variance becomes:

$$< \widehat{C}_\ell^2 > - < \widehat{C}_\ell >^2 = \frac{2}{2\ell+1} C_\ell. \tag{2.47}$$

We conclude that the fact that there are only $2\ell + 1$ independent directions on the sky for a given multipole ℓ, limits the efficiency of our estimator for the power spectrum with the so called **cosmic variance**:

$$\frac{< \widehat{C}_\ell^2 > - < \widehat{C}_\ell >^2}{C_\ell} = \frac{2}{2\ell+1}. \tag{2.48}$$

The cosmic variance mostly affects the large scales and it is sub-dominant for $\ell > 1000$, see Fig.2.11.

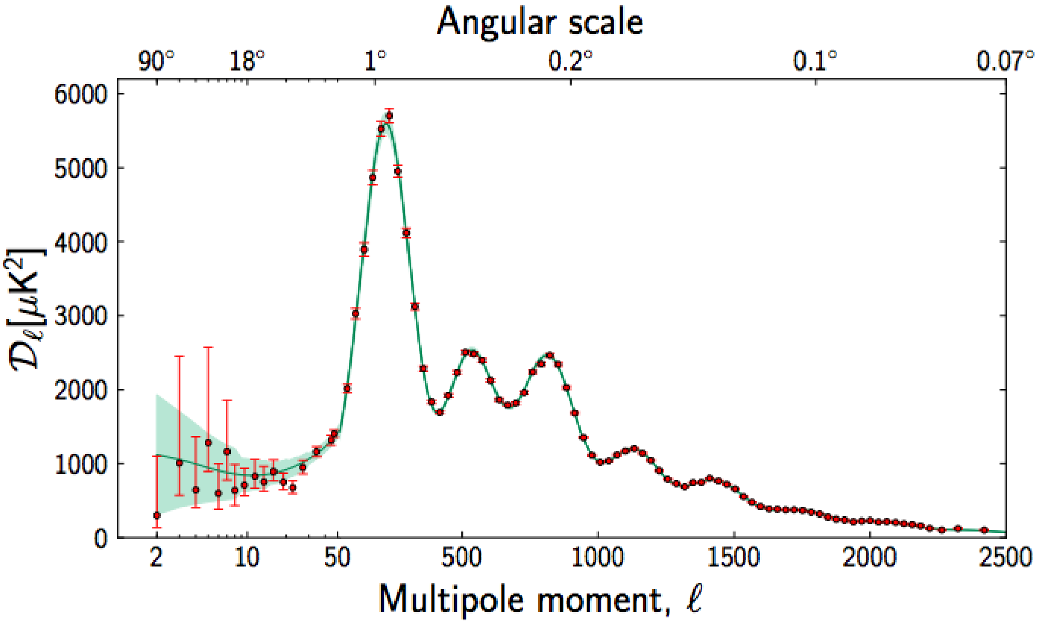

Figure 2.11: *Angular power spectrum measured by Planck. The blue line is the theoretical trend and the red dots are the observed data and their errors. The blue shaped region is the cosmic variance [2].*

2.5.2 Instrumental effects

The instrumental systematics are originated by different sources and affects in a different way different scales [2, 6, 7]: the detector intrinsic precision, pointing issues, calibrations, noise uncertainties.

The impact of the instrumental effects on each detector depends on the value of the coupling coefficient for each detector. These coupling coefficients tell us how much the physical temperature fluctuations impact each detector reading. They depend on the emissivity properties of the object and on the optical and geometrical properties of the set-up. The level of the noise depends on the total integration time per sky pixel, which is unlikely to be evenly distributed for realistic observing strategies. Moreover the white noise part of the detector spectrum becomes dominated by a steeper component. This extra power at long wavelength will translate in "stripping" of the noise maps.

2.6 Foregrounds

For present and future CMB experiments the identification and separation of signals coming from different sources is an important step in data analysis.
The main goal of **component separation** is to provide a map of the CMB, from which the relevant cosmological information will be derived, cleaned from foreground contamination [14, 22, 24, 38, 55, 97]. In order to have success a CMB experiment must take into account and properly remove (if possible) a number of non CMB signals and effects [59]. Figure 2.12 are shown, as a function of frequency, the intensity of the synchrotron, free-free, dust and CO lines emission in relation to the CMB, that are the main foreground emission that we need to take in account during the component separation problem.

2.6.1 Synchrotron

Synchrotron radiation is due to relativistic cosmic ray electrons which are accelerated by the Galactic magnetic field [87]. The emission depends on the grown density and energy spectrum of the electrons and the strength of the magnetic field. The 75% of this radiation is highly polarized perpendicularly to the field lines. An accurate modelling of the magnetic field distributions and the galactic cosmic ray can (in principle) be used to predict the polarization foreground from synchrotron emission and remove it from observed maps. At frequencies above a few 100 MHz, the spectrum is optically thin and is steeply falling with frequency, with typical temperature spectral indices ($T \propto \nu^{\beta}$) of $\beta \sim -2.7$ at GHz frequencies. The values are obtained by phenomenologically constraining the synchrotron associated power law. At higher frequencies, the

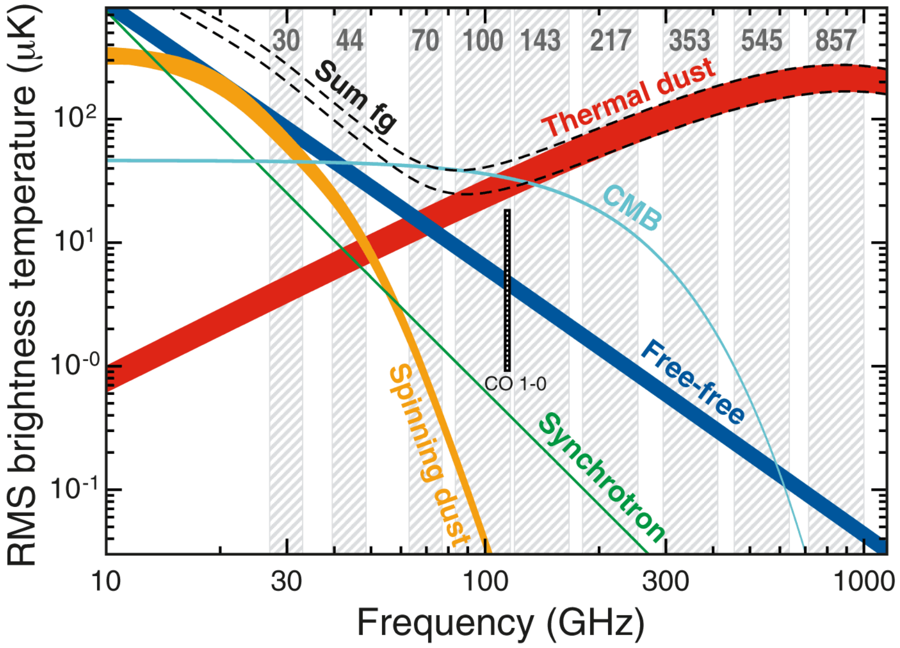

Figure 2.12: *Most recent determinations of the rms anisotropy as a function of frequency for CMB and for sources of foreground emission: synchrotron, free-free, spinning dust, and thermal dust emission in temperature. [1]*

spectrum appears to steepen further, presumably due to radiative losses, which cause spectral ageing, with $\beta \sim -3.0$ [32, 41]. Synchrotron radiation is present in both temperature and polarization maps.

The polarization of synchrotron radiation is less known, since it can only be directly mapped at frequencies above a few GHz, due to the effect of Faraday Rotation, which is important at frequencies below a few GHz.

2.6.2 Free-Free emission

Free-free (Bremsstrahlung) emission is generaed by free electrons interacting with ions in ionised gas. These electrons are accelerated by protons and emit free-free radiation. Close to the gaactic plane it is the dominant foreground at frequencies $\nu > 1$ GHz and it is well described by a power law, althought at lower frequencies presents a visible break. This is due to the fact that the medium becomes optically thick and the brightness an the electron temperature become equal. At frequencies above a few GHz, the emission is optically thin and consequently we have a flatter spectral index of $\beta \approx 2.1$ [41]. Comparing the free-free spectrum with the synchrotron one, at low frequencies they are very similar, but they can be distinguished because the power-law index of free-free is flatter than the synchrotron one. Bremsstrahlung emission is intrinsically unpolarized. In fact, the Coulomb interactions have random orientation, with no significant alignment with the magnetic field. Residual polarization can occur on sharp edges due to Thomson scattering [41].

2.6.3 Thermal and spinning dust radiation

We can distinguish between thermal and spinning dust emission. The thermal dust emission is black-body emission modified by opacity effects, from interstellar dust grains with typical temperatures around 20 K and $\beta \sim 1.5 - 2$ [46]. This emission can be significantly polarized, because elongated dust grains emit along their shortest axes, while large dust grains can align efficiently by the galactic magnetic field. The dust having non-zero dipole moment rotates and emits in the microwave region of the electromagnetic spectrum. The spinning dust radiation is emitted by the smallest ($\sim 10^{-9} m$) interstellar dust grains and molecules, which can rotate at few GHz. If they have an electric dipole moment, they emit by electric dipole radiation [44].

2.6.4 CO lines

CO lines are carbon monoxide transition lines that Planck experiment detected, in particular at the frequencies of 100, 217 and 353 GHz. It is possible to separate these lines from the other diffuse components and to describe parametrically in terms of an amplitude inside the corresponding detector map.

2.6.5 Extragalactic point sources

Radio sources relevant in the microwaves are the so called "blazars". These are jet-dominated extragalactic objects characterized by a strongly variable and polarized emission of non-thermal radiation, from low radio energies up to high energy gamma rays.

2.6.6 Cosmic Infrared Background

The Cosmic Infrared Background (CIB) is a background emission of the formation and evolution of the galaxies at wavelengths larger than few microns. The infrared emission collects contributions from different populations at different redshifts. CIB is important because it is expected to probe the clustering properties of galaxies, that are linked to the dark matter halos distribution. The APS of CIB anisotropies has two contributions: white-noise component and an additional component, caused by shot noise and by spatial correlations between the sources of the CIB respectively.

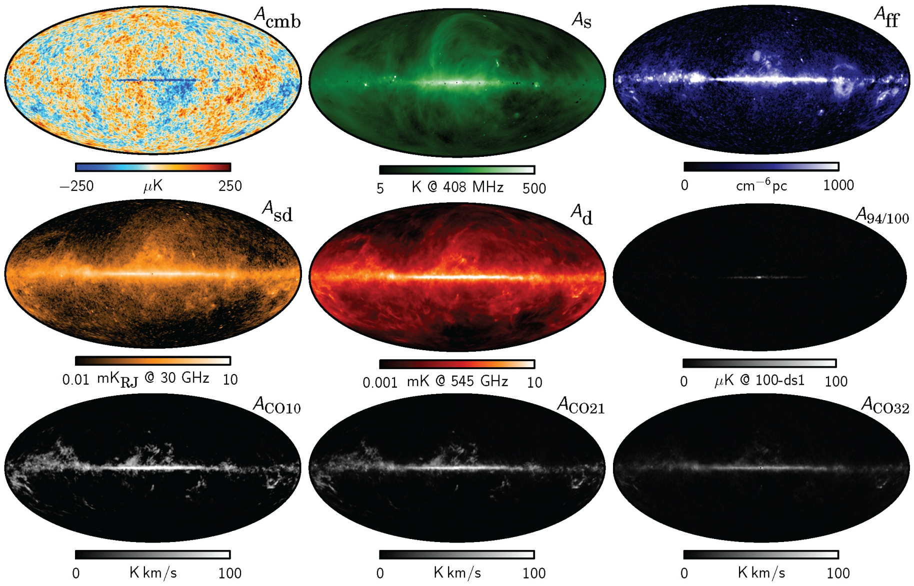

Figure 2.13: *Maximum posterior intensity maps derived from the joint analysis of Planck, WMAP, and 408 MHz observations (Planck Collaboration X 2015). From left to right, top to bottom: CMB; synchrotron; free-free; spinning dust; thermal dust; line emission around 90 GHz; CO J* $=$ *1* $\rightarrow$ *0; CO J* $=$ *2* $\rightarrow$ *1, and CO J* $=$ *3* $\rightarrow$ *2.* [2]

3

CORE: Cosmic Origins Explorer

L'universo è immenso, e gli uomini non sono altro che
piccoli granelli di polvere su un insignificante pianeta.
Ma quanto più prendiamo coscienza della nostra
piccolezza e della nostra impotenza dinanzi alle forze cosmiche,
tanto più risulta sorprendente ciò che gli esseri umani hanno realizzato.
Bertrand Russell

Observations of the CMB have played a fundamental role in establishing the current cosmological model. The Planck mission [95] gave us strong evidence for inflation model but the existence of a background of primordial gravitational waves remains unproven. In order to improve our knowledge of the universe we need to study the polarization properties of CMB anisotropies that remain largely untapped at the moment. At angular scales larger than 1° in the B-modes resides the most evident signature of the gravitational waves (GWs), the amplitude of which is still undetermined. B-modes are generated also by weak gravitational lensing of the CMB by intervening massive structures between us and the LSS peaking on 10' angular scales, i.e. all the structures on large scales. However, the main future request is to distinguish between the two sources of B-modes, thus we need to perform a precise measurement of the lensing effect. This measure provides not only the opportunity to derive a dark matter map distribution at times and scales inaccessible otherwise, but also to possibly uncover novel physics. One of the main scientific goals of CORE is the detection, precise characterization and scientific exploitation of CMB polarization B modes, from inflationary gravitational waves and from the weak gravitational lensing [23, 27, 35–37, 47, 70, 75, 85].

In Fig.3.1, is shown how well CORE will measure E and B modes and in particular primordial B modes, for two different tensor to scalar ratio: r=0.01 and r=0.001. It also shows the relative importance of various sources of error in polarization measurements. In particular the need for an accurate component separation at all angular scales to fully exploit the CMB polarization signals over a large fraction of the sky.

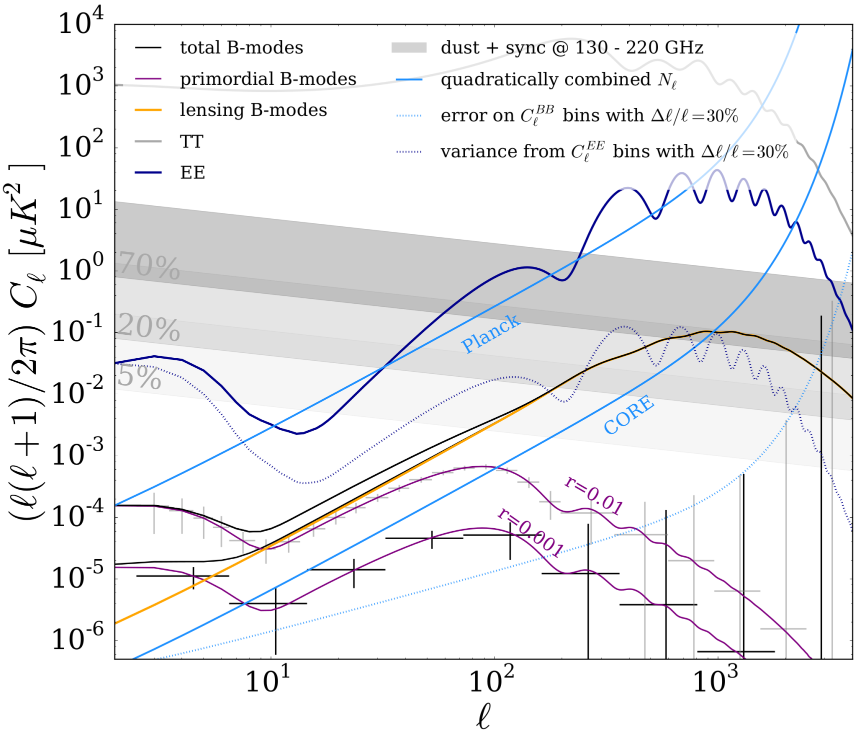

Figure 3.1: *CMB angular power spectra. The noise amplitudes for Planck and CORE are the cyan lines are compared with: TT (grey line) and EE (blue line) spectra, primordial and lensing B-modes (purple and yellow lines), in black the total B-modes. The grey shadows correspond to the expected level of foregrounds (dust and synchrotron) [37].*

3.1 The mission

The Cosmic Origins Explorer (CORE) is a mission proposed to the European Space Agency at M5 call as a fourth generation of CMB satellites after COBE [48, 49, 93], WMAP [92] and Planck [95].

CORE was proposed to map the CMB polarization pattern with unprecedented sensitivity. Thanks to its high resolution and sensitivity it will be possible to detect signature of B-modes from tensor to scalar ratio up to r $\sim 10^{-3}$, at a precision level of 3σ, close to the cosmic variance limit [37]. This is two orders of magnitude better than Planck sensitivity.

CORE mission is designed to produce definitive maps of the CMB polarization anisotropies at large and intermediate angular scales. If CORE will detect primordial gravitational waves, it will also provide the shape, n_t, of their spectrum over the largest possible range of cosmological scales.

CORE requires a full-sky survey in order to satisfy its primary purpose. Detecting B-modes from primordial GWs with $r \sim 10^{-3}$ requires a sensitivity of $\sim 2\mu$K arcmin [37] after foreground cleaning. At large scales, B-modes, produced by gravitational lensing of E-modes polarization, perform like a white noise around 5 μK arcmin. This lensing noise disturbs our measurements but using delensing algorithms it is possible to remove it at least partially. In this way we can access to lower amplitudes of primordial B-modes. The aim of CORE mission is to remove more than half of the lensing noise using the lensing map reconstructed internally, this is possible with a sensitivity of 2 μK arcmin (improve the reconstruction of lensing on small scales means a better or more accurate cleaning).

In order to have a full sky coverage, CORE will orbit around the second Sun-Earth Lagrange point (L2), the same position as Planck. The satellite will scan the sky with a dedicated scanning strategy combining a fast spin ($T_{spin} \simeq$ 2 minutes) around the spacecraft principal axis of symmetry, with a slower precession ($T_{prec} \simeq 4$ days) around an axis that is kept anti-solar to keep the solar flux on the spacecraft constant. CORE will also rotate around the Sun with a period of 1 year. The precession angle is $\alpha = 30°$ and the line of sight (LOS) is offset from the spin-axis by an angle $\beta = 65°$, as we will describe in section 3.4 in more details.

The CORE instrument uses an array of 2100 polarization-sensitive Kinetic Inductance Detectors (KIDs) at the focus of a 1.2 m aperture crossed-Dragone telescope. The full array produces an aggregate CMB polarization sensitivity of about 1.7μK arcmin. CORE is designed to map the full-sky CMB polarization with a mean noise level 25 times better than the Planck mission in amplitude, with an angular resolution of order 5' at frequencies $\sim$ 200 GHz. In order to control in an optimal way the foreground emission, the range of frequencies of CORE goes from 60 up to 600 GHz:

- Six channels from 60 to 115 GHz monitoring low-frequency and astrophysical foreground emissions, i.e. polarized synchrotron and spinning dust.

- Six channels between 130 GHz and 220 GHz observing the CMB.
- Seven channels between 255 and 600 GHz to monitor dust emission and to map cosmic infrared background (CIB) anisotropies.

The scientific program of the mission focuses on understanding the fundamental processes that gave raise to our observable universe through observations of the CMB polarization. The aims of the mission are [23]: i) understand the principal mechanisms that gave rise to primordial inhomogeneities in the early universe; ii) test the standard cosmological model; iii) try to find cosmological signals of extensions of the standard model of particles and interactions; iv) investigate the cosmic structures that generate secondary CMB anisotropies; v) understand the properties of foreground contamination for CMB polarization observations and the dust-obscured star-formation phase of galaxy evolution; vii) study the cosmic dipoles to test the cosmological principle at the largest scales.

3.2 Survey requirements

Based on the achievement of goals the mission design needs some requirements: sensitivity, angular resolution, and observations channels. We will see the details in this section. From Fig. 3.1, it is possible notice the following important issues: i) the multipoles, ℓ, smaller than 100 are dominated by foreground emission in polarization. In order to observe primordial and lensing B-modes with noise-dominated performance it is necessary an efficient component separation; ii) After component separation we have foreground residuals that are a source of potential bias; iii) For $\ell \leq 2500$ and $\ell \leq 1000$ the dominant uncertainty is the cosmic variance of the full-sky E-modes and of full-sky lensing B-modes respectively. For cosmological constraints based on polarization E modes and lensing B modes, it is preferable increase the size of the survey, to reduce the sampling variance rather than to observe smaller patches of the sky.

The performance of future CMB observations will be limited by the capability of removing foregrounds and to separate lensing from primordial B-modes over the largest solid angle.

From Chapter 2 the CMB anisotropies (both temperature and polarization anisotropies) are best observed at wavelengths between 1 mm and 1 cm, so around the peak of the CMB 2.725 K black body emission. In this frequency range, between a few 10 and few 100 GHz, ground-based observations are in a set of windows through which the atmosphere is sufficiently transparent. Unfortunately the atmosphere contributes to the total photon background, i.e photon noise. So, for an identical number of detectors, the mapping speed (i.e. the time that we have to wait to get a noise reduction of up to 1σ) of a space instrument is more or less 100 times better with respect to the ground one. In Sec.*2.6* we shown that CMB observations are contaminated at frequencies below 100 GHz, by: Galactic synchrotron, free-free, spinning dust emission and extragalactic radio sources. The thermal dust emission is instead dominant foreground at frequencies above 100 GHz. In addition, at frequencies above 200 GHz, anisotropies of the cosmic infrared background (CIB) dominates the emission of the observed sky. Several lines of CO emission at about 220, 225 and 230 GHz.

In polarization, synchrotron is polarized up to 75%, thermal dust polarization grater or equal to 10% at high frequencies and point sources are polarized at a level less than 1%. Observing the sky at several frequencies and exploiting the fact that the emission law of the CMB is different from that of most foreground emission processes we can remove the foreground contamination [39]. Looking at the previous missions, the sky has been observed in three (COBE), five (WMAP) and nine (Planck) frequency bands. This implies that future CMB data observations require more than ten channels in order to improve the sensitivity in the foreground cleaning. More precisely, we need four channels in order to parametrize the synchrotron and four channels in order to measure the thermal dust at high frequency.

Furthermore to investigate foreground residuals and systematic errors, Planck mission used comparisons between four foreground cleaned channels: 70, 100, 143 and 217 GHz. Over all we can conclude that ten channels is the minimum to monitor foreground emission in polarization. CORE with its 19 channels is perfect to this purpose [37].

In order to confirm the primordial origin of observed B-modes, CORE is designed to detect both the re-ionization and recombination bumps of the primary CMB. Measuring with great accuracy the polarization of CMB at large scales can improve measurement of the optical depth τ and check if temperature anomalies detected by WMAP and Planck are also found in polarization maps.

From Chapter 2, we know that the cosmic variance uncertainty depends on the inverse of the sky fraction at all multipoles. So, we need to observe a large sky fraction to reduce the error bars on the measured spectra.

In order to obtain information from CMB polarization, it is necessary to measure with high signal-to-noise ratio (S/N) both E and B-modes. In Fig.3.2 we compare the final error on polarization for a noise level of 2 μ K arcmin, the expected final sensitivity of CORE with theoretical spectra. This is sufficient in order to measure lensing B-modes with S/N $\simeq 2.5$ per mode in amplitude, with a beam ranging from 2' to 32".

E-mode observations are signal dominated up to $\ell \simeq 3000$, considering a beam of 4'. When the beam becomes bigger, E-mode measurements become degraded, hence, the ultimate E-mode measurement requires a noise level $\leq 2\mu$K arcmin and angular resolution $\leq 4'$. For primordial B-modes, under the assumption that the lensing contamination can be completely removed by other mean 2μK arcmin seems adequate to detect r=0.001. However, we also require that the mission provides an algorithm of delensing B-mode maps, so that the lensing residuals does not exceed much the noise level of the mission. Summarizing: the space mission should be designed to provide, after component separation, a clean CMB map over more than 50% of the sky with: a sensitivity in the 1.7-2.5 μK arcmin range and CMB angular resolution better than about 30'.

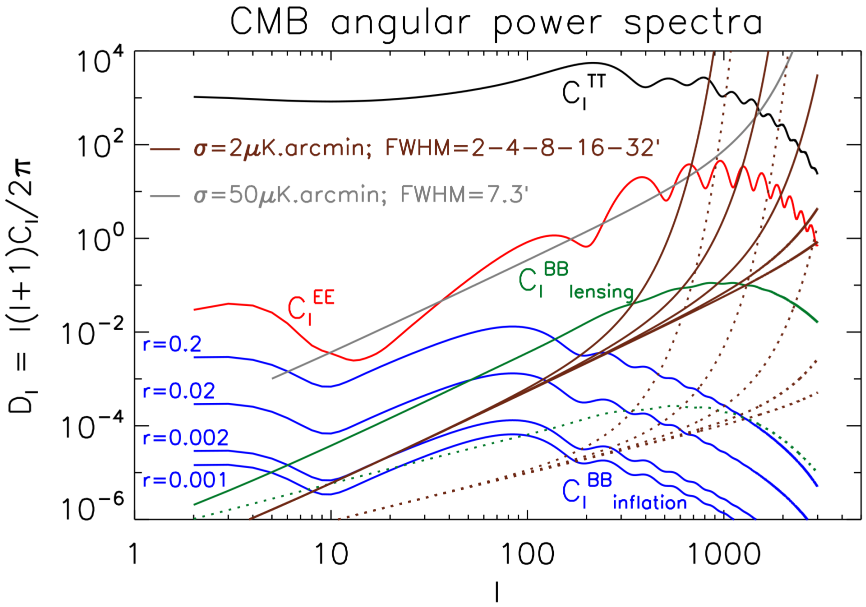

Figure 3.2: *CMB temperature and polarisation angular power spectra. The grey line corresponds to the spectrum of instrumental noise representative of the polarisation sensitivity achieved with the Planck mission. Solid brown lines show the level of noise for a map sensitivity of 2 μK arcmin and a beam of 2', 4', 8', 16' or 32' (from bottom to top), and dotted brown lines correspond to the error on C_ℓ for the same noise level and angular resolution.* [37]

3.3 Scientific instrument

CORE is designed to operate in a frequency range between 60-600 GHz and it is composed by a crossed-Dragone telescope, with 1.2 m projected aperture with an additional folding flat mirror. The focal plane is populated with 2100 polarization-sensitive Kinetic Inductance detectors, distributed among 19 frequency bands. All details of the detectors are shown in Fig. 3.3. The CORE reflectors are three small mirrors: the primary (M1) is 1.5 × 1.3 m^2, secondary (M2) is 1.4 × 1.3 m^2 and tertiary (M3) is 1.0 × 0.7 m^2 and they have masses of 42.8, 40.0, and 15.4 kg, respectively, see Fig.3.4. In order to reduce to negligible levels the stray light on the focal plane the telescope has shields and baffles. The first have a truncated-cone shape with a single aperture from which the telescope observe the sky. As we can see in the previous section the CORE Focal Plane (FP) presents 2100 detectors whose noise will not exceed the photon noise associated with the incoming background power.

channel GHz	beam arcmin	N_{det}	ΔT μK.arcmin	ΔP μK.arcmin	ΔI μK_{RJ}.arcmin	ΔI kJy/sr.arcmin	$\Delta y \times 10^6$ y_{SZ}.arcmin	PS (5σ) mJy
60	17.87	48	7.5	10.6	6.81	0.75	-1.5	5.0
70	15.39	48	7.1	10	6.23	0.94	-1.5	5.4
80	13.52	48	6.8	9.6	5.76	1.13	-1.5	5.7
90	12.08	78	5.1	7.3	4.19	1.04	-1.2	4.7
100	10.92	78	5.0	7.1	3.90	1.2	-1.2	4.9
115	9.56	76	5.0	7.0	3.58	1.45	-1.3	5.2
130	8.51	124	3.9	5.5	2.55	1.32	-1.2	4.2
145	7.68	144	3.6	5.1	2.16	1.39	-1.3	4.0
160	7.01	144	3.7	5.2	1.98	1.55	-1.6	4.1
175	6.45	160	3.6	5.1	1.72	1.62	-2.1	3.9
195	5.84	192	3.5	4.9	1.41	1.65	-3.8	3.6
220	5.23	192	3.8	5.4	1.24	1.85	-	3.6
255	4.57	128	5.6	7.9	1.30	2.59	3.5	4.4
295	3.99	128	7.4	10.5	1.12	3.01	2.2	4.5
340	3.49	128	11.1	15.7	1.01	3.57	2.0	4.7
390	3.06	96	22.0	31.1	1.08	5.05	2.8	5.8
450	2.65	96	45.9	64.9	1.04	6.48	4.3	6.5
520	2.29	96	116.6	164.8	1.03	8.56	8.3	7.4
600	1.98	96	358.3	506.7	1.03	11.4	20.0	8.5
Array		2100	1.2	1.7			0.41	

Figure 3.3: *Proposed CORE frequency channels. [35].*

The instrument is optimized to maximize its mapping speed by means of the widest possible FP of diffraction-limited detectors. The total number of detectors is limited by several reasons [35]

- the electrical power dissipated on the readout electronics, because impacts on the power budget;
- the electrical power dissipated on the cryogenic section, because impacts on the power budget of the cryo-system;

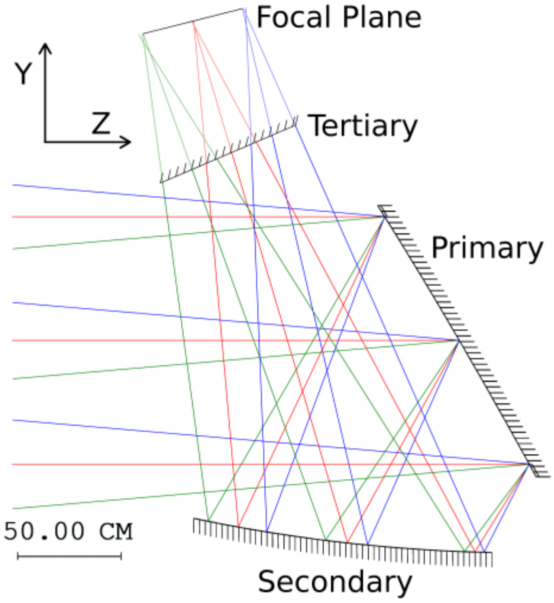

Figure 3.4: *Proposed configuration of the mirrors of the satellite. (www.core-mission.org)*

- the maximum allowed data rate;
- the diffraction limited field of view of the telescope, that depends on the size and configuration of the telescope;

In order to minimize the complexity of the system, every single detector will be chosen to cover the 60-600 GHz frequency range. The chosen range of frequencies covers: a) *low frequencies*, (between 60 and 115 GHz) where diffuse synchrotron radiation is dominant. The limited number of pixels available for the low frequencies represent a challenge, as the polarization sensitivity on chip, implying more development effort; b) *CMB frequencies* (130-220 GHz), where the CMB signal is maximum; c) *high frequencies* (255 - 600 GHz), where diffuse emission from dust is dominant. This range is covered by 19 frequency bands, this number was chosen to have a number of independent channels larger that the number of parameters required in a first-order description of all the relevant foregrounds.

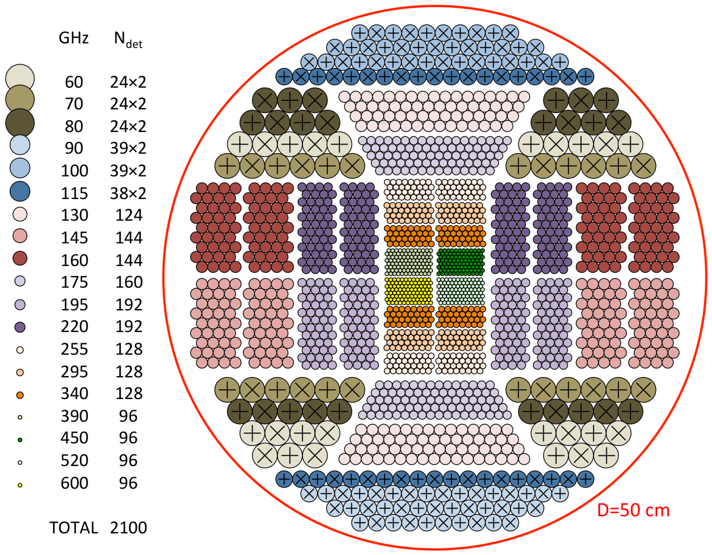

Figure 3.5: *Proposedconfiguration of the Focal Plane.*

3.4 Orbit and Scanning strategy

The payload and spacecraft geometry and the size of the telecommunication system are subject to the choice of the orbit. Moreover, the size of the orbit impacts the maximum elongation of the Earth and Moon with respect to the Sun as seen from the spacecraft and the required amount of propellant. As we anticipated before, CORE mission will be in orbit around the second Lagrange point (L2) of the Sun-Earth system, to guarantee that the Sun, Earth and Moon are away from the line of sight at all times. In Fig. 3.6, is shown a possible orbit around the Sun-Earth L2 point. The scanning strategy is selected to cover the full sky both in temperature and polarization. In order to have an adequate control of errors in the polarization angle and of residuals of I into Q and U after inversion of the linear system of observations we need that each pixel must be observed:

a) by the same detector with many different polarization angles over the course of the mission, preferably evenly spread in $[0, 2\pi]$ for best polarization sensitivity [31];

b) with different polarization angles on short timescales;

c) at very different times during the mission;

Moreover, the line of sight must never come close to the direction of the Sun, Earth, or Moon. The solar flux absorbed by the satellite should be constant in

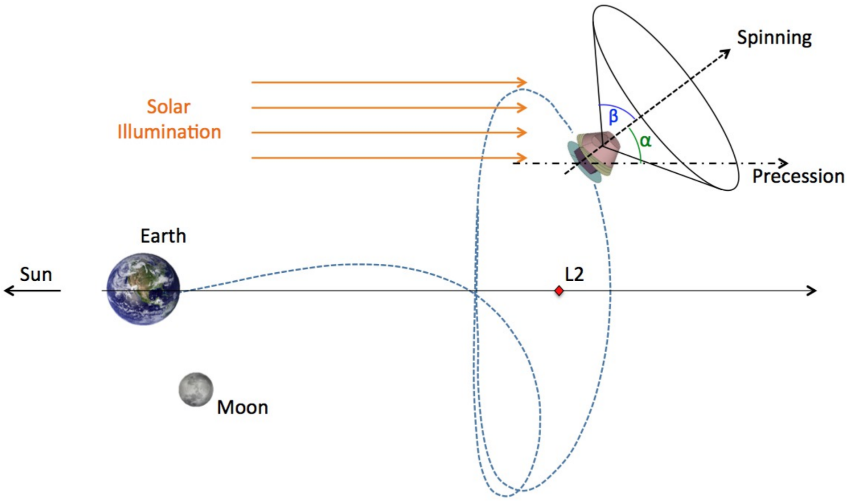

Figure 3.6: *Orbit and scanning strategy for CORE satellite.*

order to avoid strong fluctuations of the temperature of the payload.

For negligible impact of low-frequency noise, most of the pixels should be revisited on timescales of the order of $\frac{1}{f_k}$. Where f_k is the **knee frequency** of the low-frequency noise, i.e. the frequency at which the power spectrum of low-frequency noise equals that of the white noise. In order to minimizing the sampling variance we need to observe a complete sky. It may be useful to implement a scanning strategy that can concentrate observations in the cleanest regions of the sky during a mission extension, after identification of such regions during the main survey.

As we have seen in Sec.*2.5.2*, systematic effects generate confusion between Stokes parameters. Any contamination that does not exhibit a purely stochastic behaviour are considered as systematic effect.

In order to control the systematic effects it is necessary to combine the scanning strategy, the characteristics of the instrument and its calibration. Contrarily to some mission proposed like LiteBird, CORE does not have a rotating half-wave plate (HWP), an active polarization modulator. This implies that each pixel of the sky should be scanned with large span of different orientations, i.e. scanning angles. In order to obtain this a combination of spacecraft design and a choice of scanning strategy which combines: **spinning** at 0.5 rpm around a spin-axis coinciding with the axis of symmetry of the spacecraft; each detector scans a large quasi-circle of opening angle $\alpha \simeq 65°$ for each spin period; the spin axis precedes around the anti-solar direction with a period of 4 days and is oriented at 30° (β) from the Sun - Earth - L2 (anti-solar) direction; each detector covers about

45% of sky, for each precession; Reorientation of the precession axis with period 1 year to follow the yearly motion of L2 around the Sun. The only requirement to have a full sky coverage is:

$$\alpha + \beta > 90^\circ + \theta_{FP}, \tag{3.1}$$

where θ_{FP} is the angular radius of the imprint of the focal plane on the sky.
The **baseline case** is $\alpha + \beta = 95^\circ$ so that all the focal plane detectors will cover the full sky.
Keeping constant the angle between the spin axis and the anti-solar direction help to prevent fluctuations of the absorbed solar radiation on the spacecraft during the scan. This radiation would generate scan-synchronous fluctuations of the payload temperature seen by the detectors as spurious signals. Moreover, in order to re-observe each sky pixel over small and large timescales, we need to combine a spinning, a precession, and a revolution with very different periods. We chose 2 minutes (spinning), 4 days (precession) and 1 year (observation period) to observe each pixel with a wide span of scanning angles [23].

3.5 The map-making approach for CMB experiments

Construction of the CMB map from time-ordered data (TOD) is a foundamental part of the data analysis of CMB experiments. The first map-making approch was developed for COBE experiment [69] and it is a differential measuring scheme effective in reducing correlated noise. Subsequently this approch is extended to maps that contain millions of pixels for WMAP [102], Planck and CORE. The goal of map-making is to evaluate an estimator of the sky representation, $\widehat{m}$, from a vector of observation.
In this thesis we used a map-making method called MADAM (Map-making through Destriping for Anisotropy Measurements) [61]. The basic idea of the method is: the low frequency component of the instrument noise in TOD is modelled as a superposition of simple base functions, whose amplitudes are determined by means of maximum-likelihood analysis, involving the covariance matrix of the amplitudes. The covariance matrix is computed from the noise spectrum, assumed to be known.

It is possible to define a relation between the observations, y, and the sky:

$$y = Pm + n', \tag{3.2}$$

where P is the "pointing" operator, m is the pixelized CMB map and n' is the noise contribution.
It is convenient chose P as a simple pixelized pointing matrix where the signal part of a sample is just the corresponding pixel value. In case of polarized detectors, the signal is a linear combination of the intensity and polarization pixel values. The noise matrix n' is unknown, it must be estimated from the data, it exhibits minimum variance among all linear estimators and it becomes the maximum likelihood solution if the noise is drawn from a multivariate Gaussian distribution. This solution unfortunately is computationally intractable for a real world situation, in which we have billions of time samples and millions of map pixels. The problem can be effectively solved by resorting to iterative techniques, typically employing a conjugate gradient solver [74].
Dividing the noise contribution into a correlated and white noise components, and modelling the correlated part as a sequence of uniform baselines, we obtain:

$$n' = Fa + n, \tag{3.3}$$

where a is the amplitude of the baseline and F spreads it into TOD and consists of zeroes and ones, indicating which samples belong to which baseline. The baseline is the length of a chunck of data in which we have divided the entire TOD.
Considering the white and correlated noise independent each others, the total noise covariance matrix becomes:

$$C_t =< n'n'^T >= FC_aF^T + C_n, \tag{3.4}$$

where $C_n =< nn^T >$ is the white noise covariance, $C_a =< aa^T >$ is the covariance matrix for the component amplitudes a, and $< ... >$ denotes the expectation value of quantity in brackets. The goal of the map-making is to find, for given data y, the maximum-likelihood estimate of m and a simultaneously. Maximum likelihood analysis yields the chi-square minimization function:

$$\chi^2 = (y - Fa - Pm)^T C_n^{-1}(y - Fa - Pm) + a^T C_a^{-1} a. \tag{3.5}$$

We want to minimize the last equation with respect to both a and m. So, minimization with respect to m gives:

$$m = (P^T C_n^{-1} P)^{-1} P^T C_n^{-1} (y - Fa). \tag{3.6}$$

Substituting Eq.(3.6) into Eq.(3.5) and minimizing with respect to a, we obtain an estimate for the amplitude vector a which is:

$$(F^T C_n^{-1} Z F + C_a^{-1}) a = F^T C_n^{-1} Z y, \tag{3.7}$$

where $Z = I - P(P^T C_n^{-1} P)^{-1} P^T C_n^{-1}$. Matrix P depends on resolution and for that we can define two different pointing matrices: matrix P_c is constructed at the destriping resolution and matrix P_m at the map resolution. The MADAM code products also the binned map and the sum map, that are useful in signal-only simulations and in the case of incomplete sky coverage, since it is well defined also in pixels with poor sampling of polarization directions respectively. Equations (3.6) and (3.7) are the basis of the MADAM map-making method, for more precise description see [60, 61] .

3.6 Low frequency noise

The precise control of the systematic effects (due to non-idealities in the instrument) is very important to achieve the science goals of future CMB polarization observations. These non-idealities impact the shape of the response in space (e.g. beam) and in time or frequency (e.g. bandpass).

One of the most important is the **cross correlated** noise contribution: a source of potential concern for the densely packed focal planes of the current and forthcoming generation of CMB experiments.

For CORE experiment it is assumed that the noise of the i-th detector has the following spectral behaviour:

$$n_i = \widehat{n}_i + n_c, \tag{3.8}$$

$$< \widehat{n}_i \widehat{n}_i >= A \left[1 + \left(\frac{f}{f_k} \right)^{-1} \right], \tag{3.9}$$

$$< n_i n_j >=< n_c n_c >= A \left[C + \left(\frac{f}{f_k} \right)^{-2} \right] \; for i \neq j, \tag{3.10}$$

where $\widehat{n}_i$ is the auto-correlated noise component, n_c is the cross-correlated noise component.

We can define an instrumental noise correlations for low and high frequency, between 10 mHz and 10 Hz. Noise power below this band is "low frequency" and noise above this frequency is "high frequency". Low frequency noise correlations are driven by the electronic amplification of the signal and usually fit well the $1/f$ noise model:

$$P(f) \propto \left(\frac{f}{f_k}\right)^{\alpha} \tag{3.11}$$

where the P is the noise power spectral density, f is frequency, f_k is the knee frequency and α is the slope of the spectrum.

The instrumental noise spectrum at high frequency is close to flat (white). For most radiometer detectors this means that the overall noise spectrum is well characterized by:

$$P(f) = \frac{\sigma^2}{f_s}\left[1 + \left(\frac{f}{f_k}\right)^{\alpha}\right] \tag{3.12}$$

where σ is the white noise standard deviation and f_s is the sampling frequency.

3.7 Mitigation of Systematic Effects

The impact of systematic effects plays a crucial role in the analysis of CMB experiments [3, 5, 16, 17, 42, 94]. A lot of papers in literature focus specifically on polarization specific systematics and their treatment [58, 71, 79, 91].

The term systematics, in the CMB community, includes contamination that changes from ideal. Under this assumption also the **white noise** is considered as a systematic. Moreover, is considered as systematic the correlated or "$1/f$ " noise i.e. a purely random component with a zero expectation value.

In this thesis we used a realistic simulation pipeline in order to produce time ordered data for a year of observations. Then we reduce to intensity and polarization maps using a state of the art map making code.

3.7.1 Data analysis: Simulations

The Planck mission has shown that simulated data are crucial for the success of a CMB space mission. Simulations are essential at the beginning of the mission, because they support the optimization of the design of the spacecraft, telescope,

and instruments, and to test and validate the data analysis pipelines before launch. After launch, the simulation pipeline should include instrumental and systematic effects to characterize the realistic properties of the instrument and data products and to support the science exploitation. The two key ingredients of the simulation pipeline are the **instrument model** and the **sky model**. Thanks to simulation pipeline it is possible to generate new simulations immediately if the instrument model is updated anytime during the analysis. From that the data analysis pipelines and the simulation pipeline must be integrated. The sky model is able to simulate astrophysical emission over all the frequency range of CORE, moreover it is also continuously updated during the course of the analyses. So, optimization of the instrument and the model are important to guarantee that the dataset obtained will be sufficient to achieve the science of the goals. The validation and verification of the data analysis pipeline plays a critical role to ensure that the science can be extracted from the mission dataset.
In Fig.3.7 there is an overview of a proposed pipeline for CORE. The data simulation operator combines the mission model (included the detector properties, focal plane layout, optical path, scanning strategy, data-flagging, CMB and foregrounds) and the sky model the CMB foregrounds to generate time ordered-data (TOD). The steps of the analysis pipeline are: pre-processing, map-making,

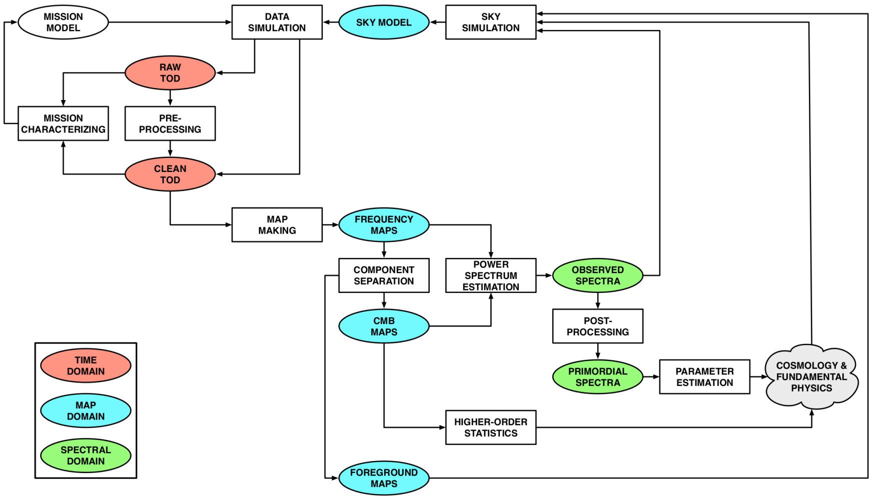

Figure 3.7: *Schematic of simulation and analysis pipeline. The rectangular operators acting on oval data objects, which may be time samples (red), map pixels (blue) or power spectra (green) [75].*

component separation, power spectrum estimation and post-processing. The first three guarantee the mitigation of the systematic effects in the data domain,

otherwise the last two help in the reduction of the statistical uncertainties. The spectral and map-domain products are used to constrain the parameters of the models of cosmology and fundamental physics. Moreover data representations can be used to provide feedback to refine the mission and the sky models.
To generate simulations, inside the Planck collaboration [5], it has been developed a package called **TOAST** (Time-Ordered Astrophysics Scalable Tools) [1]. This code is a useful tool to study $1/f$ contamination. We used this code to study $1/f$ contamination inside the CORE collaboration.

3.7.2 TOAST: Time-Ordered Astrophysics Scalable Tools

Telescopes which collect data as time-streams give us a unique set of analysis challenges. Detector data contains noise which is correlated in time and sources of correlated signal from the instrument. Large pieces of data must often be analysed simultaneously to extract an estimate of the sky signal. TOAST is implemented as a python wrapper and data management layer into which new modules can be dropped, coupled with compiled libraries.
TOAST has been extensively validated, verified and used in the Planck full focal plane simulations [5] but also for the CORE and LiteBIRD satellite missions. In this thesis the TOAST framework uses some libraries: a) *pointing library*: generates, for each detector, the dense-sampled pointings from the sparse-sampled satellite boresight pointing; b) *noise simulation library*: the TOAST noise simulation library, generates time-streams of noise from each detector piecewise stationary noise power spectral density functions; c)*libCONVIQT (beam convolution) library* [2]: generates time-streams of sky signals from each detectors full asymmetric beam and pointings and the simulated sky being observed [82]; d) libMADAM (map-making) library [3], makes a destriped map of the sky given some set of time-ordered data and pointings, for some set of detectors [61].
The first two are internal libraries of TOAST and the last two are external libraries. To evaluate the impact of the asymmetric beams TOAST generates a sky signal maps using a combination of a+c+d (destriped). In this thesis we use a+b+d to generate coverage and noise maps in order to evaluate the impact of correlated noise and scanning strategies. With Madam library we generate noise maps from timelines simulated with TOAST.

---

[1] http://github.com/hpc4cmb/toast

[2] http://github.com/hpc4cmb/libconviqt

[3] http://github.com/hpc4cmb/libmadam

3.7.3 Simulated noise maps

The parameters that we selected as input to TOAST to produce noise maps are shown in Tab. 3.1. In the following analysis we choose the CORE baseline scanning strategy with spin angle of 65°, precession angle of 30°, spin period 120s and precession period of 4 days. We consider timelines containing only instrumental noise and we simulate an year of observations divided into segments of 24 hours. We assume a noise model with power spectrum density:

$$P(f) =< n_i n_i >= A\left[\left(\frac{f}{f_k}\right)^{\alpha} + 1\right], \tag{3.13}$$

where A is the amplitude, f is the frequency, α is a slope (equal to 1) and f_k is the knee frequency [75]. Considering a CORE two detector system, a reasonable choice for the knee frequency is about 20 mHz the amplitude corresponds to a NET of $53.2\mu K\sqrt{s}$ at 145 GHz.

In the following analysis we consider a pair of orthogonal detectors at 145 GHz at the same position in the focal plane, i.e both at the boresight oriented at -22.5° and 67.5° with respect to the scan direction. This choice produces angular power spectra of EE and BB with similar amplitudes and equalizes the noise power in Q and U parameters. However this choice becomes irrelevant for maps produced by a large number of detectors, because each detector will have different angles orientations, averaging the observation and obtaining equal noise power in Q and U.

In addition, we consider two pairs of detectors at ±4.7° with respect to the boresight along the direction orthogonal to the scan direction to simulate the observable properties of the detectors at the edge of the focal plane. These are labelled as "high" and "low" detectors in the Tab. 3.1. These have the same polarization orientation as the boresight detectors. In Fig.3.8 we show the hit map for two boresight detectors after one year of observation with an estimate of the total diffuse polarized foregrounds at 70 GHz. This estimate was obtained using the Planck 353 GHz and 30 GHz polarized maps as dust and synchrotron templates respectively. We can see, also, the presence of irregular small-scales features, these would be diluted when considering a large number of detectors. Thanks to it large precession, CORE will obtain a sky coverage of 45% in only 4 days and a complete sky coverage in only 6 months of observation.

Using the scanning strategy described above, all pixels in the sky have been observed at least 200 times. Moreover, from this exercise we find that the CORE scanning strategy produces a high signal-to-noise sampling of regions that are

Parameter		Value
Precession angle [°]		30
Spin angle [°]		65
Precession period [days]		4
Spin period [s]		120
Hours of observation per day [h]		24
Length of a single chunk of TOD [h]		24
Observation duration [days]		366
Number of detectors		2
Frequency [GHz]		145
FWHM [arcmin]		7.68
Sampling rate [Hz]		84.97
Polarization orientation detector 1 [°]		-22.5
Polarization orientation detector 2 [°]		67.5
Knee frequency f_k [mHz]		0, 10, 20, 50
Noise slope α		1.0
NET [μK$\sqrt{\text{s}}$]		52.3
Deviation from boresight [°]	'high'	+4.7
	'low'	-4.7
$\mathrm{N_{side}}$		1024
Baseline (with noise prior) [s]		1.0

Table 3.1: *Parameters supplied to TOAST to generate the baseline simulations. See text for details. The sampling rate is chosen to ensure four samples per beam FWHM.*

remarkably clean of polarized foreground emission.

In the following section, we analyse the white noise covariance matrix for the chosen scanning strategy. Using a 3x3 symmetric positive matrix for (I,Q,U) in each pixel and ignoring $1/f$ contributions (i.e. correlations between pixels) we tested the efficiency of the CORE scanning strategy.

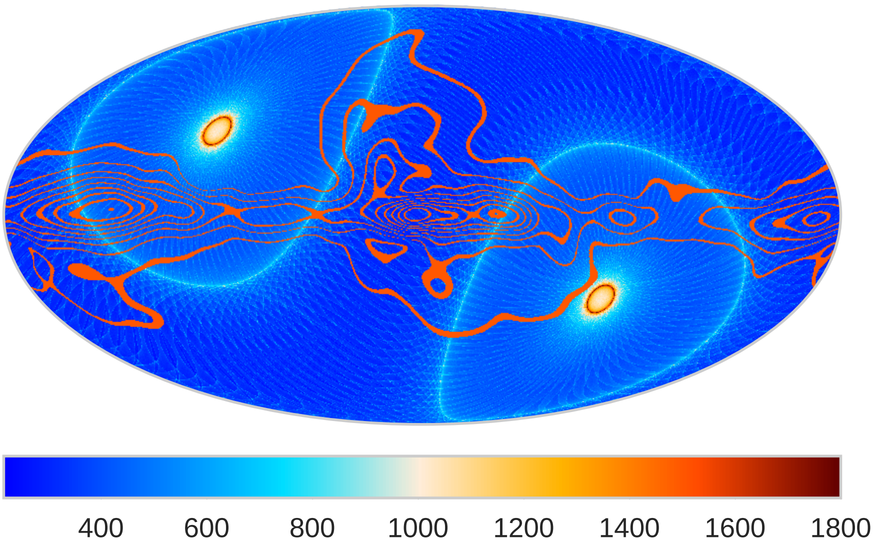

Figure 3.8: *Hit map for a pair of detectors located at the center of the focal plane after one year of observation and it shown in Galactic coordinates. The orange contours is an estimate of the polarization amplitude of the foregrounds at 70 GHz. The outermost contour corresponds to 1.3 μK in polarized intensity, and the subsequent contours to further steps of 1.3 μK.*

3.7.4 Baseline scanning strategy

The maps of the elements of the 3x3 white noise covariance matrices and their histograms (produced by madam for the case of boresight detectors in Galactic coordinates) are shown in Fig.3.9 and Fig.3.10 respectively. Notice that IQ and IU correlations, in Fig.3.9, are very weak. Looking at Fig.3.10 larger values of the histograms reflect larger pixel variance of the noise maps. The histograms do not have large tails (we do not have pixels that have noise larger then the mean value), total intensity has smaller values with respect to polarization by a factor of 2. In particular QQ and UU histograms are very similar, QU present significant correlation features. When multi-detector map is produced, using a large number of detectors of a single frequency channel, we expect these features to scale down. In Fig.3.10, we show also the histograms of the noise covariance matrices for the high and low detectors (blue and red histograms). We analysed the case at the edge of the focal plane to check that the detectors in this position are able to cover the all sky given the CORE scanning strategy. This does not happen thanks to the choice that the sum of the spin angle and the precession angle is greater than 90° for the entire focal plane. The lowest sum is reached by

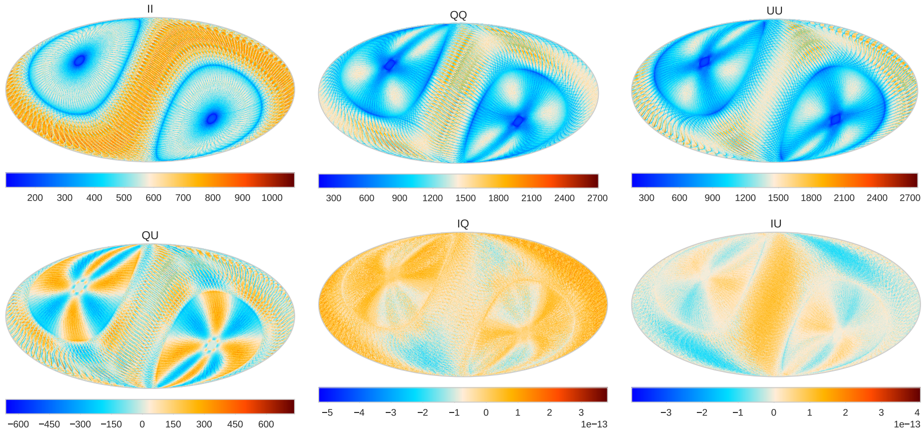

Figure 3.9: *Elements of the white noise covariance matrix for a pair of boresight detectors displayed as maps in units of μK^2: II, QQ, UU, QU, IU and IQ in galactic coordinates.*

low detectors where it is equal to 90.2°. The histogram shapes for the high and low cases are similar to the boresight ones and there aren't anomalous values of the noise covariance matrix elements.

We compute the ratio of the smallest and the largest eigenvalue of the 3x3 covariance matrices in each pixels obtaining maps of the so called reciprocal condition number (RCN). We used RCN because is an useful indicator to check if the matrix is ill-conditioned and verify the purity of the map-making solution for the Stokes parameters. In the ideal case the RCN takes maximum value of 0.5, otherwise values too low may leave the system vulnerable to non-idealities. For an optimal inversion we can set two basic requirements: an average value across the histogram higher than 0.25 and no pixels with values lower than 10^{-2}. Histograms of the RCN for the boresight, high and low cases are shown in Fig. 3.11. High detectors present lower RCN, whilst low detectors show slightly higher RCN. High and low detectors present respectively lower and slightly higher RCN. We obtain an average value of about 0.41 and no pixels with values lower than 0.2. So, the separation of the Stokes parameters for the CORE scanning strategy is very good. This also shows that CORE can efficiently modulate polarization without a rotating HWP.

In this thesis we also compute the angular power spectra (APS) of the simulated noise maps. The noise APS allow to evaluate the destriping efficiency of MADAM in controlling spurious low-frequency contributions. In Fig.3.12 are shown the average TT, EE and BB APS from 1000 noise realizations for the boresight (green line), high (red line) and low (blue line) detectors and 1σ dispersion of the boresight case. The APS of different detectors are very similar, only the APS of

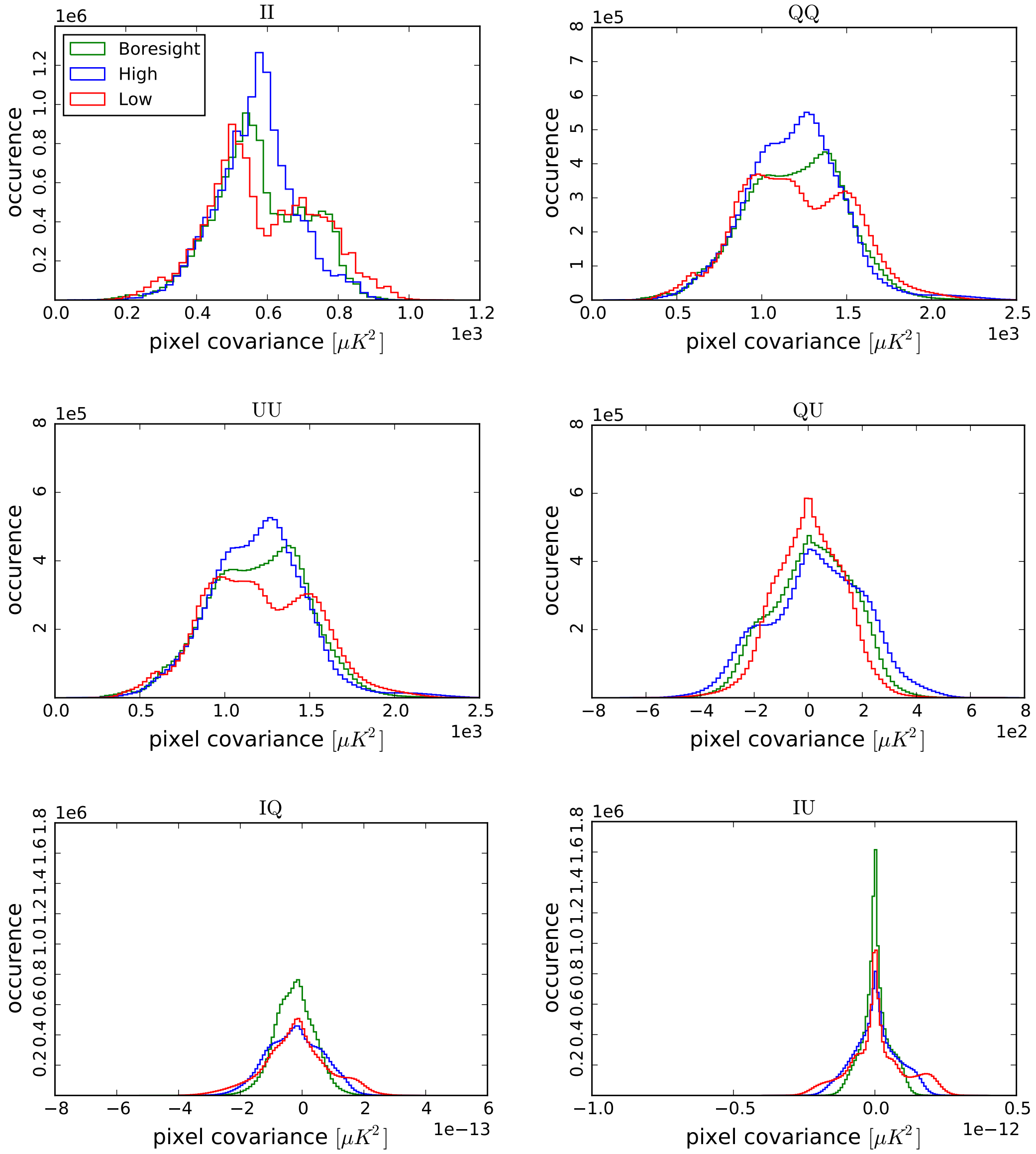

Figure 3.10: *Histograms of the covariance matrix in galactic coordinates.*

low detectors shows a little lower amplitudes than the other two. EE and BB spectra are more or less the same as a result of the choice of the polarization orientations of the detectors. Due to residual $1/f$ contribution after destriping all spectra present a low multipole (large scale) excess. All the analysis about the impact of different knee frequencies is discussed in the following sections.

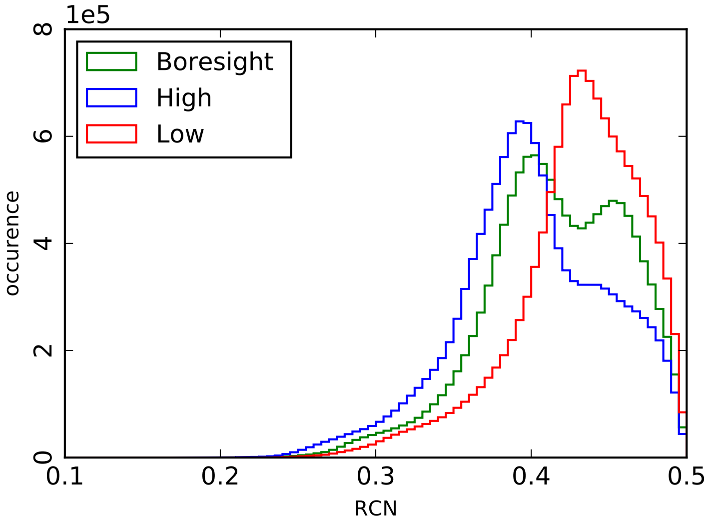

Figure 3.11: *Histograms of the reciprocal condition numbers for the boresight (green line), high (blue line) and low (red line) detectors.*

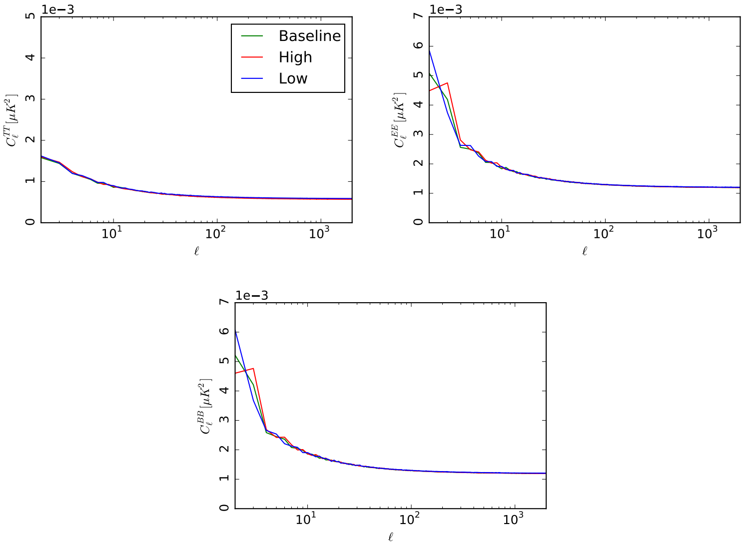

Figure 3.12: *Angular power spectra for TT , EE and BB of the baseline simulations for the boresight, high and low detectors. The 1σ dispersion for the boresight case is the shaded regions.*

Parameter	Baseline	Tweak 1	Tweak 2	Tweak 3
Precession angle [°]	30	32	34	36
Spin angle [°]	65	63	61	59
	Tweak 4	Tweak 5	Tweak 6	Tweak 7
Precession angle [°]	38	40	45	50
Spin angle [°]	57	55	50	45

Table 3.2: *Parameters modified with respect to Table ?? to obtain tweaked cases to evaluate a possible optimization of the CORE scanning strategy. The first column gives the baseline parameters.*

3.7.5 Perturbing the scanning strategy

In this thesis, analysing the effect of varying the spin and precession angles, we explore possible optimizations of the CORE scanning strategy. These seven pairs of precession and spin angles keeping the sum of these angles equal to 95° to preserve a full sky coverage in every position of the focal plane. We considered seven "tweaked" cases are compared to the baseline CORE scanning strategy in the Table 3.2 the chosen values. In Fig.3.13 we show the RCN of the noise covariance matrices or considering the boresight, high and low detectors. The RCN are all similar with average values around 0.4 for all cases. In particular, larger tails towards lower RCN values for the cases 1,2,3,4 and 5 are found and their average RCN is slightly lower. The other two considered cases (6 and 7) show slightly improved RCN with respect to the baseline. When we consider the high and low detectors the improvements are less evident. Comparing the case number 6 with the baseline we have a highest mean RCN equal to 0.42 in the boresight case. However, this value is very close to the one that we found for the baseline. In 3.14 we show the APS (average of 10 noise realizations) of the noise maps for the boresight, high and low detectors. The APS of the tweaked

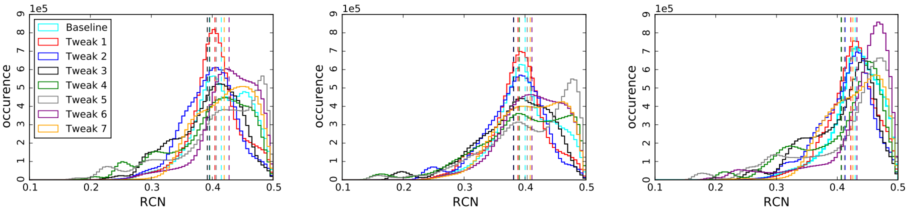

Figure 3.13: *Histograms of the RCN for the boresight (left), high (centre) and low (right) detectors in the tweaked cases.*

cases are compared to the baseline and its 1σ dispersion delimited by the shaded region. On small scales, the APS are more or less identical while we obtained larger differences at large scales, but all are well inside the 1σ dispersion.

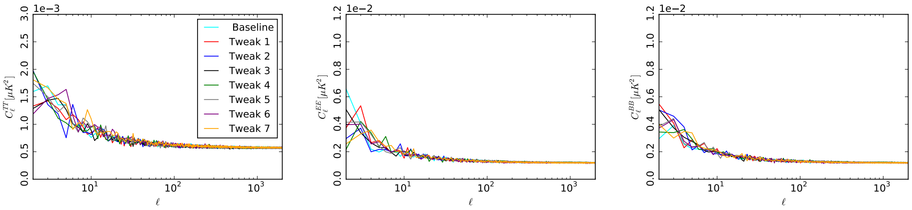

Figure 3.14: *TT (left), EE (centre) and BB (right) APS of the baseline simulations for the boresight detectors compared to the tweaked cases.*

3.7.6 1/f noise performance

We generate 1000 Monte Carlo (MC) realizations and apply MADAM to produce destriped noise maps. The results for f_k of 10 (red line), 20 (blue line), 50 mHz (black line) are shown in Fig.3.15. and the results are compared with the white noise case with for knee frequency of 0 mHz. The cyan region corresponds to the 1σ dispersion. In the same Figure, we show the results for a pair of low detectors (dashed lines) and high detectors (dotted lines).

In the figure we can find the effect of the destiping residuals, i.e. there is a larger amplitude of the noise spectrum at large scales. The residuals also increase with increasing f_k. Looking to $f_k = 10mHz$ case, the APS is very close to the 1σ dispersion of the white noise. It means that, in first approximation, we are not able to distinguish between noise maps from the pure white noise case (in temperature and polarization) for $f_k < 10mHz$. Consequently for $f_k < 10mHz$ the low frequency noise have negligible effects.

We can compare the amplitude of $1/f$ noise residuals with primordial polarization signal. The proposed configuration of the CORE focal plane has 2100 detectors in a range from 60 to 600 GHz.

We can infer the impact of auto correlated detector noise extending it to the entire focal plane using the above results with the assumption of no correlated noise among the detectors. We produce a noise power spectrum from the combination of six cosmological channels, between 130 and 220 GHz, by inverse noise weighting. After that we rescale the amplitude of the noise APS derived from a pair of detectors to match this noise spectrum at $\ell = 300$. In Fig.3.16 we compare the results with the EE and BB theoretical CMB spectra, for different

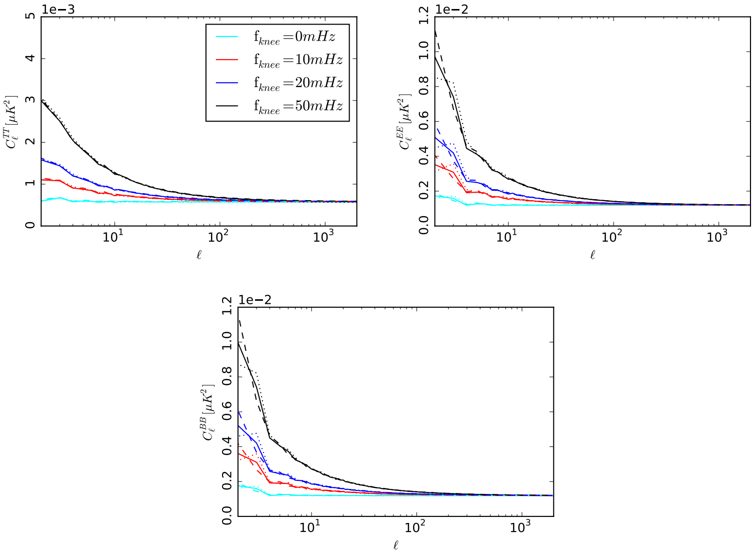

Figure 3.15: *TT (left), EE (centre) and BB (right) APS of the baseline simulations for the boresight detectors considering several knee frequencies f_k. We show the APS from the boresight detectors (solid lines), high detectors (dotted lines) and low detectors (dashed lines).*

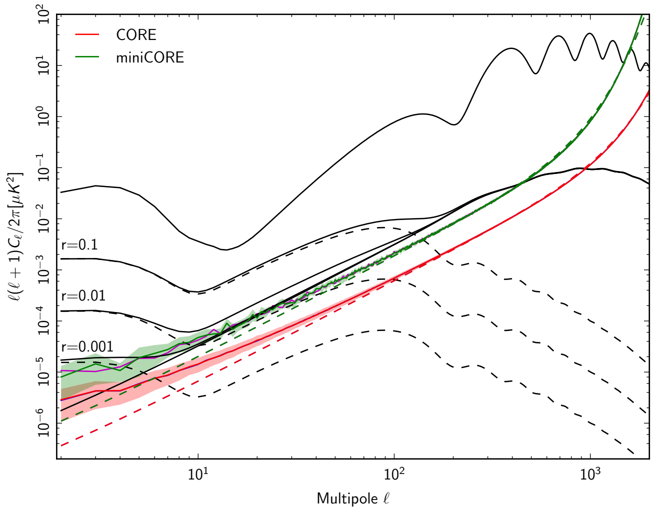

Figure 3.16: *Polarized noise angular power spectra (coloured lines) in EE and BB for CORE (red and blue lines respectively) and miniCORE (magenta and cyan respectively), considering all channels between 130 and 220 GHz, compared to EE and BB CMB theoretical spectra for several values of the tensor-to-scalar ratio r (the solid curve includes lensing B modes). The shading corresponds to the $1\,\sigma$ uncertainty region. [75]*

values of the tensor to scalar ratio r, while the other cosmological parameters are kept to the Planck 2015 best fit values. In Figure 3.16 the red dashed line shows the noise spectrum from the inverse noise weighting of the six CMB channels. The solid line corresponds to the noise APS of a pair of detectors (average of 1000 noise realizations, $f_k = 50$ mHz and a beam of 5 arcmin). We show both EE (blue line) and BB (red line) noise APS. They are almost indistinguishable because overlapped.

The effect of $1/f$ noise is remarkable at $\ell \leq 100$. However, even in this pessimistic assumption of $f_k = 50$ mHz, the noise APS is well below the BB spectrum for r $= 10^{-3}$ at $\ell \leq 10$.

In the same Figure we also show the forecasted noise spectra EE (magenta line) and BB (cyan line) for the so-called miniCORE design, a downscoped configuration of CORE [35]. For this exercise we consider the miniCORE parameters: beam FHWM equal to 11.9 arcmin for a 145 GHz, a sampling rate of 54.8 Hz and 10 noise realizations. Except for the number of the detectors per channels the other parameters are the same used for CORE. For miniCORE the BB APS for $r = 10^{-3}$ is closer to the noise level, so this design still allows a lot of margin for an accurate measurement of tensor modes in view of $1/f$ residual contamination. MiniCORE, with respect CORE, presents: a reduction of the diameter of the telescope aperture to 80 cm, a reduction of the number of detectors (900 instead of 2100) and the removal of all channels with frequency below 100 GHz (15 frequency bands in place of 19). The reduction of the requirement on $\sigma(r)$ by a factor of 3 (MiniCORE alone vs CORE alone) translates in a reduction of the requirement on the sensitivity by a factor of $\sqrt{3}$. Despite the noise level for miniCORE is closer to the BB spectrum for $r = 10^{-3}$, this design still allows plenty of margin for an accurate measurement of tensor modes in view of $1/f$ residual contamination, especially considering that $f_k = 50$ mHz is taken here as a worst case scenario [75].

4

LSPE: Large Scale Polarization Explorer

Per quanto difficile possa essere la vita,
c'è sempre qualcosa che è possibile fare.
Guardate le stelle invece dei vostri piedi
Stephen Hawking

The advent of space-based observations has transformed amog others the fields of Earth and planetary science and astronomy. The unique position, the long based time of observation and the clarity of the image offered by space missions in space resulted in an understanding of the universe to unprecedented levels. However, these advances come at a significant cost. For any possible space mission, even the most cost-effective design and implementation requires substantial financial resources and launch facilities with costs that are affordable only at the national agency level. Balloon-borne experiments are limited by integration time due to small duration flights or Sun disturbance, limiting the mapping of a large portions of the sky. Although space missions have obtained major achievements in the study of the CMB (like Planck, WMAP and COBE) thanks to the full coverage with high sensitivity and good control of systematics, ground and baloon-borne missions have also given extremely interesting contributions to the field.

Balloon-borne missions support all science disciplines: Astrophysics, Planetary Science, Heliophysics, Earth Science and Technology Development. Moreover, scientific balloons have produced important forefront science discoveries. For example, Boomerang [33, 64, 76] and MAXIMA [65, 83] mapped the anisotropies of the CMB. Their results confirmed the inflation model of the universe expansion

and this is one of the great scientific confirmations of the 30th Century. The relatively low cost, the easy access to balloons and the quick turn-around response times created a large interest for using this platform to perform new science.
The improvement in sensitivity implies the reduction of the level of noise and this requires more detectors. This is easily affordable in balloon experiments in close future.
A polar night flight balloon mission presents specific technical problems in addition to those of a normal day-time flight: the payload thermal management, the supply power of the instrument and the telemetry. The first problem is due to the absence, during the polar night, of the solar radiation (necessary to warm up the instrument) in fact the temperature of the stratosphere is around $-80°C$. This conditions impacts on the electronic on board, so it is necessary insulate it thermally. For the second one we need an electrical energy storage close to 1 GJ. A possible solution is to use lithium batteries, which feature high energy density and can operate in vacuum and at very low temperatures. In this case the cost is significant. Data transmission is also a problematic task. LSPE will produce a raw data rate of about 400 kbps, which is entirely stored onboard. Essential housekeeping information is transmitted through the iridium network, to check the performance and the evolution of the observing program.
This Chapter is dedicated to the analyses and description of the LSPE experiment. So we will describe briefly the LSPE mission (in Sec.*4.1*) and describe tools used in this thesis the: LSPE simulator (Sec.*4.2*) to simulate the scanning strategy of the balloon, template fitting technique (Sec.*4.3*) to clean the CMB maps from foreground contaminations and Cromaster (Sec.*4.4*) to extract the APS of the LSPE maps.

4.1 The LSPE instrument

The Large Scale Polarization Explorer (LSPE) is a balloon-borne experiment with the main scientific goal of measuring B-mode CMB polarization at large angular scales. The balloon will observe the sky from the stratosphere limiting the atmospheric contamination and during the polar night to limit the solar contamination.
The mission consists of two different experiments: a ground-based experiment **STRIP** (STRatospheric Italian Polarimeter) [9, 18], which is the low frequency instrument and balloon counterpart **SWIPE** (Short Wavelength Instrument for

the Polarization Explorer) [34], designed to survey the sky at high frequencies. The experiment has been designed to improve with respect to previous efforts in three areas: i) sensitivity; ii) systematic effects; iii) foregrounds. The sensitivity is improved using arrays of photon-noise limited detectors. The control and mitigation of the systematic effects will be improved using several levels of modulation and a half wave plate (HWP) for SWIPE. Both SWIPE and STRIP are sensitive to the W band, using orthogonal technologies and thus providing an additional check for systematic effects. The frequency range covered by the two instruments corresponds to the region where the ratio between polarized CMB signal and polarized foregrounds is maximum. This allows us to use efficiently component separation techniques. Our current understanding of the universe is strongly supported by observations coming from both studies of large scale structure via galaxy surveys and from precise CMB measurements. CMB polarization measurements represent a unique tool to probe energy scales as high as 10^{16} GeV, inaccessible to any particle accelerator. The primordial B-modes amplitude is usually parametrized by the tensor-to-scalar ratio, r, see Sec.*2.4.1*. However, primordial B-mode signal is very small compared to polarized foregrounds and instrumental noise. At frequencies below 60 GHz the most important effect is the synchrotron emission, above 90 GHz the polarized interstellar emission dominates. LSPE should be optimized to achieve high sensitivity to have a low noise contamination while covering a wide spectral interval to improve the component separation. For these reasons SWIPE has been optimized to cover the high frequency side of the CMB spectrum with very high sensitivity. Combining its data with STRIP, which covers the low-frequency side with orthogonal technologies, LSPE becomes a powerful mission, with unprecedented sensitivity and efficient control of systematic effects.
In order to reveal B-modes from inflation, LSPE is based on some assumptions, which give to important requirements:

a) *Large-scale*: we need to observe a large sky fraction, because the signature of the effect of the re-ionization and of the inflation (primordial B-modes) are mainly evident at low multipoles $\ell < 80$;

b) *Frequency coverage*: foregrounds dominates the CMB signal at high and low frequencies expecially in polarization. If we want to separate foregrounds from the cosmological signal we have to scan the same part of the sky at different wavelengths and then operate a massive component separation [12, 13, 45];

c) *Control of systematics*: the control of systematics plays an important roles in a CMB polarization experiment. The mitigation of spurious signals can be easier operated with an optimised scanning strategy.

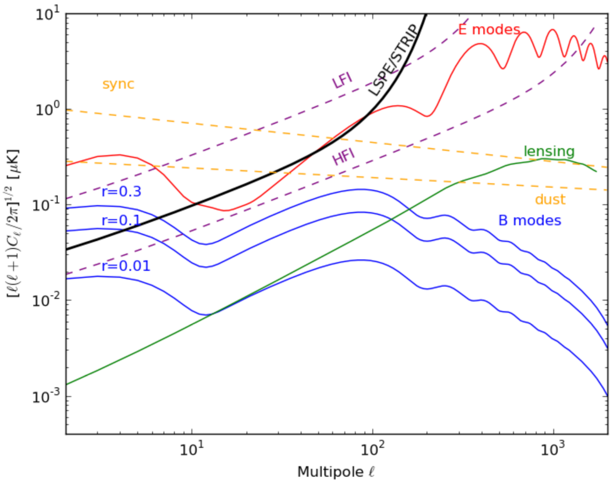

Figure 4.1: *Overall polarized power spectra from CMB (both E and B modes), from galactic foregrounds (synchrotron and dust scaled at 40 GHz) and the expected white-noise sensitivity from LSPE/STRIP compared to both Planck-LFI and Planck-HFI. [18]*

Tab.4.1 shows the level of the polarized angular power spectra of CMB for E-modes (red line) and for the expected amplitude of primordial B-modes for different values of r (blue lines). For example, in violet we show the noise levels of Planck-HFI/LFI instruments and in black the expected noise level for LSPE-STRIP. The green line is the lensing, the blue lines are B-mode signal and the yellow lines corresponds to the polarized foregrounds (synchrotron and dust) that must be mitigated during the data analysis pipeline.

The significant improvement of STRIP with respect to the Planck-LFI data, that have similar frequency range, implies a step forward in our understanding of the microwave sky at large angular scales, where the signature from inflation through the B-modes is higher.

4.1.1 STRIP INSTRUMENT DESIGN

STRIP covers the low frequency with 49 polarimeter modules in Q-band ($\sim 40GHz$) and a small array of 7 modules in W-band ($\sim 90GHz$), see Fig.4.2. It is a ground based telescope that will be placed at Canary islands. The Q-band channel is designed to map the polarized Galactic synchrotron emission, which is dominant in a large fraction of the sky a low frequencies useful for an effective component separation. The W-band array will contribute to the CMB polarized sensitivity in foreground-clean regions and provides a key for systematic effect cross-check thanks to the different technologies adopted by the two (STRIP and SWIPE) instruments.

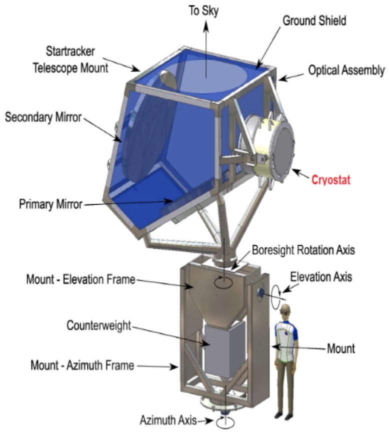

Figure 4.2: *STRIP proposed ground configuration. [20]*

The detectors will be placed in the focal plane of a dual-reflector telescope that provides an angular resolution of about 1.5 degrees. In Fig.4.1 are shown the main characteristics of the instrument compared to Planck-LFI ones.

4.1.2 SWIPE INSTRUMENT DESIGN

SWIPE instrument is a refractive telescope which will detect the polarization of the CMB using TES bolometers, see Fig.4.3. It will fly on a balloon from Svalbard collecting data for about 15 days. In Fig.4.2 are shown the details of the instrument compared to Planck-HFI. The peculiarity of SWIPE will be the presence of a rotating **half wave plate** (HWP) polarization modulator to mitigate the instrumental systematics. HWP can be used to separate beam asymmetries from polarization signals by occasional stepping of the HWP orientation or by continuously rotating it. A HWP allows to [28]: i) mitigate beam, calibration

	PLANCK-LFI			STRIP	
Frequency (GHz)	30	44	70	43	90
FWHM Resolution (arcmin)	0.55	0.47	0.22	1.0	0.5
Sky covverage (%)	100	100	100	18	18
Obs time (months)	30	30	30	0.467	0.467
Bandwidth (%)	4.5	4.1	12.0	7.7	16.2
N_{det}	2	3	6	49	7
Tsky (antenna) (K)	2.068	1.804	1.382	1.822	1.113
Delta Q(U) (μK) on SWIPE beams	3.27	3.95	3.77	1.78	6.68
Improvement factor wrt Planck-HFI				2.2	0.6

Table 4.1: *Main characteristics of the STRIP instrument, compared to the LFI instrument aboard of Planck. [9]*

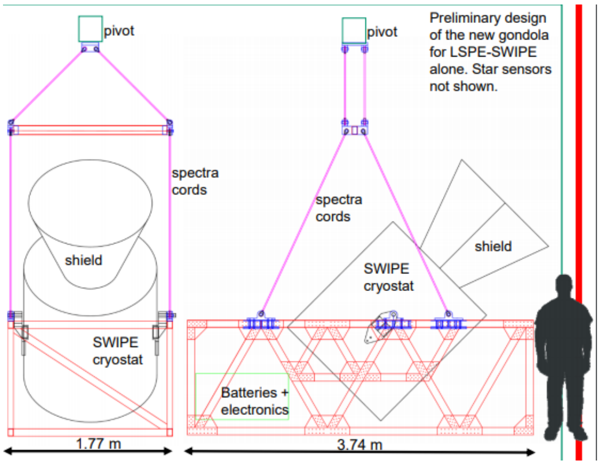

Figure 4.3: *Design of the SWIPE instrument [19].*

and other instrumental systematics; ii) reject the $1/f$ noise at the hardware level, as it moves the polarization signal to high frequencies allowing thus to sample the Stokes parameters Q and U in the white noise regime; iii) achieve a better angle coverage uniformity. Despite these positive points, the HPW can induce systematic effects that are to be studied.

The scanning strategy of this instrument is based on a stepped or spinning HWP. The scanning strategy of SWIPE, shown in Tab.4.4 is described by three parameters: the sky-scan speed, the rotation rate of the HWP and the elevation. The instrument scans the sky by spinning around the local vertical, while keeping the telescope elevation constant for long periods and then changing the elevation by step between 35 and 55 deg. SWIPE will map the sky spinning at $\sim$ 3rpm and moving around the North Pole at a latitude around the 78th parallel North with a constant angular velocity. This scanning strategy will lead to an overall sky coverage of about 33%, which will be sufficient to reconstruct the angular

	PLANCK-HFI						**SWIPE**		
Frequency (GHz)	100	143	217	353	545	857	140	220	240
FWHM Resolution (arcmin)	9	7	6	5	5	5	90	90	90
Sky coverage (%)	100	100	100	100	100	100	30	30	30
Obs time (months)	30	30	30	30	30	30	0.467	0.467	0.467
Bandwidth (%)	33	33	33	33	33	33	33	5	5
N_{det}	8	8	8	8	0	0	110	108	108
Channel NET (μK s^{1/2})	25	31	45	140	//	//	11.05	46.81	97.49
Delta Q(U) (μK) on SWIPE beams	0.27	0.42	0.84	2.6	-	-	0.10	0.43	0.90
Improvement factor wrt Planck-HFI							4.2	1.95	2.92

Table 4.2: *Main characteristics of the SWIPE instrument, compared to the HFI instrument aboard of Planck [9].*

power spectrum down to multipoles of the order of 15.

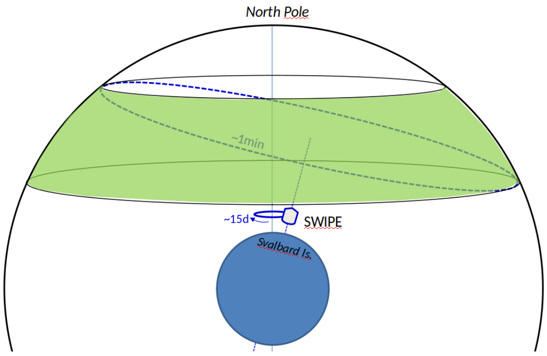

Figure 4.4: *Scanning strategy of SWIPE/LSPE experiment.*

SWIPE will have as first optical element a HWP polarization modulator followed by a 50 cm aperture refractive telescope, a beam splitting polariser, and two symmetric orthogonally-placed focal planes with an number of 110 detectors per frequency. The single focal plane consists of 55 detectors at 140 GHz, 54 detectors at 240 GHz and 54 detectors at 220 GHz, Fig. 4.5. The position of the detectors is designed taking into account the direction of the scanning strategy. Detectors placed on the same projected elevation angle are able to scan the same sky pixels. The response to polarization of the whole focal plane is modulated by a large diameter rotating HWP based on photolithographic technology. These meta-material wave-plates are based on anisotropic metallic grids behaving differently along two orthogonal axes. To achieve a significant number of polarization modulations the HWP should rotate at a rate of many revolutions per second.

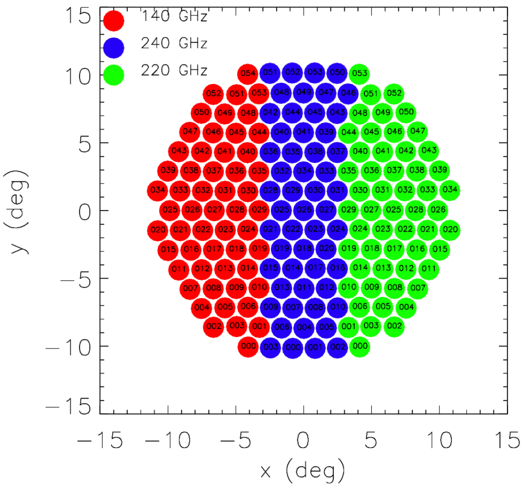

Figure 4.5: *Focal plane of SWIPE, it composed by 55 detectors for 140 GHz (red), 54 detectors for 220 GHz (green) and for 240 GHz (blue).*

4.2 Flight simulator

The scanning strategy of an experiment is an important aspect because allows us to cover efficiently the sky and cover the contamination of systematic effects. So, the first step is to validate a scanning strategy and then to evaluate its impact on systematics mitigation. The core of our simulations is represented by the SWIPE flight simulator, which has the capability to generate Time-Ordered data (TOD) starting from an input map, with CMB and foregrounds.
Inputs to the simulator are:

- Position of the instrument with respect to the Earth surface: longitude and latitude;
- Number of detectors and their frequencies;
- Days of observations;
- HWP configuration;
- Payload rotation speed;
- Noise properties.

The flight simulator simulates the SWIPE scanning strategy along the all mission. At the moment STRIP flight simulator has not been delivered so, in this thesis, we focus our analysis on LSPE-SWIPE optimization. Thee code has also the capability of producing maps thought a internal map-making algorithm. Starting from the inputs described above it provides a TOD, a map of the observed sky, a coverage map with hits per pixel and a block diagonal noise covariance matrix.

4.2.1 Map-making

Another important aspect is represented by the map-making [103]. This process consists in the reconstruction of CMB temperature and polarization maps, starting from TODs and pointing informations, provided by the flight simulator. The flight simulator plus map-making allows us also to simulate systematics and then to propagate those integrated effects on maps and cosmological parameters as well. For the following analysis we used a different map-making tool, that we describe in the following section, instead of MADAM that we used for CORE. In the assumption of only one detector (the final map is a sum over each detector normalised by the number of hits for each pixel) we can define several elements which are the ingredients of the map-making problem:

- N_t, number of time-ordered samples $\sim 6.7 \cdot 10^7$;
- N_p, number of pixels (HEALpix convention);
- A, the pointing matrix of dimension $[N_t,\, N_p]$;
- $\overrightarrow{n}_t$, noise vector, with covariance matrix $N = \left\langle n \cdot n^T \right\rangle$;
- $\overrightarrow{d}_t$, time-ordered data;
- $\overrightarrow{m}_p$, map convolved with the instrumental beam.

A single TOD turns out to satisfy the following relation:

$$\overrightarrow{d}_t = A_{t,p} \cdot \overrightarrow{m}_p + \overrightarrow{n}_t. \tag{4.1}$$

The noise covariance matrix is defined as:

$$N = \left\langle n \cdot n^T \right\rangle, \tag{4.2}$$

where $< ... >$ means that we operate an ensemble mean on infinite noise realization and T is the transposed vector.
The map-making problem consists in finding the solution of Eq.(4.1). The solution has to be linear as we can write:

$$\overrightarrow{s}_p = W \overrightarrow{d}_t, \tag{4.3}$$

where W is the matrix describing the linear relation and $\overrightarrow{s}_p$ is the reconstructed sky map.
We obtain a solution by minimizing the error map:

$$\overrightarrow{s}_p - \overrightarrow{m}_p = [WA - I]\overrightarrow{d}_t + W\overrightarrow{n}_t, \tag{4.4}$$

where I is the identity matrix.
The simplest **map-making method** is the co-addition solution, where the noise component of Eq.(4.1) is neglected. This method performs only noiseless simulation, so we can analyse the effect of predicted systematics without being hidden by noise. So, the corresponding equation is

$$W_{coad} = [A^T A]^{-1} A^T. \tag{4.5}$$

The A^T projects the timeline onto the sky map pixels and the $A^T A$ counts the sample falling in each pixel. Moreover for this method we satisfy the property $W_{coad}A = I$ and minimise the error map variance for the noiseless case.
We can define a more general solution, i.e we can define the noise power spectrum starting from the noise covariance matrix in Eq.(4.2):

$$P(n) = \frac{1}{|(2\pi)^{n_t} N|^{\frac{1}{2}}} e^{-\frac{1}{2}\overrightarrow{n}_t^T N^{-1} \overrightarrow{n}_t}. \tag{4.6}$$

The optimal method called **maximum likelihood solution** is given by $dP/dm = 0$, where:

$$W = (A^T N^{-1} A)^{-1} A^T N^{-1}. \tag{4.7}$$

If N is unknown, we need to make a guess using a noise model. Eq.(4.7) is valid in case of Gaussian noise.
Considering a simple example: an overlap of white noise and $1/f$ noise, with a specific f_{knee}. The noise power spectrum becomes:

$$P(n) = \sigma^2(1 + f_{knee}/f). \tag{4.8}$$

We can evaluate the noise covariance matrix as:

$$N^{-1} = F^{-1}[\Theta^{-1} F(\overrightarrow{d} - A\overrightarrow{m})], \tag{4.9}$$

where F is the Fast Fourier Transformation, F^{-1} is inverse of the Fast Fourier Transformation and Θ is the noise spectral density.
The $\frac{1}{f}$ noise causes the correlation of pixel at large scale in the sky. We need to

use an high-pass filter, in order to reduce the effect of this $\frac{1}{f}$ noise. This approach reduce the cosmological informations at low multipoles, for this reason the flight simulator is provided with an iterative map-making which has the capability of restoring the large part of the signal removed by the filtering. The iterative method can restore more than 80% of lost signal at all multipoles with only 10 iterations [9].

4.3 Template fitting

As we can described above, the component separation is necessary to remove the foreground contaminations from the observed sky. The template fitting we implemented is based on the idea that the channels at frequencies higher and lower than the cosmological ones may be used as templates for dust and synchrotron emissions in polarization.
The template fitting, developed by WMAP team, has been also widely used to build the polarization low-ell likelihood in Planck. Actually it is the only validated method that allow to build an accurate full spectra likelihood (TT, EE, BB, TE, TB, EB) and it is pixel based allowing for testing also non rotational invariant models. In Planck, we used it at $N_{side} = 16$ but for LSPE data we wanted to work at $N_{side} = 64$. At the moment we do not have STRIP realistic simulations so it is not possible to test the template fitting with in synchrotron contaminations. We tested the template fitting in the case of a single foreground: the dust. In the test we used, for the reason in the following, the 140 GHz map as the cosmological channel to be cleaned. We can define the polarization map as:

$$m = \frac{1}{1-\alpha}(m_{140} - \alpha m_X), \tag{4.10}$$

here m is the (Q,U) map, X stands for 220 GHz or 240 GHz channels and α is the scaling coefficient for dust emission that is found by minimizing:

$$\chi^2 = m^T C^{-1} m, \tag{4.11}$$

where C is the signal+noise covariance matrix:

$$C = S(C_\ell) + \frac{1}{(1-\alpha)^2} N_{140} + \frac{\alpha^2}{(1-\alpha)^2} N_X. \tag{4.12}$$

We consider negligible the contribution to the covariance matrices of the error on alpha.

4.4 Angular power spectrum estimator: Cromaster

Cromaster is an implementation of the pseudo-C_ℓ method [54], in particular it allows for both auto- and cross-power spectrum estimation [81].
It is possible decompose a sky map (X) in CMB signal plus noise data:

$$X = S + n \tag{4.13}$$

from that we can define the masked sky pseudo-spectrum as:

$$\widetilde{C}_\ell = \frac{1}{2\ell+1}\sum_{m=-\ell}^{\ell} |a_{\ell m}|^2 = \widetilde{C}_\ell^S + \widetilde{N}_\ell \tag{4.14}$$

The term $\widetilde{C}_\ell^S$ is the pseudo-spectrum of the sky signal and the term $\widetilde{N}_\ell$ is the noise pseudo-spectrum present in the map. We have defined the pseudo-a$_{\ell m}$ as a function of the mask (w) and the spherical harmonics functions of the expansion ($Y_{\ell m}$):

$$\widetilde{a}_{\ell m} = \int d\Omega X(\theta,\phi) w(\theta,\phi) Y^*_{\ell m}(\theta,\phi) \tag{4.15}$$

In order to recover the full sky power spectrum, $\widehat{C}_\ell$, cromaster uses the estimator:

$$\widehat{C}_\ell = \sum_{\ell'} K_{\ell\ell'}(\widetilde{C}_{\ell'} + \widetilde{N}_{\ell'}) \tag{4.16}$$

where $K_{\ell\ell'}$ is the mode-mode coupling kernel and it is a geometrical correction that accounts for the loss of orthonormality of the spherical harmonic functions in the cut sky. For an isotropic sky signal, that is a realization of a theoretical power spectrum, we can define $\left\langle \widehat{C}_\ell \right\rangle = C_\ell$.
It is possible define the error bars for pseudo-C_ℓ methods for a masked sky as:

$$\Delta\widehat{C}_\ell = \sqrt{\frac{2}{2\ell+1} f_{sky}\left(C_\ell + N_\ell\right)} \tag{4.17}$$

where f_{sky} is the effective fraction of the sky used for the analysis which accounts for the weighting scheme of the pixels.
A more accurate approach to associate an error bar to the estimated APS is to build a covariance matrix, that in this case is an $\ell_{max} \times \ell_{max}$ matrix, where ℓ_{max} is the maximum multipole. The elements of the covariance matrix are defined as:

$$Cov(\widehat{C}_\ell \widehat{C}_{\ell'}) = \left\langle \left(\widehat{C}_\ell - < \widehat{C}_\ell >\right) \left(\widehat{C}_{\ell'} - < \widehat{C}_{\ell'} >\right) \right\rangle_{MC} \tag{4.18}$$

The error bars can be approximated, at the first order, as the elements of the diagonal of the matrix. The approximation is corrected if the off-diagonal elements are orders of magnitude lower than diagonal elements. In order to estimate the covariance matrix off-diagonal elements we need a large number of simulations.

4.5 Validation of SWIPE simulator and optimization of scanning strategy

The validation of the SWIPE scanning strategy and data pipeline are important to further optimize the instrument characteristics in view of a better performance in polarization. The parameters that we selected as input to SWIPE simulator to produce maps are shown in Tab.4.3. As an optimization of the scanning strategy we tested the performances of using a stepping or a spinning HWP. The

Parameters	**Value**
Latitude	78.2 $°N$
Longitude	15°.6
Initial elevation	35°
Elevation range	10°
Frequencies	140, 220, 240 GHz
Number of detectors	110, 108, 108
Mission length	14 days
Including $1/f$ noise	$f_{knee} = 20$MHz;

Table 4.3: *The flight parameters that we used for the simulation.*

parameters that we took into account are shown in Tab.4.4. For all the following

Motion HWP	**Stepping**	**Spinning**
Rotation speed	3.0 rpm	0.125 rpm
ω_{HWP}	20 step per hour	/
Spin HWP	/	1.01

Table 4.4: *Characteristics of the simulated stepping and spinning HWP.*

analysis we generated maps at Healpix resolution parameter, N_{side}, equal to 64 and we analysed all the SWIPE frequencies 140, 220 and 240 GHz. We gave to the simulator an artificial CMB sky with r=0.03, with dust contamination simulated following [21] with a constant β spectral index. For the map-making we choose an iteration equal to 50.
We compared two cases of HWP: stepping, where the HWP makes 20 step per hour and spinning where the plate has a continuous rotation speed of 1.01 rpm. As a first preliminary test, we considered the output maps of the two different cases Fig. 4.6 In order to better appreciate the differences between the outputs

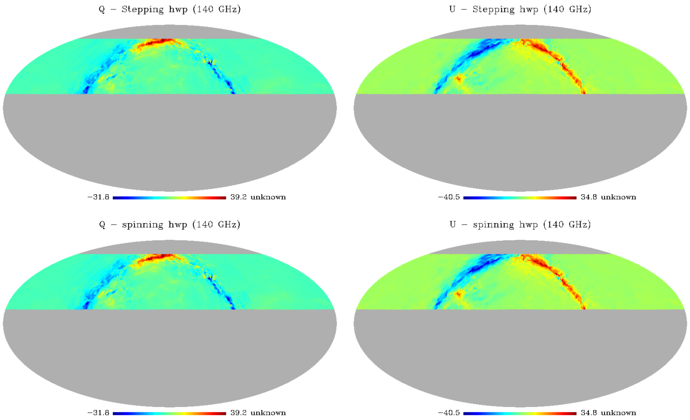

Figure 4.6: *Comparison between Q and U output maps for 140 GHz for the stepping case (top line) and the spinning case (bottom line). All the maps are in equatorial coordinates.*

of the simulator in the two different configurations we show the maps of the output-input for Q and U at frequencies of 140 GHz, Fig.4.7. Here we can appreciate important differences between the two cases with larger residuals for the stepping case.

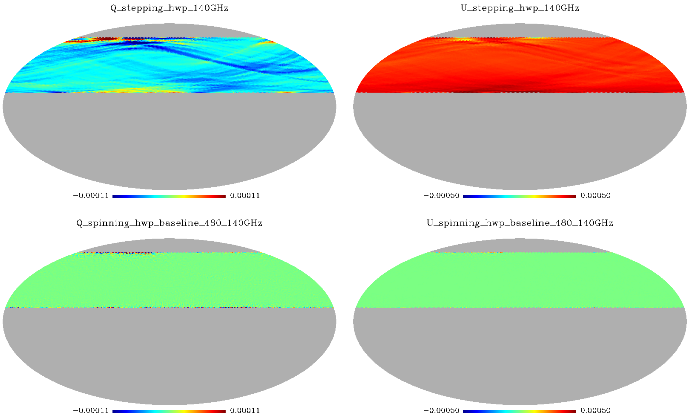

Figure 4.7: *The maps of the output-input maps for Q and U for frequencies 140 GHz for both stepping (top line) and spinning HWP (bottom line) in equatorial coordinates.*

In Fig.4.8 we show the histograms for the 3x3 noise covariance matrices for the frequencies of SWIPE at 140 GHz (green line), 220 GHz (blue line) and 240 GHz (red line). We compare the stepping HWP case (first and third row) with the spinning HWP one (second and fourth row) for the temperature and polarization components. We find that for both stepping and spinning cases the covariances TT, QQ and UU are very similar, while differences are seen in the TP correlation. In particular, the spinning case is more efficient in limiting the correlations TQ and TU but the correlation QU is greater with respect to the stepping case. We also noticed that, there are few very large values probably due to poor observation of the pixels at the borders of the scanning strategy giving high noise covariance values. To mitigate this problem, we removed those pixels in the component separation analysis.
We consider, also histograms of the reciprocal condition numbers (RCN) of the noise covariance matrix. They are the ratio between the lowest and the largest eigenvalue of the 3x3 noise covariance matrix for each pixel. We show the results in Fig.4.9, where we compare again the stepping with respect to the spinning case. 140 GHz is the green line, 220 GHz is the blue line and 240 GHz is the red line. LSPE is a good candidate to solve the polarization because has very high RCN allowing for a very good reconstruction of the polarization amplitude for each pixel. From this simple test we can conclude that the difference between the stepping and the spinning cases are smaller. However looking at output-input maps it seems that the spinning HWP case is better.
We also, tested the optimization of the map-making baseline. We simulate the spinning HWP with different baseline of the map-making: 60 s, 480 s and 1440

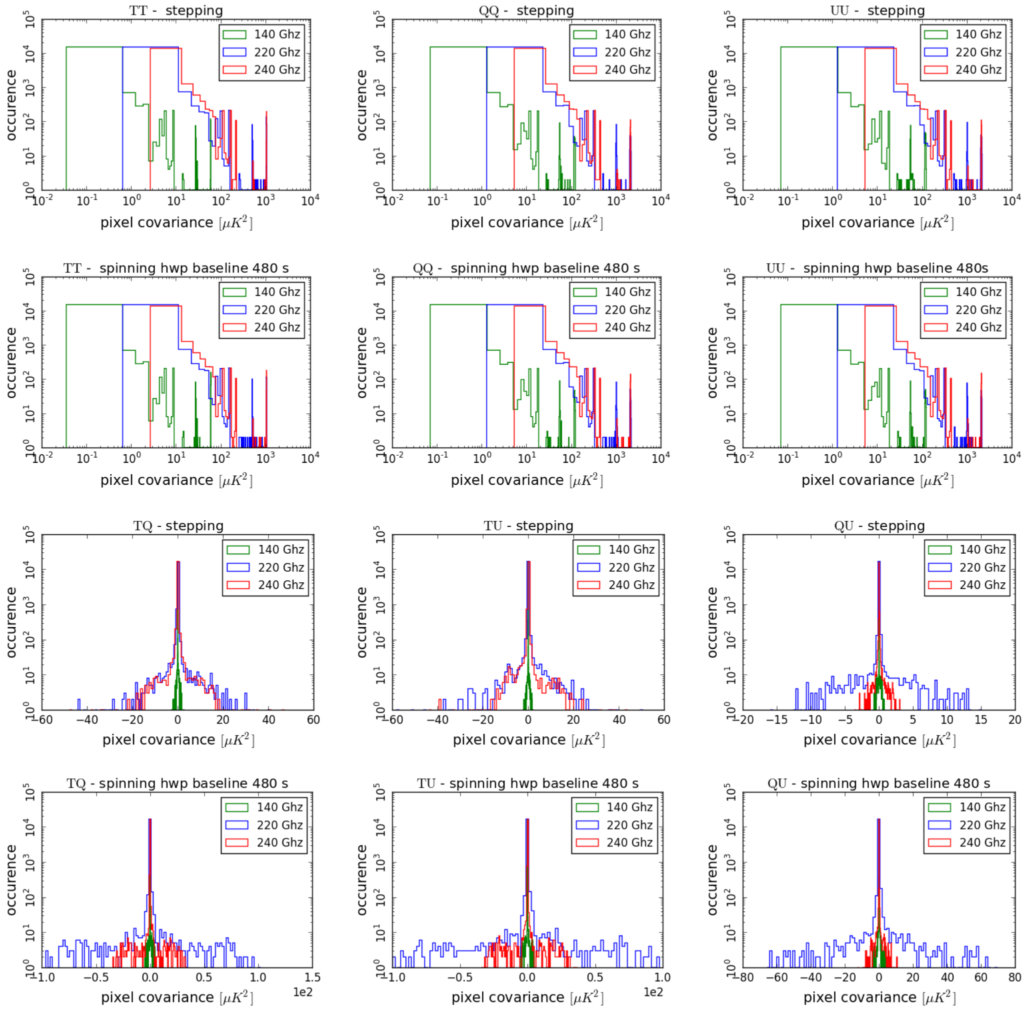

Figure 4.8: *Histograms of the 3x3 noise covariance matrices for stepping (first and third row) and spinning HWP (second and fourth row) for all the frequencies 140 (green line), 220 (blue line) and 240 GHz (red line).*

s. To better appreciate the differences between the different baseline of the map-making we show the maps of the output-input for Q and U at frequencies of 140 GHz, Fig.4.10. Here we can appreciate important differences between the three baseline that we choose, the lower level of contamination is present in the baseline case 480 s. We also check that histograms of the 3x3 covariance matrices and the RCN and they show very similar results. From these tests we find that the best case is spinning HWP with baseline 480 s. For this reason we consider this as the principal case for the following analysis.

As a last test, to validate the SWIPE scanning strategy, we investigated the

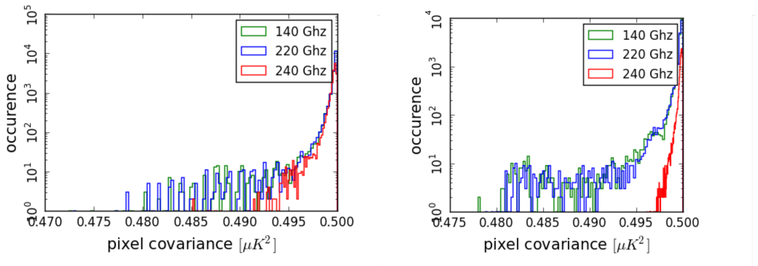

Figure 4.9: *Histograms of the inverse condition number for the cases: stepping HWP (left side) and spinning HWP (right side). The green lines of the histograms correspond to the 140 GHz channel, the blue lines 220 GHz channel, and the red lines 240 GHz channel.*

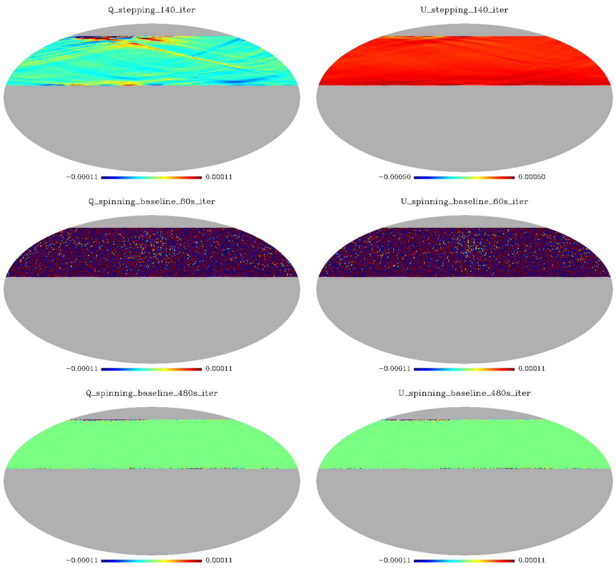

Figure 4.10: *The maps of the output-input maps for Q and U for frequencies 140 GHz for spinning HWP in equatorial coordinates for different baseline of map-making: 60 s (top panels), 480 s (middle panels) and 1440 s (bottom panels).*

impact of $1/f$ noise on observed maps. In order to do that, starting from the best case that we described above, we generated noise maps with $1/f$ contamination. We compared their mean APS with the average APS obtained from 100 white noise maps (no $1/f$). In Fig.4.11 we show the APS for the polarization EE (on the left) and BB (on the right), for the noise maps with $1/f$ effect (green line) with the associate 1σ dispersion (green shadow) and for the white noise maps (cyan line) with the associate dispersion (cyan shadow). From these results

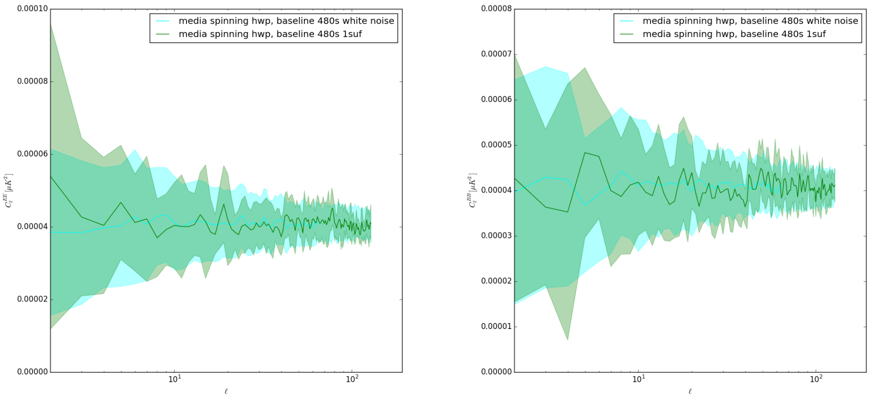

Figure 4.11: *Average polarization angular power spectra of the noise maps at 140 GHz with (green) and without (cyan) $1/f$ noise contamination. Shaded regions are 1σ dispersion of the MC. On the left EE and on the right BB.*

we can conclude that there are no significant differences between the two cases considered, confirming that the spinning HWP is able to efficiently remove the $1/f$ noise contamination.

From these results we obtained that the spinning case is the best for our analysis. So from here on we considered only the spinning case.

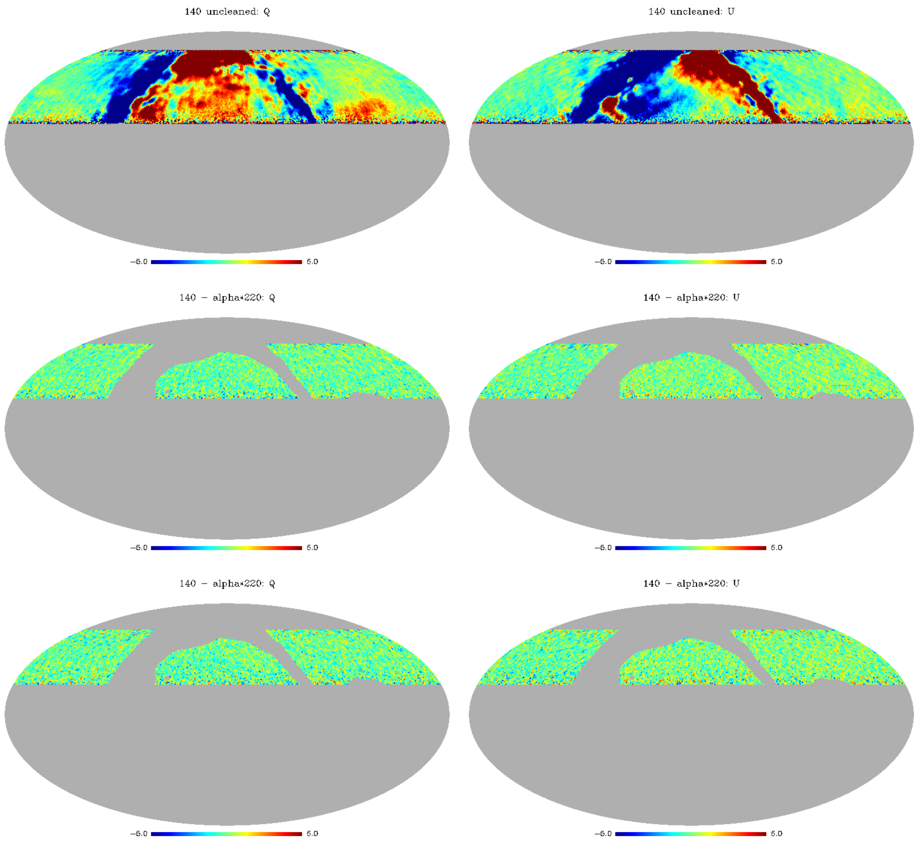

Figure 4.12: *In the top line the 140 GHz Q and U input maps, in the central and bottom lines the map cleaned with the 220 GHz and 240 GHz channels. The colour scales are the same going from* -5.0 *to* $5.0\mu K$.

4.6 Preliminary results of the template fitting technique

To test and validate the template fitting methodology we did several test. We analysed the 140 GHz, 220 GHz and 240 GHz channels with a $N_side = 64$, FWHM = 110' and considered a CMB maps from Planck best fit 2018 fiducial model with r=0.03. Moreover we consider the the CMB plus dust maps passed through the LSPE scanning strategy simulator and used a mask that cover the border pixels and the galactic plane. In the component separation APS extraction we consider a mask, that has been optimize to reduce the noise in the analysis. It masks all the unobserved pixels, the galactic plane where we used the polarization mask used in Planck-LFI low ℓ likelihood and the pixels at the borders of the observed region, that has described in the previous sections, show higher noise value. We tried to clean the 140 GHz channel with both 220 GHz and 240 GHz channels with the template fitting code, that we implemented and we used Cromaster code to extract the APS of the cleaned maps. In this way we are able to compare the APS before and after the component separation process and see the effect of the cleaning. Fig. 4.12 show the input Q an U 140 GHz with dust contamination map (top line) and the cleaned map with 220 GHz and 240 GHz channels respectively in the second and third line. The colour scale is set the same for all the maps, in order to emphasis the effect of the cleaning. In the cleaned maps we don't see any more any large scale contamination. In order to understand if the template fitting is properly working we firstly compare the scaling factors, α, estimated by our code with the theoretical value. In Fig. 4.13 we show the scaling factor obtained cleaning the 140 GHz with the 220 GHz (left panel) and the 240 GHz (right panel). From these results we can conclude that we are able to clean the maps in a very good way, because the α that we obtain is in agreement with the theoretical one at 1σ level.

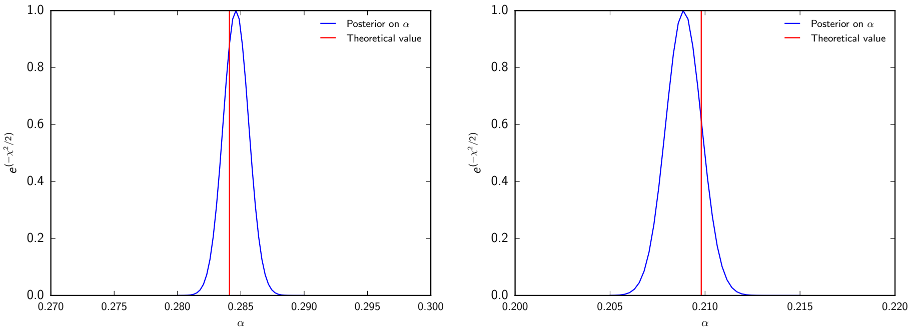

Figure 4.13: *On the left the posterior of α with 220 GHz and on the right with 240 GHz. In blue there are the posterior of α, in red the theoretical value.*

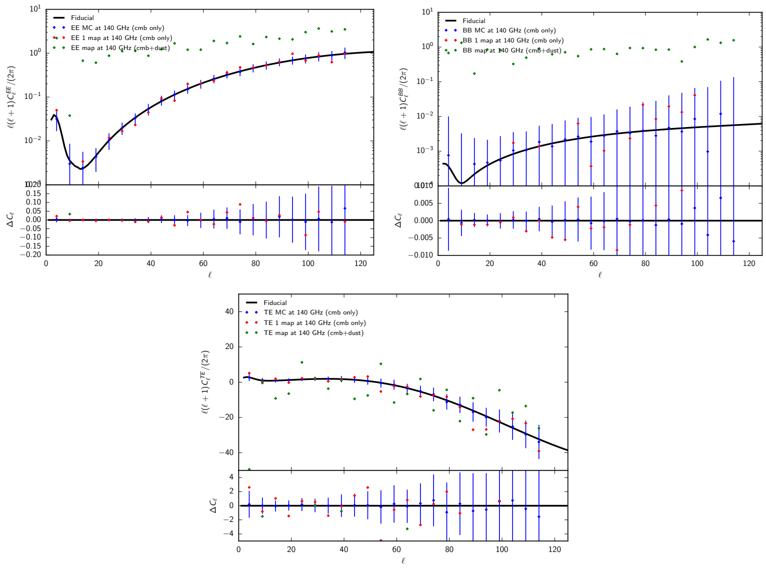

Figure 4.14: *From top left to right bottom the APS of the input 140 GHz map for: EE, BB and TE. The black line is Planck best fit 2018 fiducial model, the dots are: MC CMB plus noise (blue), single map with only CMB (red) and the same CMB plus dust at 140 GHz. Lower panels show the residuals with respect to the fiducial.*

In Fig.4.14 we show the APS of the input map at 140 GHz channel (blue dots), we show the MC (100 realizations) with CMB plus noise, a single map with only CMB realization for reference (red dots) and the same CMB with dust contamination (green dots). It is evident the effect of contamination in polarization.

In Fig. 4.15 we show the preliminary results of the component separation cleaning 140 GHz with the 220 GHz channel. We show in black the Planck best fit 2018 fiducial model and in blue, red and green a MC of the CMB plus noise and the cleaned map respectively. The APS of the cleaned maps is now fully compatible with the MC of the CMB plus noise only map giving us the proof that our template fitting method efficiently removes the contaminations. APS of the CMB map EE, BB and TE and the once of the cleaned one are very similar. In Fig. 4.16 we show the same that we show in Fig.4.15 but using the 240 GHz channel. Results are very similar with the previous case.

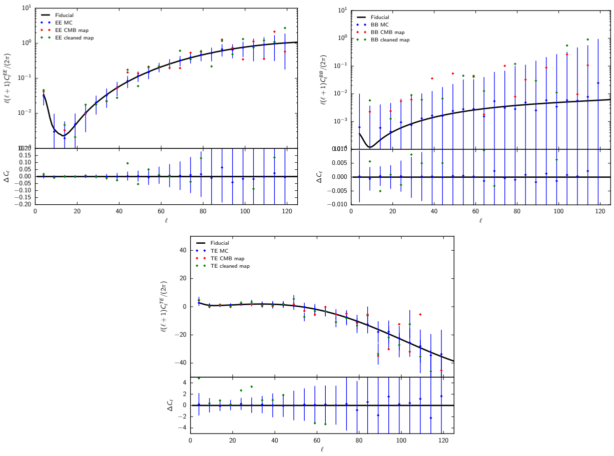

Figure 4.15: *APS for the 140 GHz map cleaned with the 220 GHz channel. From top left to bottom right EE, BB and TE. The black line corresponds to the Planck best fit 2018 fiducial model, the dots correspond to MC (blue), single CMB map (red) for reference and the cleaned map (green).*

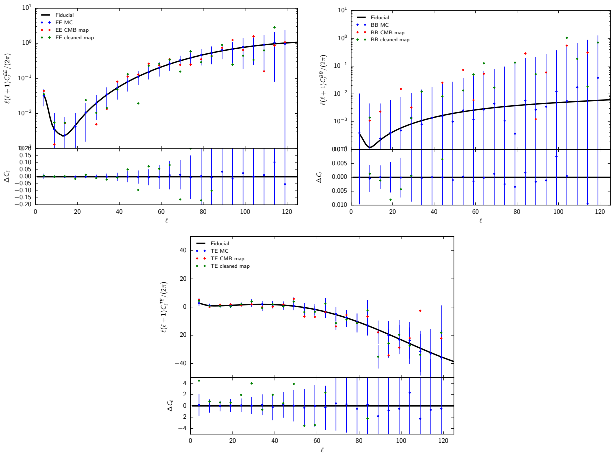

Figure 4.16: *APS for the 140 GHz map cleaned with the 240 GHz channel. From top left to bottom right EE, BB and TE. The black line corresponds to the Planck best fit 2018 fiducial model, the dots correspond to MC (blue), single CMB map (red) for reference and the cleaned map (green).*

4.7 Future prospectives

As we can see in the previous section, the validation and optimization process of the template fitting give us some good results. We are able to clean the maps in a very good way, because the scaling factor that we obtain is very close to the theoretical value. Looking to the APS of the map cleaned, it is evident the effect of contamination in polarization. In fact, the template fitting induce a high noise in polarization that cover the CMB signal especially in BB.

So we need to optimize the template fitting technique and in order to do that a possible choice is test and validate the template fitting method using the 270 GHz channel instead of 240 GHz. Because the photon noise at 270 GHz is lower and reduce the noise in polarization after cleaning. Another step is to combine the 140 GHz with the 220 GHz maps both clean by the 240 GHz channel, in order to see the impact of the noise. Furthermore, a final figure of merit will be the estimation of the cosmological parameters from the cleaned maps to propagate the uncertainties and find the tensor-to-scalar ratio.

Conclusions

In this thesis I focused on two future CMB polarization experiments, the proposed CORE satellite mission and the ground-based/balloon-borne experiment LSPE. The main results of this thesis is the optimization of the scanning strategy parameters for both experiments. In the case of LSPE, I have also discussed the removal of foreground contamination to achieve better quality CMB polarization data.

In the case of CORE, I used the TOAST code to simulate the scanning strategy of the satellite and I explored in detail the properties of the CORE noise maps and the impact of $1/f$ noise, focusing on a pair of detectors at 145 GHz to produce (I, Q, U) maps, at positions in the centre and at the edges of the focal plane. I have also attempted to optimize the scanning strategy parameters and forecast contamination from $1/f$ noise in BB measurements. I investigated the impact of systematic effects that we expect to affect the observations. I used the TOAST simulation pipeline to generate timelines of realistic instrumental noise with $1/f$ contamination. Moreover, I used the flexible generalized destriping code MADAM to minimize this $1/f$ contamination, for the specific CORE set-up and scanning strategy case. For all the cases analysed in this thesis I find the best set-up that achieves full sky coverage and is able to cleanly separate the Stokes parameters. I used, as figure of merit, the 3x3 pixel noise covariance matrices, checking that they are well-conditioned. In the absence of an active hardware modulator such as an half-wave plate, the CORE instrument can only count on the satellite scanning strategy to modulate the polarization signal. Moreover, I demonstrated how the residual QU couplings are non negligible and need to be accounted for during the analysis. In this work I have also attempted to optimize the scanning strategy parameters: in particular precession and spin angles. I found that the advantage is minimal within a range of angles compatible with

reasonable assumptions on the satellite design and operational constraints. The CORE map-making obtains excellent levels of suppression of the auto-correlated noise component ($1/f$), thanks to a very well interconnected scanning strategy. I find that for a detector knee frequency of the order of 10 mHz, the residual correlation in the noise maps can be neglected. Finally, I forecasted the impact of $1/f$ noise in the measurement of the BB angular power spectra (APS) finding that, for $f_k < 10$ mHz, the results are indistinguishable from pure white noise maps.
The validation of the LSPE-SWIPE scanning strategy is a crucial point, exactly as for the CORE satellite, to further optimize the instrument characteristics in view of better performance in polarization. I used a SWIPE flight simulator code to simulate the scanning strategy of the balloon and explored the properties of the noise maps and the impact of $1/f$ noise. We focused on all the three channels of the instrument: 140 GHz, 220 GHz and 240 GHz. In particular, I tested different performances of the half-wave plate: a stepping HWP, which makes 20 steps per hour, and a spinning HWP, which has a continuous rotation speed of 1.01 rpm. From the difference of Q and U maps I assessed the respective performances of the stepping and spinning HWP, finding larger residuals for the first case. In addition, I analysed the histograms of the 3x3 covariance matrices, finding that both for stepping and spinning cases the covariances TT, QQ and UU are very similar, while some differences are present in the cross-correlations. Another figure of merit that I analysed is the reciprocal condition number, RCN. I have found that the RCN is very close to the ideal value of 0.5 thanks to the use of an HWP. This means that SWIPE is able to reconstruct polarization for each pixel in an optimal way. Therefore, the spinning HWP is the best case scenario for SWIPE.

In order to have a complete comprehension of the map-making algorithm I tested the differences in the reconstructed maps using three different baselines: 60 s , 480 s and 1440 s. The lower level of contamination is shown in the 480 s case, where I investigated the impact of $1/f$ noise on the observed maps finding that it is negligible.

After the validation of the SWIPE flight simulator, I implemented a template fitting code for component separation. I focused on removing the dust contamination from the 140 GHz channel using both the 220 GHz and 240 GHz channels as templates. By comparing the APS before and after component separation, I benchmark the results obtained from our template fitting method with theoretical expectations, finding that they are in good agreement.

As a final test, I compared the APS extracted from the 140 GHz maps cleaned with the 220 GHz maps to the simulated inputs, employing Monte Carlo realizations of the CMB plus noise maps. Aim of this comparison is to prove that our template fitting method efficiently removes contamination. However, we notice that the template fitting procedure induces higher noise in polarization. I obtained a similar result using the 240 GHz channel as input.

It is evident that there are margins for further improvements. For example, using a 270 GHz channel (not currently in the setup) instead of 240 GHz. The reason for this choice is that the photon noise at 270 GHz is not much higher then 240 GHz, but the former is significantly farther apart in frequency from 140 GHz. This would reduce the noise in polarization during the cleaning process. Therefore the results of my thesis show that this new channel should be considered. Another possible step could be combining the 140 GHz and the 220 GHz maps both cleaned with the 240 GHz channel, in order to limit the impact of the noise.

The results of this thesis set a remarkable confirmation that the simulation pipeline for a next generation of space/balloon born are powerful tool to aid the design of an experiment. Thanks to my simulations we are able to choose the best configuration of the instruments, in particular for scanning strategy, and give constrain about the future observations of the CMB polarization.

Bibliography

[1] R Adam, PAR Ade, N Aghanim, MIR Alves, M Arnaud, M Ashdown, J Aumont, C Baccigalupi, AJ Banday, RB Barreiro, et al. Planck 2015 results-x. diffuse component separation: Foreground maps. *Astronomy & Astrophysics*, 594:A10, 2016.

[2] R. Adam et al. Planck 2015 results. i. overview of products and scientific results. *Astron. Astrophys.*, 594:A1, 2016.

[3] P. A. R. Ade et al. Improved Constraints on Cosmology and Foregrounds from BICEP2 and Keck Array Cosmic Microwave Background Data with Inclusion of 95 GHz Band. *Phys. Rev. Lett.*, 116:031302, 2016.

[4] P. A. R. Ade et al. Planck 2015 results. XIII. Cosmological parameters. *Astron. Astrophys.*, 594:A13, 2016.

[5] PAR Ade, N Aghanim, M Arnaud, M Ashdown, J Aumont, C Baccigalupi, AJ Banday, RB Barreiro, JG Bartlett, N Bartolo, et al. Planck 2015 results-xii. full focal plane simulations. *Astronomy & Astrophysics*, 594:A12, 2016.

[6] N Aghanim, C Armitage-Caplan, M Arnaud, M Ashdown, F Atrio-Barandela, J Aumont, C Baccigalupi, AJ Banday, RB Barreiro, E Battaner, et al. Planck 2013 results. v. lfi calibration. *Astronomy & Astrophysics*, 571:A5, 2014.

[7] N Aghanim, C Armitage-Caplan, M Arnaud, M Ashdown, F Atrio-Barandela, J Aumont, C Baccigalupi, Anthony J Banday, RB Barreiro, E Battaner, et al. Planck 2013 results. iii. lfi systematic uncertainties. *Astronomy & Astrophysics*, 571:A3, 2014.

[8] N. Aghanim et al. Planck 2018 results. VI. Cosmological parameters. 2018.

[9] S. Aiola et al. The Large-Scale Polarization Explorer (LSPE). *Proc. SPIE Int. Soc. Opt. Eng.*, 8446:84467A, 2012.

[10] Y. Akrami et al. Planck 2018 results. i. overview and the cosmological legacy of planck. 2018.

[11] Ralph A Alpher, Hans Bethe, and George Gamow. The origin of chemical elements. *Physical Review*, 73(7):803, 1948.

[12] Charmaine Armitage-Caplan, Joanna Dunkley, Hans Kristian Eriksen, and Clive Dickinson. Large-scale polarized foreground component separation for planck. *Monthly Notices of the Royal Astronomical Society*, 418(3):1498–1510, 2011.

[13] Charmaine Armitage-Caplan, Joanna Dunkley, Hans Kristian Eriksen, and Clive Dickinson. Impact on the tensor-to-scalar ratio of incorrect galactic foreground modelling. *Monthly Notices of the Royal Astronomical Society*, 424(3):1914–1924, 2012.

[14] Carlo Baccigalupi. Cosmic microwave background polarisation: foreground contrast and component separation. *New Astronomy Reviews*, 47(11-12):1127–1134, 2003.

[15] Daniel Baumann. Tasi lectures on inflation. *arXiv preprint arXiv:0907.5424*, 2009.

[16] EJ Baxter, R Keisler, S Dodelson, KA Aird, SW Allen, MLN Ashby, M Bautz, M Bayliss, BA Benson, LE Bleem, et al. A measurement of gravitational lensing of the cosmic microwave background by galaxy clusters using data from the south pole telescope. *The Astrophysical Journal*, 806(2):247, 2015.

[17] CL Bennett, D Larson, JL Weiland, N Jarosik, G Hinshaw, N Odegard, KM Smith, RS Hill, B Gold, M Halpern, et al. Nine-year wilkinson microwave anisotropy probe (wmap) observations: final maps and results. *The Astrophysical Journal Supplement Series*, 208(2):20, 2013.

[18] M Bersanelli, A Mennella, G Morgante, M Zannoni, G Addamo, A Baschirotto, P Battaglia, A Baù, B Cappellini, F Cavaliere, et al. A coherent polarimeter array for the large scale polarization explorer (lspe) balloon

experiment. In *Ground-based and Airborne Instrumentation for Astronomy IV*, volume 8446, page 84467C. International Society for Optics and Photonics, 2012.

[19] Prof. Marco Bersanelli. Lspe/strip status. *SWIPE: Overview, meeting generale lspe Bologna*, 07 July 2017.

[20] Prof. Marco Bersanelli. Lspe/strip status. *Meeting LSPE Milano*, 10 July 2017.

[21] A Bonaldi, S Ricciardi, and ML Brown. Foreground removal requirements for measuring large-scale cmb b modes in light of bicep2. *Monthly Notices of the Royal Astronomical Society*, 444(2):1034–1040, 2014.

[22] FR Bouchet and R Gispert. New astronony, 4, 443. *arXiv preprint astro-ph/9903176*, 1999.

[23] FR Bouchet, L Pagano, R Stompor, P Ferreira, S Galli, M Kunz, S Basak, S Matarrese, T Peacocke, F Finelli, et al. Core: Cosmic origins explorer-a white paper. 2015.

[24] FR Bouchet, S Prunet, and Shiv K Sethi. Multifrequency wiener filtering of cosmic microwave background data with polarization. *Monthly Notices of the Royal Astronomical Society*, 302(4):663–676, 1999.

[25] Harvey R. Brown and James Read. Clarifying possible misconceptions in the foundations of general relativity. *Am. J. Phys.*, 84:327, 2016.

[26] Sean Bryan. Half-wave plates for the spider cosmic microwave background polarimeter. *arXiv preprint arXiv:1402.2591*, 2014.

[27] C. Burigana et al. Exploring cosmic origins with CORE: effects of observer peculiar motion. *JCAP*, 1804(04):021, 2018.

[28] Alessandro Buzzelli, Giancarlo de Gasperis, Paolo de Bernardis, Silvia Masi, and Nicola Vittorio. Optimization of the half wave plate configuration for the lspe-swipe experiment. In *Journal of Physics: Conference Series*, volume 841, page 012001. IOP Publishing, 2017.

[29] Paolo Cabella and Marc Kamionkowski. Theory of cosmic microwave background polarization. In *International School of Gravitation and Cosmology: The Polarization of the Cosmic Microwave Background Rome, Italy, September 6-11, 2003*, 2004.

[30] Sean M Carroll. Lecture notes on general relativity. *arXiv preprint gr-qc/9712019*, 1997.

[31] F Couchot, J Delabrouille, J Kaplan, and Benoît Revenu. Optimised polarimeter configurations for measuring the stokes parameters of the cosmic microwave background radiation. *Astronomy and Astrophysics Supplement Series*, 135(3):579–584, 1999.

[32] RD Davies, RA Watson, and CM Gutierrez. Galactic synchrotron emission at high frequencies. *Monthly Notices of the Royal Astronomical Society*, 278(4):925–939, 1996.

[33] P De Bernardis, PAR Ade, JJ Bock, JR Bond, J Borrill, A Boscaleri, K Coble, CR Contaldi, BP Crill, G De Troia, et al. Multiple peaks in the angular power spectrum of the cosmic microwave background: Significance and consequences for cosmology. *The Astrophysical Journal*, 564(2):559, 2002.

[34] P De Bernardis, S Aiola, G Amico, E Battistelli, A Coppolecchia, A Cruciani, A D'Addabbo, G D'Alessandro, S De Gregori, M De Petris, et al. Swipe: a bolometric polarimeter for the large-scale polarization explorer. In *Millimeter, Submillimeter, and Far-Infrared Detectors and Instrumentation for Astronomy VI*, volume 8452, page 84523F. International Society for Optics and Photonics, 2012.

[35] P. de Bernardis et al. Exploring cosmic origins with core: The instrument. *JCAP*, 1804(04):015, 2018.

[36] G. De Zotti et al. Exploring cosmic origins with CORE: Extragalactic sources in cosmic microwave background maps. *JCAP*, 1804(04):020, 2018.

[37] J. Delabrouille et al. Exploring cosmic origins with core: Survey requirements and mission design. *JCAP*, 1804(04):014, 2018.

[38] J Delabrouille, G Patanchon, and E Audit. Separation of instrumental and astrophysical foregrounds for mapping cosmic microwave background anisotropies. *Monthly Notices of the Royal Astronomical Society*, 330(4):807–816, 2002.

[39] Jacques Delabrouille, J-F Cardoso, M Le Jeune, M Betoule, G Fay, and F Guilloux. A full sky, low foreground, high resolution cmb map from wmap. *Astronomy & Astrophysics*, 493(3):835–857, 2009.

[40] Robert H Dicke, P James E Peebles, Peter G Roll, and David T Wilkinson. Cosmic black-body radiation. *The Astrophysical Journal*, 142:414–419, 1965.

[41] Clive Dickinson. Cmb foregrounds-a brief review. *arXiv preprint arXiv:1606.03606*, 2016.

[42] Clive Dickinson, Richard A Battye, Pedro Carreira, Kieran Cleary, Rod D Davies, Richard J Davis, Ricardo Genova-Santos, Keith Grainge, Carlos M Gutiérrez, Yaser A Hafez, et al. High-sensitivity measurements of the cosmic microwave background power spectrum with the extended very small array. *Monthly Notices of the Royal Astronomical Society*, 353(3):732–746, 2004.

[43] Scott Dodelson. *Modern cosmology*. Academic press, 2003.

[44] BT Draine and A Lazarian. Electric dipole radiation from spinning dust grains. *The Astrophysical Journal*, 508(1):157, 1998.

[45] J Dunkley, A Amblard, C Baccigalupi, M Betoule, D Chuss, A Cooray, J Delabrouille, C Dickinson, G Dobler, J Dotson, et al. Prospects for polarized foreground removal. In *AIP Conference Proceedings*, volume 1141, pages 222–264. AIP, 2009.

[46] Loretta Dunne and Stephen A Eales. The scuba local universe galaxy survey–ii. 450-μm data: evidence for cold dust in bright iras galaxies. *Monthly Notices of the Royal Astronomical Society*, 327(3):697–714, 2001.

[47] Fabio Finelli et al. Exploring cosmic origins with CORE: Inflation. *JCAP*, 1804:016, 2018.

[48] DJ Fixsen, ES Cheng, DA Cottingham, RE Eplee Jr, RB Isaacman, JC Mather, SS Meyer, PD Noerdlinger, RA Shafer, R Weiss, et al. Cosmic microwave background dipole spectrum measured by the cobe firas instrument. *The Astrophysical Journal*, 420:445–449, 1994.

[49] DJ Fixsen, ES Cheng, JM Gales, John C Mather, RA Shafer, and EL Wright. The cosmic microwave background spectrum from the full cobe* firas data set. *The Astrophysical Journal*, 473(2):576, 1996.

[50] George Gamow. Expanding universe and the origin of elements. *Physical Review*, 70(7-8):572, 1946.

[51] Maurizio Gasperini. *Lezioni di cosmologia teorica.* Springer Science & Business Media, 2012.

[52] NW Halverson, EM Leitch, C Pryke, J Kovac, JE Carlstrom, WL Holzapfel, M Dragovan, JK Cartwright, BS Mason, S Padin, et al. Degree angular scale interferometer first results: a measurement of the cosmic microwave background angular power spectrum. *The Astrophysical Journal*, 568(1):38, 2002.

[53] Shaul Hanany, Johannes Hubmayr, Bradley R Johnson, Tomotake Matsumura, Paul Oxley, and Matthew Thibodeau. Millimeter-wave achromatic half-wave plate. *Applied optics*, 44(22):4666–4670, 2005.

[54] Eric Hivon, Krzysztof M Górski, C Barth Netterfield, Brendan P Crill, Simon Prunet, and Frode Hansen. Master of the cosmic microwave background anisotropy power spectrum: a fast method for statistical analysis of large and complex cosmic microwave background data sets. *The Astrophysical Journal*, 567(1):2, 2002.

[55] MP Hobson, AW Jones, AN Lasenby, and FR Bouchet. Foreground separation methods for satellite observations of the cosmic microwave background. *Monthly Notices of the Royal Astronomical Society*, 300(1):1–29, 1998.

[56] Wayne Hu. Concepts in cmb anisotropy formation. In *The Universe at High-z, Large-Scale Structure and the Cosmic Microwave Background*, pages 207–239. Springer, 1996.

[57] Wayne Hu. Lecture notes on cmb theory: from nucleosynthesis to recombination. *arXiv preprint arXiv:0802.3688*, 2008.

[58] J Kaplan and J Delabrouille. Astrophysical polarized backgrounds, eds. s. cecchini, s. cortiglioni, r. sault & c. sbarra. In *AIP Conf. Proc*, volume 609, page 209, 2002.

[59] JF Keating, PJ O'brien, PA Blachut, RN Meek, and HM Broekhuyse. Locking intramedullary nailing with and without reaming for open fractures of the tibial shaft: a prospective, randomized study. *JBJS*, 79(3):334–341, 1997.

[60] Elina Keihänen, Reijo Keskitalo, Hannu Kurki-Suonio, Torsti Poutanen, and A-S Sirviö. Making cosmic microwave background temperature and polarization maps with madam. *Astronomy & Astrophysics*, 510:A57, 2010.

[61] Elina Keihänen, Hannu Kurki-Suonio, and Torsti Poutanen. Madam-a map-making method for cmb experiments. *Monthly Notices of the Royal Astronomical Society*, 360(1):390–400, 2005.

[62] William H Kinney. Tasi lectures on inflation. *arXiv preprint arXiv:0902.1529*, 2009.

[63] Lev Davidovich Landau. *The classical theory of fields, Volume 2.* Elsevier, 2013.

[64] A Lange, P De Bernardis, M De Petris, S Masi, F Melchiorri, E Aquilini, L Martinis, F Scaramuzzi, B Melchiorri, A Boscaleri, et al. The boomerang experiment. *Space Science Reviews*, 74(1-2):145–150, 1995.

[65] AT Lee, P Ade, A Balbi, J Bock, J Borrill, A Boscaleri, BP Crill, P De Bernardis, H Del Castillo, P Ferreira, et al. Maxima: an experiment to measure temperature anisotropy in the cosmic microwave background. In *AIP Conference Proceedings*, volume 476, pages 224–236. AIP, 1999.

[66] EM Leitch, C Pryke, NW Halverson, J Kovac, G Davidson, S LaRoque, E Schartman, J Yamasaki, JE Carlstrom, WL Holzapfel, et al. Experiment design and first season observations with the degree angular scale interferometer. *The Astrophysical Journal*, 568(1):28, 2002.

[67] Andrew R Liddle, Paul Parsons, and John D Barrow. Formalizing the slow-roll approximation in inflation. *Physical Review D*, 50(12):7222, 1994.

[68] Andrei D Linde. A new inflationary universe scenario: a possible solution of the horizon, flatness, homogeneity, isotropy and primordial monopole problems. *Physics Letters B*, 108(6):389–393, 1982.

[69] Charles H Lineweaver, George F Smoot, Charles L Bennett, Edward L Wright, Luis Tenorio, A Kogut, Phil B Keegstra, G Hinshaw, and Anthony J Banday. Correlated errors in the cobe dmr sky maps. *arXiv preprint astro-ph/9403021*, 1994.

[70] J. B. Melin et al. Exploring Cosmic Origins with CORE: Cluster Science. *JCAP*, 1804(04):019, 2018.

[71] NJ Miller, M Shimon, and BG Keating. Cmb polarization systematics due to beam asymmetry: Impact on cosmological birefringence. *Physical Review D*, 79(10):103002, 2009.

[72] Charles W. Misner, K. S. Thorne, and J. A. Wheeler. *Gravitation*. W. H. Freeman, San Francisco, 1973.

[73] Diego Molinari. Phd thesis: Development of new tools and devices for cmb and foreground data analysis and future experiments.

[74] P Natoli, G De Gasperis, C Gheller, and N Vittorio. A map-making algorithm for the planck surveyor. *Astronomy & Astrophysics*, 372(1):346–356, 2001.

[75] P. Natoli et al. Exploring cosmic origins with core: mitigation of systematic effects. *JCAP*, 1804(04):022, 2018.

[76] CB Netterfield, PAR Ade, JJ Bock, JR Bond, J Borrill, A Boscaleri, K Coble, CR Contaldi, BP Crill, P De Bernardis, et al. A measurement by boomerang of multiple peaks in the angular power spectrum of the cosmic microwave background. *The Astrophysical Journal*, 571(2):604, 2002.

[77] Keith A Olive, Particle Data Group, et al. Review of particle physics. *Chinese physics C*, 38(9):090001, 2014.

[78] S Padin, MC Shepherd, JK Cartwright, RG Keeney, BS Mason, TJ Pearson, ACS Readhead, WA Schaal, J Sievers, PS Udomprasert, et al. The cosmic background imager. *Publications of the Astronomical Society of the Pacific*, 114(791):83–97, 2002.

[79] Luca Pagano, Paolo de Bernardis, Grazia De Troia, Giulia Gubitosi, Silvia Masi, Alessandro Melchiorri, Paolo Natoli, Francesco Piacentini, and Gianluca Polenta. Cmb polarization systematics, cosmological birefringence, and the gravitational waves background. *Physical Review D*, 80(4):043522, 2009.

[80] Arno A. Penzias and Robert Woodrow Wilson. A measurement of excess antenna temperature at 4080-mc/s. *Astrophys. J.*, 142:419–421, 1965.

[81] Gianluca Polenta, D Marinucci, A Balbi, P De Bernardis, E Hivon, S Masi, P Natoli, and N Vittorio. Unbiased estimation of an angular power spectrum. *Journal of Cosmology and Astroparticle Physics*, 2005(11):001, 2005.

[82] Gary Prezeau and Martin Reinecke. Algorithm for the evaluation of reduced wigner matrices. *The Astrophysical Journal Supplement Series*, 190(2):267, 2010.

[83] Bahman Rabii, Celeste D Winant, JS Collins, AT Lee, PL Richards, ME Abroe, S Hanany, BR Johnson, P Ade, A Balbi, et al. Maxima: A balloon-borne cosmic microwave background anisotropy experiment. *Review of Scientific Instruments*, 77(7):071101, 2006.

[84] Britt Reichborn-Kjennerud, Asad M Aboobaker, Peter Ade, François Aubin, Carlo Baccigalupi, Chaoyun Bao, Julian Borrill, Christopher Cantalupo, Daniel Chapman, Joy Didier, et al. Ebex: a balloon-borne cmb polarization experiment. In *Millimeter, Submillimeter, and Far-Infrared Detectors and Instrumentation for Astronomy V*, volume 7741, page 77411C. International Society for Optics and Photonics, 2010.

[85] M. Remazeilles et al. Exploring cosmic origins with CORE: B-mode component separation. *JCAP*, 1804(04):023, 2018.

[86] Jose Alberto Rubino-Martin, Rafael Rebolo, Pedro Carreira, Kieran Cleary, Rod D Davies, Richard J Davis, Clive Dickinson, Keith Grainge, Carlos M Gutierrez, Michael P Hobson, et al. First results from the very small array—iv. cosmological parameter estimation. *Monthly Notices of the Royal Astronomical Society*, 341(4):1084–1092, 2003.

[87] George B Rybicki and Alan P Lightman. *Radiative processes in astrophysics*. John Wiley & Sons, 2008.

[88] Barbara Ryden. *Introduction to cosmology*. Cambridge University Press, 2016.

[89] Paul F Scott, Pedro Carreira, Kieran Cleary, Rod D Davies, Richard J Davis, Clive Dickinson, Keith Grainge, Carlos M Gutierrez, Michael P Hobson, Michael E Jones, et al. First results from the very small array—iii. the cosmic microwave background power spectrum. *Monthly Notices of the Royal Astronomical Society*, 341(4):1076–1083, 2003.

[90] Leonardo Senatore. Lectures on Inflation. In *Proceedings, Theoretical Advanced Study Institute in Elementary Particle Physics: New Frontiers in Fields and Strings (TASI 2015): Boulder, CO, USA, June 1-26, 2015*, pages 447–543, 2017.

[91] Meir Shimon, Brian Keating, Nicolas Ponthieu, and Eric Hivon. Cmb polarization systematics due to beam asymmetry: Impact on inflationary science. *Physical Review D*, 77(8):083003, 2008.

[92] G. F. Smoot, C. L. Bennett, A. Kogut, J. Aymon, C. Backus, G. de Amici, K. Galuk, P. D. Jackson, P. Keegstra, L. Rokke, L. Tenorio, S. Torres, S. Gulkis, M. G. Hauser, M. Janssen, J. C. Mather, R. Weiss, D. T. Wilkinson, E. L. Wright, N. W. Boggess, E. S. Cheng, T. Kelsall, P. Lubin, S. Meyer, S. H. Moseley, T. L. Murdock, R. A. Shafer, and R. F. Silverberg. First results of the cobe satellite measurement of the anisotropy of the cosmic microwave background radiation. *Advances in Space Research*, 11:193–205, 1991.

[93] George Fitzerald Smoot, Charles L Bennett, A Kogut, J Aymon, C Backus, G De Amici, K Galuk, Peter D Jackson, P Keegstra, L Rokke, et al. Preliminary results from the cobe differential microwave radiometers-large angular scale isotropy of the cosmic microwave background. *The Astrophysical Journal*, 371:L1–L5, 1991.

[94] Paul M Sutter, Benjamin D Wandelt, Jason D McEwen, Emory F Bunn, Ata Karakci, Andrei Korotkov, Peter Timbie, Gregory S Tucker, and Le Zhang. Probabilistic image reconstruction for radio interferometers. *Monthly Notices of the Royal Astronomical Society*, 438(1):768–778, 2013.

[95] Jan Tauber, Peter AR Ade, N Aghanim, MIR Alves, C Armitage-Caplan, M Arnaud, M Ashdown, F Atrio-Barandela, J Aumont, H Aussel, et al. Planck 2013 results. i. overview of products and scientific results. *Astronomy and Astrophysics*, 571, 2014.

[96] Angela C Taylor, Pedro Carreira, Kieran Cleary, Rod D Davies, Richard J Davis, Clive Dickinson, Keith Grainge, Carlos M Gutiérrez, Michael P Hobson, Michael E Jones, et al. First results from the very small array—ii. observations of the cosmic microwave background. *Monthly Notices of the Royal Astronomical Society*, 341(4):1066–1075, 2003.

[97] Max Tegmark and George Efstathiou. A method for subtracting foregrounds from multifrequency cmb sky maps. *Monthly Notices of the Royal Astronomical Society*, 281(4):1297–1314, 1996.

[98] Shinji Tsujikawa. Introductory review of cosmic inflation. In *2nd Tah Poe School on Cosmology: Modern Cosmology Phitsanulok, Thailand, April 17-25, 2003*, 2003.

[99] Robert A Watson, Pedro Carreira, Kieran Cleary, Rod D Davies, Richard J Davis, Clive Dickinson, Keith Grainge, Carlos M Gutierrez, Michael P

Hobson, Michael E Jones, et al. First results from the very small array—i. observational methods. *Monthly notices of the royal astronomical society*, 341(4):1057–1165, 2003.

[100] Steven Weinberg. *Gravitation and cosmology: principles and applications of the general theory of relativity.* Wiley New York, 1972.

[101] M. White, editor. *Anisotropies in the CMB*, 1999.

[102] Edward L Wright, Gary Hinshaw, and Charles L Bennett. Producing megapixel cosmic microwave background maps from differential radiometer data. *The Astrophysical Journal Letters*, 458(2):L53, 1996.

[103] D Yvon and F Mayet. Mirage: A new iterative map-making code for cmb experiments. *Astronomy & Astrophysics*, 436(2):729–739, 2005.

Thanks

I would like to thank my advisor Paolo Natoli for guiding and supporting me over this three beautiful years.
I would like to thank my co-advisor Diego Molinari that has always been available for help me during this years with helpful suggestion.
I would like to thank my family for the support and constant encouragement.
A very special thank goes to Francesco that believe in me and encourage me every single day.
I want to thank all the people who shared with me beautiful and less beautiful moments during these years, especially the last very stressful months: Ugo, Umbe, Cate, Dani, Benry, Vale, Ale, Bea, Carda, Eri, Max and Luca.